



PhD THESIS from UNIVERSITÉ DE LYON

in cotutelle with

Technische Universität München

---

**SPH simulation of free surface flows**  
**Application to centrifugal atomization process for UMo powder synthesis**

**Sandra GEARA**

---

COMMITTEE:

|                   |      |  |                       |
|-------------------|------|--|-----------------------|
| ADAMS, Nikolaus   | Prof | Technische Universität München, Germany  | Chairman              |
| VIDAL, David      | Prof | Polytechnique Montréal, Canada           | Referee               |
| SIBILLA, Stefano  | Prof | Università di Pavia, Italy               | Referee               |
| CAMEIRAO, Ana     | Prof | École des Mines de Saint-Étienne, France | Examiner              |
| PETRY, Winfried   | Prof | Technische Universität München, Germany  | PhD director          |
| BONNEFOY, Olivier | Prof | École des Mines de Saint-Étienne, France | PhD director          |
| ADAMI, Stefan     | Dr   | Technische Universität München, Germany  | PhD co-supervisor     |
| MARTIN, Sylvain   | Dr   | École des Mines de Saint-Étienne, France | PhD co-supervisor     |
| STEPNIK, Bertrand | Dr   | Framatome-CERCA, France                  | Industrial supervisor |
| ALLENOU, Jérôme   | Dr   | Framatome-CERCA, France                  | Industrial supervisor |

Die Dissertation wurde am 24.01.2022 bei der Technischen Universität München eingereicht und durch die TUM School of Natural Sciences am 27.10.2022 angenommen.

**Spécialités doctorales**  
 SCIENCES ET GENIE DES MATERIAUX  
 MECANIQUE ET INGENIERIE  
 GENIE DES PROCEDES  
 SCIENCES DE LA TERRE  
 SCIENCES ET GENIE DE L'ENVIRONNEMENT

**Responsables :**  
 K. Wolski Directeur de recherche  
 S. Drapier, professeur  
 F. Gruy, Maître de recherche  
 B. Guy, Directeur de recherche  
 V.Laforest, Directeur de recherche

**Spécialités doctorales**  
 MATHEMATIQUES APPLIQUEES  
 INFORMATIQUE  
 SCIENCES DES IMAGES ET DES FORMES  
 GENIE INDUSTRIEL  
 MICROELECTRONIQUE

**Responsables**  
 M. Batton-Hubert  
 O. Boissier, Professeur  
 JC. Pinoli, Professeur  
 N. Absi, Maître de recherche  
 Ph. Lalevée, Professeur

**EMSE : Enseignants-chercheurs et chercheurs autorisés à diriger des thèses de doctorat (titulaires d'un doctorat d'État ou d'une HDR)**

|                |                |                        |                                      |       |
|----------------|----------------|------------------------|--------------------------------------|-------|
| ABSI           | Nabil          | MR                     | Génie industriel                     | CMP   |
| AUGUSTO        | Vincent        | MR                     | Génie industriel                     | CIS   |
| AVRIL          | Stéphane       | PR                     | Mécanique et ingénierie              | CIS   |
| BADEL          | Pierre         | PR                     | Mécanique et ingénierie              | CIS   |
| BALBO          | Flavien        | PR                     | Informatique                         | FAYOL |
| BASSEREAU      | Jean-François  | PR                     | Sciences et génie des matériaux      | SMS   |
| BATTON-HUBERT  | Mireille       | PR                     | Mathématiques appliquées             | FAYOL |
| BEIGBEDER      | Michel         | MA                     | Informatique                         | FAYOL |
| BILAL          | Blayac         | DR                     | Sciences et génie de l'environnement | SPIN  |
| BLAYAC         | Sylvain        | PR                     | Microélectronique                    | CMP   |
| BOISSIER       | Olivier        | PR                     | Informatique                         | FAYOL |
| BONNEFOY       | Olivier        | PR                     | Génie des Procédés                   | SPIN  |
| BORBELY        | Andras         | DR                     | Sciences et génie des matériaux      | SMS   |
| BOUCHER        | Xavier         | PR                     | Génie Industriel                     | FAYOL |
| BRUCHON        | Julien         | PR                     | Mécanique et ingénierie              | SMS   |
| CAMEIRAO       | Ana            | PR                     | Génie des Procédés                   | SPIN  |
| CHRISTIEN      | Frédéric       | PR                     | Science et génie des matériaux       | SMS   |
| DAUZERE-PERES  | Stéphane       | PR                     | Génie Industriel                     | CMP   |
| DEBAYLE        | Johan          | MR                     | Sciences des Images et des Formes    | SPIN  |
| DEGEORGE       | Jean-Michel    | MA                     | Génie industriel                     | Fayol |
| DELAFOSSÉ      | David          | PR                     | Sciences et génie des matériaux      | SMS   |
| DELORME        | Xavier         | PR                     | Génie industriel                     | FAYOL |
| DESRAYAUD      | Christophe     | PR                     | Mécanique et ingénierie              | SMS   |
| DJENIZIAN      | Thierry        | PR                     | Science et génie des matériaux       | CMP   |
| BERGER-DOUCE   | Sandrine       | PR                     | Sciences de gestion                  | FAYOL |
| DRAPIER        | Sylvain        | PR                     | Mécanique et ingénierie              | SMS   |
| DUTERTRE       | Jean-Max       | PR                     | Microélectronique                    | CMP   |
| EL MRABET      | Nadia          | MA                     | Microélectronique                    | CMP   |
| FAUCHEU        | Jenny          | MA                     | Sciences et génie des matériaux      | SMS   |
| FAVERGEON      | Loïc           | MR                     | Génie des Procédés                   | SPIN  |
| FEILLET        | Dominique      | PR                     | Génie Industriel                     | CMP   |
| FOREST         | Valérie        | PR                     | Génie des Procédés                   | CIS   |
| FRACZKIEWICZ   | Anna           | DR                     | Sciences et génie des matériaux      | SMS   |
| GAVET          | Yann           | MA                     | Sciences des Images et des Formes    | SPIN  |
| GERINGER       | Jean           | MA                     | Sciences et génie des matériaux      | CIS   |
| GONDRAN        | Natacha        | MA                     | Sciences et génie de l'environnement | FAYOL |
| GONZALEZ FELIU | Jesus          | MA                     | Sciences économiques                 | FAYOL |
| GRAILLOT       | Didier         | DR                     | Sciences et génie de l'environnement | SPIN  |
| GRIMAUD        | Frederic       | EC                     | Génie mathématiques et industriel    | FAYOL |
| GROSSEAU       | Philippe       | DR                     | Génie des Procédés                   | SPIN  |
| GRUY           | Frédéric       | PR                     | Génie des Procédés                   | SPIN  |
| HAN            | Woo-Suck       | MR                     | Mécanique et ingénierie              | SMS   |
| HERRI          | Jean Michel    | PR                     | Génie des Procédés                   | SPIN  |
| ISMAILOVA      | Esma           | MC                     | Microélectronique                    | CMP   |
| KERMOUCHE      | Guillaume      | PR                     | Mécanique et Ingénierie              | SMS   |
| KLOCKER        | Helmut         | DR                     | Sciences et génie des matériaux      | SMS   |
| LAFOREST       | Valérie        | DR                     | Sciences et génie de l'environnement | FAYOL |
| LERICHE        | Rodolphe       | DR                     | Mécanique et ingénierie              | FAYOL |
| LIOTIER        | Pierre-Jacques | MA                     | Mécanique et ingénierie              | SMS   |
| MEDINI         | Khaled         | EC                     | Sciences et génie de l'environnement | FAYOL |
| MOLIMARD       | Jérôme         | PR                     | Mécanique et ingénierie              | CIS   |
| MOULIN         | Nicolas        | MA                     | Mécanique et ingénierie              | SMS   |
| MOUTTE         | Jacques        | MR                     | Génie des Procédés                   | SPIN  |
| NAVARRO        | Laurent        | MR                     | Mécanique et ingénierie              | CIS   |
| NEUBERT        | Gilles         | PR                     | Génie industriel                     | FAYOL |
| NIKOLOVSKI     | Jean-Pierre    | Ingénieur de recherche | Mécanique et ingénierie              | CMP   |
| O CONNOR       | Rodney Philip  | PR                     | Microélectronique                    | CMP   |
| PICARD         | Gauthier       | PR                     | Informatique                         | FAYOL |
| PINOLI         | Jean Charles   | PR                     | Sciences des Images et des Formes    | SPIN  |
| POURCHEZ       | Jérémy         | DR                     | Génie des Procédés                   | CIS   |
| ROUSSY         | Agnès          | MA                     | Microélectronique                    | CMP   |
| SANAUR         | Sébastien      | MA                     | Microélectronique                    | CMP   |
| SERRIS         | Eric           | IRD                    | Génie des Procédés                   | FAYOL |
| STOLARZ        | Jacques        | CR                     | Sciences et génie des matériaux      | SMS   |
| VALDIVIESO     | François       | PR                     | Sciences et génie des matériaux      | SMS   |
| VIRICELLE      | Jean Paul      | DR                     | Génie des Procédés                   | SPIN  |
| WOLSKI         | Krzystof       | DR                     | Sciences et génie des matériaux      | SMS   |
| XIE            | Xiaolan        | PR                     | Génie industriel                     | CIS   |
| YUGMA          | Gallian        | MR                     | Génie industriel                     | CMP   |

---

## Abstract

Within the framework of international nuclear non-proliferation treaties, stake-holders are invited to gradually reduce the use of highly enriched uranium. In this context, German FRM II-TUM and French fuel manufacturer CERCA-Framatome agreed to launch a common project for the design, engineering and operation of a prototype UMo (Uranium+Molybdenum) fuel-powder production facility.

The laser assisted Rotating Electrode Process (REP) is chosen for the UMo powder production. The main purpose of this work is to numerically model the atomization process of UMo powder in order to help the experimenters choosing the parameters that will give the targeted droplet size distribution. We want to simulate the fragmentation of a thin liquid film for different input parameters and then analyze the fragmentation process, the size distribution and shape of the final droplets. We have chosen the Smoothed Particle Hydrodynamics (SPH) method to model the rupture of the fluid film, as this Lagrangian method offers implicit multi-phase treatment without need for interface reconstruction.

We have extended an existing SPH code to allow for inflow boundaries for an efficient film formation. A surface tension model was implemented based on the Continuum Surface Force (CSF) approach. Furthermore, a new density model was developed to correct the density near the free surface. The SPH model was validated with the Rayleigh-Plateau instability and with the break-up of uni-directional water jet, with and without vibrations. It was then used to simulate the atomization in the REP configuration. These simulations have allowed us to better understand the fragmentation mechanisms. The results obtained were compared to semi-empirical models found in the literature and to experimental data. It was found that the droplets diameter predicted by the SPH simulations agrees with the semi-empirical model with a unique proportionality constant. Furthermore, the effect of vibrations on the droplet size has also been studied. It has been shown that, in the investigated REP configuration, vibrations do not have a significant effect on the particle size distribution.

---

## Résumé

Les accords internationaux de non-prolifération nucléaire conduisent progressivement à remplacer l'uranium hautement enrichi par de l'uranium faiblement enrichi. Dans ce contexte, FRM-II (TUM, Allemagne) et Framatome (CERCA) ont décidé de lancer un projet commun pour la conception, l'ingénierie et l'exploitation d'un prototype pour la production de poudre de combustible UMo (Uranium+ Molybdène).

Le "*laser assisted Rotating Electrode Process*" (REP) a été choisi pour la production de poudre d'UMo. L'objectif principal de ce travail est de simuler numériquement le procédé d'atomisation de poudre d'UMo afin d'aider les expérimentateurs à choisir les paramètres qui leur permettront d'obtenir la distribution en taille ciblée. L'idée principale est de simuler la fragmentation d'un film liquide mince pour différents paramètres d'entrée et ensuite analyser le processus de fragmentation et la distribution en taille des gouttes. La méthode "*Smoothed Particle Hydrodynamics*" (SPH) a été choisie pour simuler la rupture du film liquide puisque cette méthode Lagrangienne offre un traitement implicite, sans la nécessité de reconstruire l'interface.

Nous avons enrichi un code SPH existant en ajoutant une condition limite pour l'entrée des particules fluides pour permettre la formation d'un film liquide homogène. Un modèle de force de tension de surface pour les simulations en surface libre a été mis en place selon l'approche "*Continuum Surface Force*" (CSF). Par ailleurs, un nouveau modèle de densité a été développé pour corriger la densité proche de la surface. Le modèle SPH a été validé avec l'instabilité de Rayleigh-Plateau et la fragmentation d'un jet d'eau unidirectionnel, avec et sans vibrations. Le modèle a été ensuite appliqué à l'atomisation dans la configuration REP. Ces simulations nous ont permis de mieux comprendre les mécanismes de fragmentation. Les résultats obtenus ont été comparés à des modèles semi-empiriques trouvés dans la littérature et à des données expérimentales sur l'atomiseur REP. Il a été constaté que le diamètre des gouttelettes prédit par les simulations SPH correspond aux modèles semi-empiriques à une constante près. L'effet des vibrations sur la taille des gouttes a également été étudié. Il a été démontré que dans la configuration REP étudiée, les vibrations n'ont pas un effet significatif sur la distribution en taille des gouttes.

# Acknowledgments

This work is the result of a collaboration between the SPIN Center at Ecole Nationale Supérieure des Mines de Saint-Etienne (EMSE), Technische Universität München (TUM) and Framatome-CERCA.

This PhD was a rich and intense experience and it would not have been possible to accomplish without the support and guidance that I received from many people. I am sincerely and extremely grateful to my supervisors:

Prof. Olivier Bonnefoy and Dr. Sylvain Martin, for their continuous support and guidance, for their valuable scientific and personal advices, for their constant feedback and for always being available when necessary.

Dr. Stefan Adami, for his interest and involvement in this project, for his insightful comments on the SPH method and of course for sharing the SPH code and welcoming me at the AER department at TUM.

Dr. Bertrand Stepnik and Dr. Jérôme Allenou, for their encouragement, for their technical support and for the continuous monitoring of the work during these three years.

Prof. Winfried Petry, for his trust, for his interest in the project and for his help with the cotutelle.

Besides my advisors, I wish to show my appreciation to the members of the jury for their interest in this project and for devoting their valuable time to participate in the PhD committee.

I would like to thank those who have contributed to the results presented in this manuscript: Hubert and Andrea for their help with the experimental device, Jérôme for his technical help for using the cluster and Bastien for sharing with me his results on the REP atomizer.

My deep appreciation goes to all the members of the SPIN family for their warm welcome. The lively and social environment made the whole experience incredibly more gratifying. Additionally, I would also like to thank the AER team at TUM for welcoming me, they made my stays there enjoyable.

I also want to thank all my friends and colleagues for all the cherished and enjoyable moments together, especially: Tatyana, Alex, Madina, Angsar, Vinicius, Nikhil, Mohamad, Rachid, Xavier, Mathilde, Joao, Sophie, Marie, Carlos, Ayoub, Anthony, Mariam, Clara, Hanin, Quentin... A special thank you to Roland who has been by my side throughout this PhD.

A heartfelt thank you to my family, my parents and my sisters, for their constant support and love. This work is dedicated to them.

I am very fortunate to have many mentors, colleagues, friends, and family whom I can approach for advice and help. It was a pleasure to work with you all. Thank you.



# Acronyms

## Abbreviations

|        |  |
|--------|--|
| 316L   | SAE 316L grade stainless steel                                     |
| Al     | Aluminium  |
| CERCA  | Compagnie pour l'Etude et la Réalisation de Combustibles Atomiques |
| CSF    | Continuum Surface Force  |
| CSS    | Continuum Surface Stress   |
| DDF    | Direct Droplet Formation   |
| DIM    | Spatial dimension (1, 2 or 3)                                      |
| EMSE   | École des Mines de Saint-Etienne                                   |
| FD     | Film Disintegration  |
| FRM II | Forschungsreaktor München II                                       |
| INL    | Idaho National Laboratory  |
| IPF    | Inter Particle Force   |
| LD     | Ligament Disintegration  |
| Mo     | Molybdenum   |
| MRD    | Maximum Relative Deviation   |
| O      | Oxygen   |
| PDE    | Partial Differential Equation                                      |
| PSD    | Particle Size Distribution   |
| REP    | Rotating Electrode Process   |
| RMSD   | Root Mean Square Deviation   |
| SPH    | Smoothed Particle Hydrodynamics                                    |
| SPIN   | Sciences des Processus Industriels et Naturels                     |
| TUM    | Technische Universität München                                     |
| U      | Uranium  |
| UMo    | Uranium-Molybdenum alloy   |
| WCSPH  | Weakly Compressible Smoothed Particle Hydrodynamics                |

## Notations

|     |              |         |
|-----|--------------|---------|
| $a$ | Acceleration | $m/s^2$ |
|-----|--------------|---------|

---

|               |  |            |
|---------------|--|------------|
| $A_0$         | Amplitude of the vibrations                                  | $m$        |
| $\alpha$      | Coefficient for the droplet diameter in the DDF regime       | -          |
| $b$           | Cover vector   | -          |
| $Bo$          | Bond number  | -          |
| $\beta$       | Coefficient for the droplet diameter for the REP atomization | -          |
| $c$           | Color function   | -          |
| $C$           | Correction coefficient for the density                       | -          |
| $Ca$          | Capillary number   | -          |
| $Cp$          | Mass specific heat capacity                                  | $J/(kg.K)$ |
| $dt$          | Time step  | $s$        |
| $dx$          | Resolution (Initial particle spacing)                        | $m$        |
| $D$           | Diameter   | $m$        |
| $\delta$      | Dirac delta function   | -          |
| $\delta_s$    | Surface delta function                                       | -          |
| $\Delta r$    | Shift position   | $m$        |
| $\Delta u$    | Velocity variant   | $m/s$      |
| $e$           | Internal energy  | $J$        |
| $Ek$          | Ekman number   | -          |
| $\epsilon$    | Absorption coefficient                                       | -          |
| $f^{surface}$ | Surface tension force  | $N/m^3$    |
| $F$           | Frequency  | $Hz$       |
| $F^b$         | Body acceleration  | $m/s^2$    |
| $F_d$         | Driving force  | $N$        |
| $\phi$        | Laser flux density   | $W/m^2$    |
| $\varphi_m$   | Normalized mass distribution                                 | -          |
| $\varphi_N$   | Normalized number distribution                               | -          |
| $g$           | Gravitational acceleration                                   | $m/s^2$    |
| $\Gamma$      | Oscillation period   | $s$        |
| $h$           | Kernel radius support  | $m$        |
| $H$           | Film thickness   | $m$        |
| $H_{Latent}$  | Latent heat of fusion  | $J/kg$     |
| $I$           | Unit matrix  | -          |
| $k$           | Curvature  | $m^{-1}$   |
| $k'$          | Wave-number  | $m^{-1}$   |
| $K$           | Thermal conductivity   | $W/(m.K)$  |
| $kh$          | Cut-off distance   | $m$        |
| $\kappa$      | Characteristic number describing the atomization regime      | -          |
| $l$           | Characteristic length  | $m$        |
| $l_s$         | Slip length  | $m$        |

---



---

|           |  |           |
|-----------|--|-----------|
| $L_c$     | Capillary length                                 | $m$       |
| $L$       | Correction matrix for the kernel gradient        | -         |
| $\lambda$ | Wavelength                                       | $m$       |
| $\Lambda$ | Calibration parameter for surface tension force  | -         |
| $m$       | Mass   | $kg$      |
| $\mu$     | Dynamic viscosity                                | $N.s/m^2$ |
| $N$       | Number of particles                              | -         |
| $\vec{n}$ | Normal vector                                    | -         |
| $\hat{n}$ | Normalised normal vector                         | -         |
| $Oh$      | Ohnesorge number                                 | -         |
| $\theta$  | Threshold angle                                  | rad       |
| $\omega$  | Rotational speed                                 | $rad/s$   |
| $p$       | Pressure   | $Pa$      |
| $P$       | Laser power                                      | $W$       |
| $\pi$     | Surface stress tensor                            | -         |
| $q$       | Enthalpy difference                              | $J/m^3$   |
| $Q$       | Volume flow rate                                 | $m^3/s$   |
| $Q_s$     | Heat Source                                      | $W$       |
| $r$       | Position   | $m$       |
| $R$       | Radius   | $m$       |
| $R_c$     | Cut-off radius                                   | $m$       |
| $Re_E$    | Reynolds number relative to the flow rate        | -         |
| $Re_T$    | Reynolds number relative to the rotational speed | -         |
| $Ro$      | Rossby number                                    | -         |
| $\rho$    | Density  | $kg/m^3$  |
| $std$     | Standard deviation                               | -         |
| $\sigma$  | Surface tension coefficient                      | $N/m$     |
| $T$       | Temperature                                      | $K$       |
| $T_d$     | Dimensionless time                               | -         |
| $t$       | Time   | $s$       |
| $\tau$    | Viscous stress tensor                            | -         |
| $u$       | Velocity   | $m/s$     |
| $V$       | Volume   | $m^3$     |
| $w$       | Growth rate                                      | $s^{-1}$  |
| $W$       | Kernel function                                  | $m^3$     |
| $We$      | Weber number                                     | -         |
| $\xi$     | Normalizing vector                               | -         |
| $\Xi$     | Curvature tensor                                 | -         |
| $\zeta$   | Compressibility                                  | -         |

---

---

## Subscripts

|         |                                 |
|---------|---------------------------------|
| a       | Refers to the axial direction   |
| CFL     | Courant-Friedrichs-Lewy         |
| droplet | Refers to droplet properties    |
| empty   | Empty volume or area            |
| f       | Refers to fluid particles       |
| HT      | Heat transfer                   |
| i       | Refers to particle i properties |
| j       | Refers to particle j properties |
| jet     | Refers to jet properties        |
| m       | Refers to the melt properties   |
| max     | Maximum                         |
| opt     | Optimal                         |
| ref     | Refers to reference value       |
| rod     | Refers to the rod properties    |
| SD      | Support domain                  |
| ST      | Surface tension                 |
| t       | Refers to total                 |
| visc    | Viscous                         |
| w       | Refers to wall particles        |

# Contents

|   |            |
|---|------------|
| <b>Abstract</b>   | <b>iii</b> |
| <b>Résumé</b>   | <b>iv</b>  |
| <b>Acknowledgments</b>                                      | <b>v</b>   |
| <b>List of acronyms</b>                                     | <b>vii</b> |
| <b>Contents</b>   | <b>xi</b>  |
| <b>Introduction</b>   | <b>1</b>   |
| <b>I State of the art: Atomization process</b>              | <b>3</b>   |
| I.1 Production of metal powder . . . . .                    | 4          |
| I.1.1 Mechanical methods . . . . .                          | 4          |
| I.1.2 Solid-State reduction . . . . .                       | 4          |
| I.1.3 Electrolytic deposition . . . . .                     | 4          |
| I.1.4 Liquid metal atomization . . . . .                    | 5          |
| I.1.5 Rotating Electrode Process (REP) . . . . .            | 6          |
| I.1.6 Process for UMo metal powder production . . . . .     | 7          |
| I.2 The physical phenomena in the REP . . . . .             | 8          |
| I.2.1 Dimensionless numbers . . . . .                       | 8          |
| I.2.2 Droplet formation mechanism . . . . .                 | 9          |
| I.2.3 Atomization regimes . . . . .                         | 10         |
| I.2.4 Particle size . . . . .                               | 13         |
| I.2.5 Experimental parameters . . . . .                     | 13         |
| I.2.6 Vibrations . . . . .                                  | 16         |
| I.3 Experimental objectives . . . . .                       | 17         |
| <b>II State of the art: Numerical simulation</b>            | <b>19</b>  |
| II.1 Numerical simulation methods for fluid flows . . . . . | 21         |
| II.1.1 Mesh-based methods . . . . .                         | 21         |
| II.1.2 Mesh-free methods . . . . .                          | 23         |
| II.2 SPH theory . . . . .                                   | 25         |
| II.2.1 SPH method . . . . .                                 | 25         |
| II.2.2 Governing equations . . . . .                        | 28         |
| II.2.3 Implementation . . . . .                             | 32         |
| II.3 SPH and free surface flows . . . . .                   | 35         |
| II.3.1 Surface tension . . . . .                            | 35         |

|            |   |            |
|------------|---|------------|
| II.3.2     | Density calculation for free surface . . . . .  | 42         |
| II.4       | Numerical objectives . . . . .  | 44         |
| <b>III</b> | <b>Numerical developments</b>   | <b>45</b>  |
| III.1      | Program outline . . . . .   | 47         |
| III.2      | Surface tension . . . . .   | 48         |
| III.2.1    | Surface particle detection . . . . .  | 48         |
| III.2.2    | Normal vector . . . . .   | 49         |
| III.2.3    | Surface delta function . . . . .  | 50         |
| III.2.4    | Curvature . . . . .   | 51         |
| III.2.5    | Surface tension model . . . . .   | 53         |
| III.2.6    | Verification examples . . . . .   | 54         |
| III.3      | New density calculation . . . . .   | 58         |
| III.3.1    | Method description . . . . .  | 58         |
| III.3.2    | Verification examples . . . . .   | 61         |
| III.4      | Continuous inlet flow . . . . .   | 66         |
| III.4.1    | Method description . . . . .  | 66         |
| III.4.2    | Verification example . . . . .  | 67         |
| III.5      | Vibrations . . . . .  | 68         |
| III.5.1    | Method description . . . . .  | 68         |
| III.5.2    | Verification example . . . . .  | 69         |
| III.6      | Case study: Application to the break-up of unidirectional water jet . . . . .                               | 70         |
| III.6.1    | Literature review . . . . .   | 70         |
| III.6.2    | Experimental set-up . . . . .   | 70         |
| III.6.3    | SPH simulation set-up . . . . .   | 72         |
| III.6.4    | Results . . . . .   | 73         |
| III.7      | Conclusion . . . . .  | 77         |
| <b>IV</b>  | <b>Simulation of the REP atomizer</b>   | <b>79</b>  |
| IV.1       | Hypothesis . . . . .  | 80         |
| IV.1.1     | Model description . . . . .   | 81         |
| IV.1.2     | Results processing . . . . .  | 82         |
| IV.2       | Simulation parameters . . . . .   | 84         |
| IV.2.1     | Analytical calculation . . . . .  | 84         |
| IV.2.2     | Simulations parameters choice . . . . .   | 87         |
| IV.3       | REP simulation results and observations . . . . .   | 89         |
| IV.3.1     | Qualitative analysis . . . . .  | 89         |
| IV.3.2     | Particle size distribution . . . . .  | 91         |
| IV.3.3     | Effect of external vibrations . . . . .   | 102        |
| IV.4       | Conclusions . . . . .   | 104        |
|            | <b>Conclusions and perspectives</b>   | <b>107</b> |
|            | <b>Appendix A Experimental study: Influence of vibrations on the break-up of unidirectional liquid jets</b> | <b>111</b> |
|            | <b>Appendix B Convergence study</b>   | <b>115</b> |

---

|                        |            |
|------------------------|------------|
| <b>Bibliography</b>    | <b>117</b> |
| <b>List of Figures</b> | <b>131</b> |
| <b>List of Tables</b>  | <b>134</b> |



# Introduction

Nuclear reactors provide solutions to scientific, medical and engineering issues of high societal importance. In Europe, the most powerful reactors available to the scientific community are the RHF of the Laue-Langevin Institute (ILL, Grenoble, France) and the Forschungs-Neutronenquelle Heinz Maier-Leibnitz of the Technical University of Munich (TUM, Germany). These research reactors have a very high power density in the core and thus they require uranium that is highly enriched.

Within the framework of International nuclear non proliferation treaties, nuclear stakeholders are invited to gradually reduce the use of highly enriched uranium. Thus, for research reactors, new processes are being studied to replace current fuels with less enriched fuels. To maintain equivalent neutronic properties, one strategy is to replace the current relatively low density uranium (U-Si and U-Al) alloys with alloys having a higher uranium density, such as Uranium-Molybdenum alloys (UMo). In this context, German FRM II-TUM and French fuel manufacture CERICA-Framatome agreed to launch a common project for the design, engineering and operation of a UMo fuel-powder production facility in France. Each fuel plate consists of a fuel core and a frame made of Aluminium (Al). The fuel core is formed by mixing UMo powders with Al powders. The mixture is compacted by cold pressing. The core is then framed in Al clad and hot rolled (figure 1).

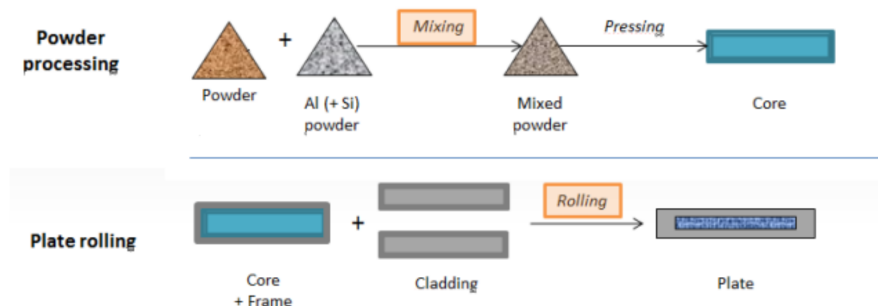


FIGURE 1: Schematic of the UMo fuel plate production (adapted from [1]).

Powder production is one crucial step in the fuel manufacturing process. In this context, it is important to control the morphology, size distribution and purity of the UMo particles to obtain the desired homogeneity of the component and therefore enhance the performance of the final product. The laser assisted Rotating Electrode Process (REP) is chosen for the UMo particles synthesis. It consists of melting the end of a metal bar (in the form of a rod) that rotates at high speed. Under the effect of the centrifugal force, the liquid metal that is formed on its top surface is radially ejected. Surface tension causes

fragmentation of the liquid metal into droplets.

In 2011, CERCA-Framatome and FRM II-TUM decided to launch a common project for the design implementation and operation of a UMo REP prototype atomizer. Based on the knowledge gathered from this project, the two parties decided to set up a REP atomizer at an industrial scale. Because the Particle Size Distribution (PSD) of the UMo powder is a key point in the quality of the final product, it is advantageous to implement an atomization process that is very well understood so that the final results can be estimated from a set of given operational parameters. For this reason, CERCA-Framatome initiated a thesis project (thèse CIFRE) with the SPIN centre of "École des Mines de Saint-Etienne" (EMSE) and in co-supervision with "Technische Universität München" (TUM). The purpose of this research project is to numerically simulate the atomization process in order to help in understanding the experimental results and scale up the atomizer. More specifically, the main objective is to help the experimenters to choose the right parameters that will allow them to obtain the targeted PSD.

The dynamics of atomization and liquid breakup are mainly dominated by surface tension forces. Because these phenomena occur on small length scales, the development of a proper surface tension model can help greatly in developing these applications. The main challenge is to be able to simulate very thin liquid metal films (few  $\mu\text{m}$  in thickness) subjected to strong topological changes. We have chosen the Smoothed Particle Hydrodynamics (SPH) method to simulate the rupture of the liquid film, as this Lagrangian method offers implicit multi-phase treatment without need for interface reconstruction. We use and enrich a generalized multi-phase SPH tool developed by Dr. Adami and his team at the Institute of Aerodynamics and Fluid Mechanics at TUM. This SPH code is based on the openFPM library, which handles parallelization and standard particle-scheme operations. We have extended this code to simulate the REP atomizer.

This manuscript is organized as follows. Firstly, we will introduce the background knowledge on liquid fragmentation process and REP atomizer. This part is followed by a description of the fundamentals and basic concepts of the weakly compressible SPH method for free surface flows. The second part describes the implementation of the SPH model. It mainly describes the surface tension model implemented and the new density correction technique near the free surface developed within the framework of this thesis. The implementation is verified with two test cases: Rayleigh-Plateau instability and unidirectional water jet break-up. The last part provides details on the numerical setup for simulating the REP atomizer and details the results on the effect of the operational parameters on the PSD. The effect of applying vibrations on the droplet size is also studied.



# Chapter I

## State of the art: Atomization process

### Contents

---

|         |   |    |
|---------|---|----|
| I.1     | Production of metal powder . . . . .                    | 4  |
| I.1.1   | Mechanical methods . . . . .                            | 4  |
| I.1.2   | Solid-State reduction . . . . .                         | 4  |
| I.1.3   | Electrolytic deposition . . . . .                       | 4  |
| I.1.4   | Liquid metal atomization . . . . .                      | 5  |
| I.1.4.1 | Gas atomization . . . . .                               | 5  |
| I.1.4.2 | Water and oil atomization . . . . .                     | 5  |
| I.1.4.3 | Plate and disk centrifugal atomization . . . . .        | 6  |
| I.1.5   | Rotating Electrode Process (REP). . . . .               | 6  |
| I.1.6   | Process for UMo metal powder production . . . . .       | 7  |
| I.2     | The physical phenomena in the REP. . . . .              | 8  |
| I.2.1   | Dimensionless numbers . . . . .                         | 8  |
| I.2.2   | Droplet formation mechanism . . . . .                   | 9  |
| I.2.3   | Atomization regimes . . . . .                           | 10 |
| I.2.3.1 | Direct droplet formation . . . . .                      | 11 |
| I.2.3.2 | Ligament disintegration . . . . .                       | 11 |
| I.2.3.3 | Film disintegration . . . . .                           | 11 |
| I.2.4   | Particle size . . . . .                                 | 13 |
| I.2.5   | Experimental parameters . . . . .                       | 13 |
| I.2.5.1 | Material properties . . . . .                           | 13 |
| I.2.5.2 | Operational parameters and atomization regime . . . . . | 14 |
| I.2.6   | Vibrations . . . . .                                    | 16 |
| I.3     | Experimental objectives. . . . .                        | 17 |

---

This chapter presents the concept of the Rotating Electrode Process (REP) and the physics driving the atomization of liquid metal films. First, a non-exhaustive list of different processes for the production of metal powder is presented. Second, the REP is described in details. Finally, the experimental studies on the atomization regimes and the particle size as a function of the operational parameters are presented.

## **I.1 Production of metal powder**

At present, several methods have been developed for industrially producing metal powders. Each production method gives different powder properties, often with different size ranges for the final powders obtained. Hence, a specific method may be selected based on the required powder properties. Some of the most common techniques are described below.

### **I.1.1 Mechanical methods**

The fabrication of metal powders by mechanical methods means to break the raw material into smaller fragments under the influence of external forces: compressive forces, shear or impact [2]. For example, the milling process relies on the combination of four basic mechanisms: impact, attrition, shear and compression. During impact, the collision of the raw material with a tough spherical impacting ball occurs. The attrition is induced by the rubbing between the raw material and the impacting ball. Finally, compression force is used to break apart these particles and form a finer powder. The main disadvantage of this method is the potential contamination of the powders from the balls and mill walls used in the process. Another main issue is the difficulty in controlling the final Particle Size Distribution (PSD). The powder formed is usually coarse and irregular in shape.

### **I.1.2 Solid-State reduction**

Solid-state reduction is a very old process frequently used in powder production. The metal ore is crushed and then mixed with another material, typically carbon [3]. The mix goes through a furnace, where a reduction reaction takes place lowering the levels of oxygen and carbon in the metal mix and leaving a sponge metal cake. The "sponge" is then crushed, separated from non-metallic material and then sieved to produce powders. The purity of the final product depends highly on that of the raw material. The resulting powder is highly irregular in shape and contains internal pores, ensuring thus a good "green strength".

### **I.1.3 Electrolytic deposition**

Using this technique, the metal that is being fragmented into powder will function as the anode and the powder will precipitate at the cathode of the electrolytic cell [2]. To be effective, this process requires specific conditions such as electrolyte composition and strength, temperature and density. This method produces high-purity and high-density powders. The main disadvantage of this method is that it is significantly more costly

---

than the other techniques, due to its high energy consumption. For this main reason, this method is generally limited to high value powders.

#### **I.1.4 Liquid metal atomization**

The atomization technique can be classified into three categories: gas, water and centrifugal atomization. The basic concept is to form powders from a molten metal. This method is widely adopted because it offers the ability to control the size of the droplets by varying the operating parameters.

##### **I.1.4.1 Gas atomization**

In gas atomization, the powder is formed by forcing the molten metal through an atomization nozzle and impinging a gas (nitrogen, argon, helium or air) [4, 5]. When the liquid metal meets the high velocity gas, it sprays in the form of jet forming tiny droplets. The size of the final powders can be controlled mainly by the nozzle shape, the melt flow rate and the gas velocity, composition and temperature. The gas atomization process can be divided into two main categories: Electrode Induction Gas Atomization (EIGA) [6] and Vacuum Induction Gas Atomization (VIGA) [7]. For the EIGA process, a rotating electrode rod is melted on one top using a conical or annular induction coil creating thus a continuous stream of molten material that will fall directly into the gas nozzle system. In the case of the VIGA process, a vacuum induction melting furnace is used to melt the alloy and is integrated with the gas atomization unit. The EIGA is mainly used for atomizing reactive metals while the VIGA process enables the atomization of non-reactive metals and their alloys.

The main objective of using this technique is to obtain spherical powders. However, due to the cooling and solidification rates, satellites might be formed because of the collisions among droplets in the spray, which make the separation of fine and coarse particles very difficult. The second major weakness is the entrapped gases during solidification that will create porosity in the powder. Furthermore, because inert gases are expensive, the production costs can be high.

##### **I.1.4.2 Water and oil atomization**

Water atomization is similar to gas atomization except that it uses an impinging jet of water rather than a gas [5]. Similar to the gas atomization technique, the size of the final droplets is mainly controlled by geometrical parameters and process parameters. The water pressure plays an important role in defining the particle size, high pressure leads to smaller powders. The microstructure of the powders obtained using this technique can be controlled by rapid quenching, but oxidation and irregular shapes often affect the quality of the product. To prevent oxidation, the water is replaced by synthetic oils. However, the oil atomization is limited to the production of low melting temperature alloys, because at high temperature pyrolysis of the oil may occur, leading to carbon pick-up. Thus, the final

powder must undergo a special treatment in order to be decarbonized.

#### **I.1.4.3 Plate and disk centrifugal atomization**

The basis of centrifugal atomization is the ejection of molten metal from a rapidly spinning container, plate or disk [2, 5]. In these cases, a cup of molten metal is rotated at high speed or the molten metal stream is impinged on a rapidly rotating disk. Under the effect of the centrifugal force and surface tension force, the liquid metal stream will spread on the surface and the resulting film will break up into a spray of droplets. These droplets will either solidify in flight to form high quality powders or deposit onto a substrate to form micro-structurally refined and chemically homogeneous preforms. The particle size depends mainly on the rotational speed, the dimensions of the system, the melt flow rate and the melt properties. The main difficulty encountered using this technique is the formation of a solid layer on the surface of the disc during atomization. To avoid this problem, it is necessary to heat the rotating disk [8]. Another problem is the limitation of the rotation speed due to mechanical restrictions, which leads to a limitation in the minimum possible particle size.

#### **I.1.5 Rotating Electrode Process (REP)**

The process was developed by the Nuclear Metals Company in 1963. This atomization technique has been widely used for the production of spherical powders of low carbon steel, cobalt-chromium and titanium alloy powders [5]. The REP has been described in details by many researchers [9, 10]. It consists of melting the end of a metal bar, in the form of a rod, that rotates at very high speed (20000-50000 rpm). Under the effect of the centrifugal force, the liquid metal film formed at the heated top surface will be ejected. Surface tension causes disintegration of the metal into droplets. These droplets will be cooled on their trajectory by a neutral gas in the chamber. The diameter of the chamber should be large enough so that the droplets will solidify before touching the chamber's walls [11]. This atomization technique can be applied to almost all metals and alloys. It allows to obtain very smooth and spherical powder of high purity. However, the main drawback is the cost because the electrode production is an expensive process. In addition, the production rate is lower compared to gas or water atomization and the PSD is not as small as with gas atomization techniques [5].

Several methods to melt the metallic rod can be used [12]:

- Creating an electric arc between a cooled tungsten electrode and the rod;
- Creating an electric arc between two rods of the same nature;
- Using a plasma torch or a laser beam.

Using the tungsten electrode may lead to a contamination of the powders due to the wear of the electrode. Moreover, the fusion system between two bars of the same nature is difficult to control. For this reason, other heat sources were considered such as plasma torches, laser beams and induction devices to enable the production of a better quality

---

powders. Nevertheless, it remains important to check the wear of the copper elements in the plasma torches that can be source of slight contamination.

### **I.1.6 Process for UMo metal powder production**

The project launched by CERCA-Framatome and FRM II-TUM consists in the design and operation of a REP atomizer for producing fuel powders at industrial scale. The REP was chosen for Uranium Molybdenum (UMo) powder production because it fulfills the requirements for metallic powder production. The use of inert atmosphere in REP atomization is very important in terms of safety. In fact, the oxygen content must be limited because of the high inflammability risk of UMo alloys. The inert atmosphere is also important for guaranteeing powder quality, since it prevents powder oxidation and thus reduces powder impurities. In addition, it promotes the formation of spherical powder because the formation of oxide layer reduces the surface tension and delays the fragmentation process [13]. Moreover, the particle size distribution is narrow and the REP ensures a high efficiency, which is essential for fuel plate fabrication.

The first REP atomizer for UMo powder fabrication was designed by the Idaho National Laboratory (INL) [14]. The atomizer uses a vertical rotational axis and the anode is fed down onto the diminishing alloy cathode unlike the commercial REP units. This arrangement allows easier operation inside the glovebox and a greater stability for the rotating UMo rod leading to a higher rotational speed and a smaller particle size. The scheme of the INL REP is presented in figure I.1. The fabricated powder is spherical with a small fraction of irregular clumps because of either an insufficient separation of molten droplets prior to solidification or a collision in flight between the droplets. Furthermore, the results show that the REP powder has a polycrystalline microstructure and no layer of columnar grain formation was observed, unlike the powder obtained using a rotating disk centrifugal atomizer that has shown an equiaxed internal microstructure surrounded by columnar grains at the edge of the particles. This difference can be explained by the rapid solidification in the REP case [14].

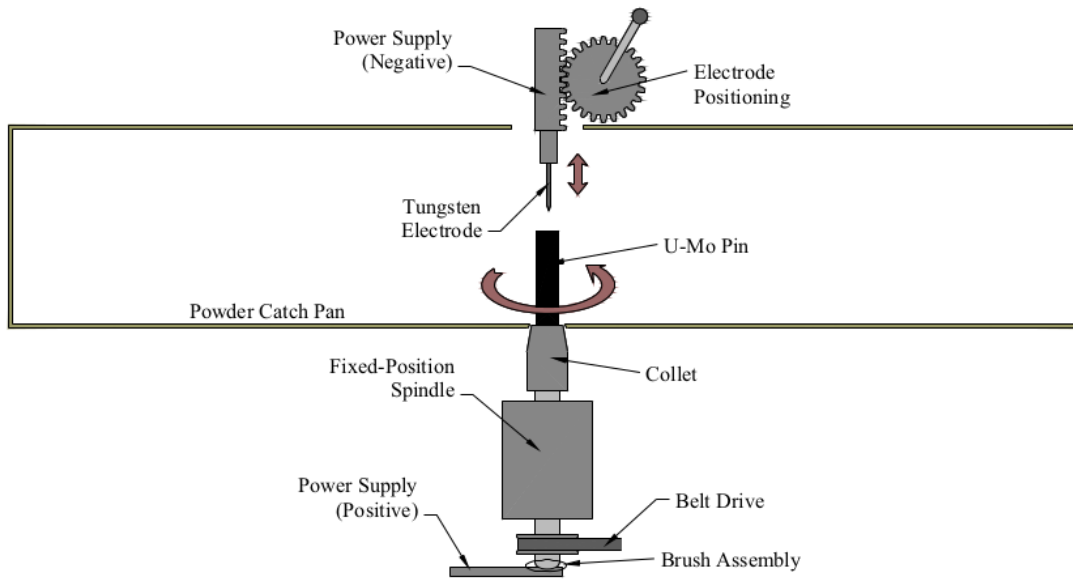


FIGURE I.1: Schematic of the INL powder atomizer [14].

CERCA-Framatome and FRM II-TUM developed from 2011 to 2015 an UMo atomizer prototype using the Electric Arc REP technology. The work was performed within the PhD thesis of R. Schenk [15] and it served as a solid foundation for the development of the new atomization pilot. The knowledge gathered from this project made it possible to propose several ideas for improving the quality of the final powders. The main improvement is the exchange of the electrode against laser heating. The new experimental atomizer device based on laser heating and rotating rod is developed in the framework of the PhD thesis of B. Ravry [16].

## I.2 The physical phenomena in the REP

### I.2.1 Dimensionless numbers

The study of the liquid behaviour and the atomization mechanism involves taking into account the magnitude of the physical forces acting upon the liquid surface. The ratio of these forces is described by the dimensionless numbers grouped in Table I.1, where  $\mu$  is the dynamic viscosity,  $\rho$  the density,  $\sigma$  the surface tension,  $l$  the characteristic length (here  $l$  is taken equal to the droplet radius  $R_{droplet}$ ),  $u$  the velocity,  $\omega$  the rotational speed and  $Q$  the volume flow rate.

---

TABLE I.1: Relevant dimensionless numbers to describe the atomization mechanisms.

| Dimensionless number | Definition  | Formula                                |
|----------------------|---|--|
| Ohnesorge number     | Viscous forces over surface tension forces                                | $Oh = \frac{\mu}{\sqrt{\rho\sigma l}}$ |
| Weber number         | Inertial forces over surface tension forces                               | $We = \frac{\rho u^2 l}{\sigma}$       |
| Reynolds number      | Inertial forces over viscous forces<br>(relative to the rotational speed) | $Re_T = \frac{\rho\omega l^2}{\mu}$    |
| Reynolds number      | Inertial forces over viscous forces<br>(relative to the flow rate)        | $Re_E = \frac{\rho Q}{l\mu}$           |
| Capillary number     | Viscous forces over surface tension forces                                | $Ca = \frac{u\mu}{\sigma}$             |
| Bond number          | Gravity force over surface tension forces                                 | $Bo = \frac{\rho g l^2}{\sigma}$       |

### I.2.2 Droplet formation mechanism

Atomization refers to the process in which a bulk liquid, for example a liquid jet or film, is fragmented into small droplets. The atomization phenomenon results from a partially random instability that grows along this liquid bulk and induces its fragmentation. The break-up occurs when the disruptive forces exceed the surface tension force. In fact, prior to fragmentation, the liquid jet will be disturbed by microscopic instabilities/waves. For some wavelengths ( $\lambda$ ), the disturbance will increase faster over time until the jet is fragmented so that the surface energy will be minimized. External forces, like centrifugal ones, may help in deforming the liquid bulk and promote the fragmentation process [5, 17].

The linear stability analysis conducted by Rayleigh [18, 19] allows to predict the size of a drop in the case of a cylindrical jet fragmentation under the effect of the surface tension force. A detailed study of this instability is presented in [17]. The dispersion relation that describes the growth rate of the disturbance as a function of the wave-number  $k' = \frac{2\pi}{\lambda}$  was proposed by Weber [20] as follows:

$$w(k') = \sqrt{\frac{\sigma}{\rho R_{jet}^3}} \left[ \sqrt{\frac{(k' R_{jet})^2 - (k' R_{jet})^4}{2} + \frac{9Oh^2(k' R_{jet})^4}{4} - \frac{3Oh(k' R_{jet})^2}{2}} \right] \quad (\text{I.1})$$

Figure I.2 presents the dispersion relation of the Rayleigh-Plateau instability for different  $Oh$  numbers. Among all the perturbations subjected to the cylindrical jet, the one having the wave-number that corresponds to the maximum growth rate will be responsible for the jet break-up. For fluids with relatively low viscosity ( $Oh \ll 1$ ), this wave-number is equal to:

$$k'_{max} R_{jet} = \frac{1}{\sqrt{2}} \left[ 1 + \frac{3Oh}{\sqrt{2}} \right]^{\frac{-1}{2}} \quad (\text{I.2})$$

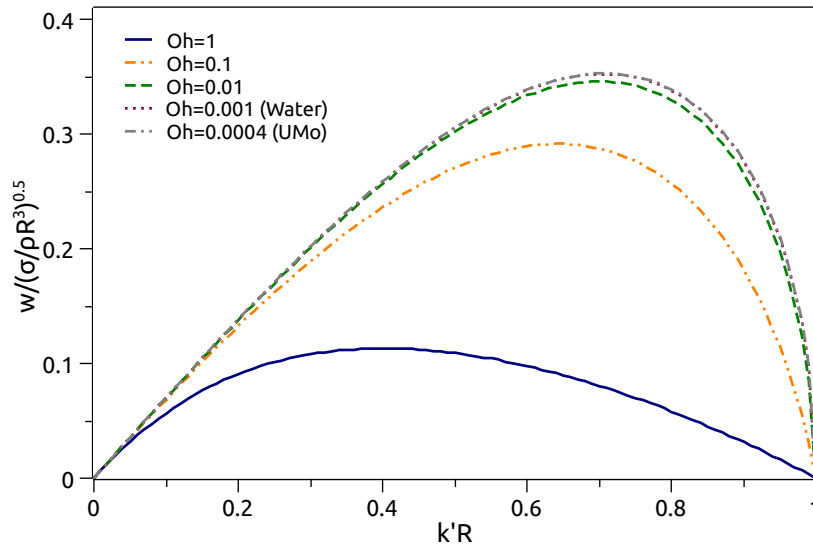


FIGURE I.2: Growth rate as a function of dimensionless wavenumber for the Rayleigh-Plateau instability.

Assuming that one droplet is produced per wavelength, the droplet size can be obtained from mass conservation as:

$$\lambda_{opt} \frac{\pi}{4} D_{jet}^2 = \frac{\pi}{6} D_{drop}^3, \quad (I.3)$$

where  $\lambda_{opt}$  denotes the wavelength experiencing the maximum growth-rate that eventually causes the break-up of the jet.

In his study, Rayleigh showed that, for low  $Oh$  number, the droplet diameter, frequency and wavelength for maximum growth are independent on the material properties. Table I.2 presents a summary of the main variables according to the Rayleigh-Plateau instability.

TABLE I.2: Rayleigh-Plateau instability.

|                 |                            |
|-----------------|----------------------------|
| $\lambda_{opt}$ | $4.5 D_{jet}$              |
| $F_{Rayleigh}$  | $0.2219 \frac{u}{D_{jet}}$ |
| $D_{drop}$      | $1.89 D_{jet}$             |

### I.2.3 Atomization regimes

The observations and studies of the centrifugal atomization have shown that there exist three basic break-up modes for the melt disintegration, see figure I.3: Direct Droplet Formation (DDF), Ligament Disintegration (LD) and film disintegration (FD) [9, 21–23].



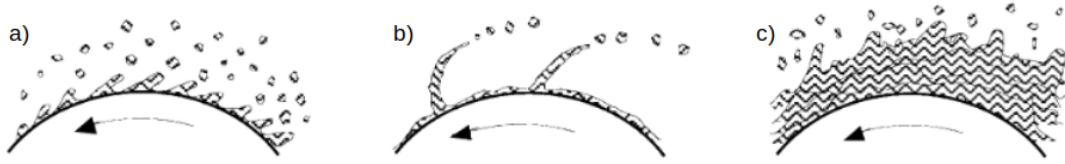


FIGURE I.3: Mechanisms of droplet formation: a) DDF, b) LD and c) FD (adapted from [24]). The liquid flow rate is increased from left to right.

### I.2.3.1 Direct droplet formation

In the DDF regime, the discrete droplets are formed as soon as the metal is detached from the disk surface. A bimodal particle size distribution was reported in this atomization regime [23, 25]. This is the result of the break-up behaviour, where one satellite drop is produced for almost every particle. Thus, the number of small particles is almost equal to that of large particles. Supposing that the operating conditions are well adjusted, namely the size of the atomization chamber and the oxygen content, the particles produced in the DDF regime are almost entirely spherical in shape.

### I.2.3.2 Ligament disintegration

The ligament disintegration regime is characterized by the formation of long unstable jets that break down into strings of droplets. As the feed rate increases, the number of ligaments increases until it reaches a certain maximum value. Any further increase in the feed rate will lead to an increase in the ligament thickness only. The number of the ligaments can also be controlled by changing the rotational speed or the electrode diameter [23]. The LD regime can produce spherical particles as well as particles of oval and elongated shapes, especially for REP because the superheat is limited and solidification may occur before ligament break-up [15, 26]. This regime is interesting from an industrial point of view because of its high productivity (production of powder mass per unit time).

### I.2.3.3 Film disintegration

This mechanism is characterized by the formation of a thin liquid sheet or film that extends around the disk prior to disintegration. The transition from the LD regime to the FD regime is reached when the ligaments can neither increase in number nor in thickness. The disintegration in the FD regime is less controlled than for the previous regimes. The particles thus obtained are less regular in shape and in size [23]. Despite its high productivity, this regime is avoided for application where a narrow size distribution is needed or desired.

An empirical relation based on experimental results has been proposed by Champagne and Angers [25] to determine the critical flow corresponding to the transition between these

three modes of atomization. This relation can be expressed as follows:

$$\kappa = \frac{Q\omega^{0.6}}{D_{rod}^{0.68}} / \frac{\sigma^{0.88}}{\rho^{0.71}\mu^{0.17}} \quad (I.4)$$

For a given liquid material, the transition from DDF to LD, and eventually to FD, can be promoted by increasing the volume flow rate and/or the rotational speed or by decreasing the rotating rode diameter. It should be noted that the transition is not sharp but rather gradual, and the coefficient of transition may vary with respect to the atomized material [15]. The constant  $\kappa$  is around 0.07 for the transition from DDF to LD, whereas it is around 1.33 for the transition from LD to FD.

According to Schenk [15], the best results for the U-8Mo atomization so far (spherical shape and size range) were observed in the LD regime in proximity of the DDF regime for  $\kappa$  approximately equal to 0.068. These operating conditions allow to benefit from the high productivity of the LD regime while guaranteeing particles of spherical or quasi-spherical shape.

The expression of  $\kappa$  is not dimensionless. Leteurtois [27] defined the three disintegration regimes as a function of the dimensionless numbers:  $Oh$ ,  $Re_T$  and  $Re_E$ . For a defined  $Oh$  number (material properties), the three atomization regimes can be represented on a  $(Re_T, Re_E)$  log-log graph by a triangle limited by three lines of equations, as in figure I.4.

$$Re_E \times Re_T \times Oh^{2.26} = 1.73 \quad (I.5)$$

$$Re_E \times Re_T^{0.596} \times Oh^{1.77} = 1.35 \quad (I.6)$$

$$Re_E \times Re_T^{-1.44} \times Oh^{-2.68} = 905 \quad (I.7)$$

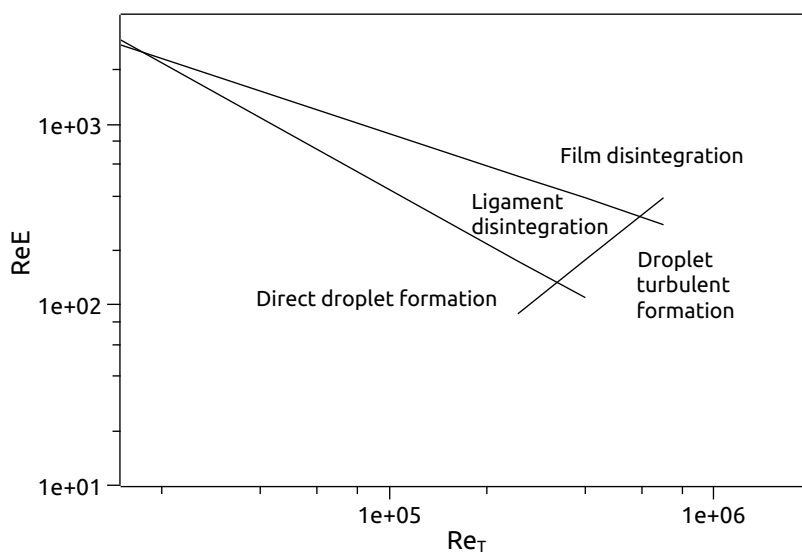


FIGURE I.4: Three regimes of droplet formation for 316L.

---

## I.2.4 Particle size

Many researchers have derived an expression for the mean droplet diameter in the DDF regime. Most of these expressions are in the form of:

$$D_{drop} = \frac{\alpha}{\omega} \sqrt{\frac{\sigma}{\rho D_{rod}}} \quad (\text{I.8})$$

This expression can be derived if we take the Rayleigh theory for instabilities and assume that the fragmentation in this regime is similar to the fragmentation of a liquid jet by replacing the gravity force  $g$  with the centrifugal force  $R\omega^2$  [28]. The list of the empirical and theoretical constants is presented in table I.3.

TABLE I.3: Empirical and theoretical values for the  $\alpha$  in equation I.8.

| Author  | $\alpha$    |
|---|-------------|
| Walton <i>et al.</i> [28]                         | 2.67-6.55   |
| Fraser <i>et al.</i> [22]                         | 3.68 - 3.86 |
| Matsumoto <i>et al.</i> [29]                      | 3.8         |
| Theory (minimum $\lambda$ for instabilities) [28] | 3.79        |
| Theory ( $\lambda$ for maximum growth rate) [28]  | 4.27        |

Champagne and Angers [9] developed a semi-empirical model to predict the powder mean diameter in the case of liquid metal with respect to the REP. Other researchers [15, 30] used this model in their experimental studies but found different constant coefficients ( $\beta$ ), reported in table I.4.

$$\frac{D_{drop}}{D_{rod}} = \beta Re_E^{0.12} Re_T^{-0.98} Oh^{-0.86} \quad (\text{I.9})$$

TABLE I.4: Values for the  $\beta$  in equation I.9.

| Author                    | $\beta$ |
|---------------------------|---------|
| Champagne and Angers [9]  | 1.42    |
| Kim <i>et al.</i> [30]    | 1.12    |
| Schenk <i>et al.</i> [15] | 1.52    |

## I.2.5 Experimental parameters

### I.2.5.1 Material properties

UMo alloys were studied by the Canadian, French, Korean and the United States for the development of their nuclear research reactors. The UMo Fuels Handbook [31] provides an overview of the available data on the UMo properties. However, in some cases, where no data are available, correlations must be used to extrapolate the properties based on the available properties of U and/or Mo. Table I.5 presents a list of the properties needed for our study.

TABLE I.5: Material properties (316L + UMo).

|                | 316L       | U          | Mo          | U-7Mo <sup>1</sup> | U-8Mo <sup>1</sup> |
|----------------|------------|------------|-------------|--------------------|--------------------|
| $\rho(kg/m^3)$ | 8000       | 19000 [31] | 10200 [31]  | 17620              | 17450              |
| $\sigma(N/m)$  | 1.6 [32]   | 1.55 [33]  | 2.8 [34]    | 1.6                | 1.77               |
| $\mu(N.s/m^2)$ | 0.005 [35] | 0.006 [36] | 0.0055 [34] | 0.006              | 0.006              |

### I.2.5.2 Operational parameters and atomization regime

CERCA-Framatome and FRM II-TUM developed an UMo atomizer prototype using the electric arc as heat source [15]. Using this prototype, UMo powders were produced and the effect of the operational parameters on the PSD were studied. The prototype was able to atomize UMo electrodes of about 40 g with an overall efficiency of only about 50% [15]. Thus, the mass of the produced UMo powders was not sufficient to prove the feasibility of the process on an industrial scale. Using the knowledge gathered from the previous study, the goal of the new project is to setup a REP atomizer able to atomize 250 g of UMo powders with an efficiency of 90%. In this context, an experimental thesis (B. Ravry [16]) was launched in 2018 for the implementation of the new atomization pilot.

In order to test and validate the general functionality of the atomizer, initially a surrogate material was used instead of UMo. For this purpose 316L stainless steel was chosen, although it was found that the steel is not a suitable replacement for the UMo regarding the atomization regime and the mass flow rate because the enthalpy of melt of 316L stainless steel is around 1200 kJ/kg compared to 250 kJ/kg for UMo [15].

Within the new experimental approach, atomization tests were carried out in a glove box under controlled atmosphere ( $[O_2] = 2-6$  ppm) with a collimated laser and a homogeneous energy distribution. The electrode has a diameter of 20 mm with a total height of 40 mm, from which only 25 mm are molten and the remaining 15 mm are used to hold the electrode in the spindle. The electrode initial mass is around 175 g and the overall atomized powder mass is around 65 g. To prevent the mechanical parts from melting, the laser beam does not illuminate the total electrode top surface. It is rather applied on a spot having a diameter between 18.05 and 18.5 mm. A reference test case was defined by choosing a rotational speed equal to 31000 rpm and a laser power of 3500 W. For this configuration, the usable powder yield efficiency is about 65 %. The effect of the operational parameters on the PSD were studied by varying these two parameters around the reference values. The experimental data gathered by B. Ravry for the reference test case are presented in table I.6 ( $t_a$  refers to the total atomization time and  $t_{sr}$  refers to the time needed for the stationary regime to start). The mass flow rate is estimated in the stationary regime. The stationary regime is defined when the melt reaches the periphery of the rod and the fragmentation process begins.

From these data, the dimensionless numbers,  $Oh$ ,  $Re_T$  and  $Re_E$  are calculated and placed on the  $(Re_T, Re_E)$  graph (hatched part from figure I.5). From the results, we

<sup>1</sup>U-xMo: x refers to the wt% of Mo in UMo alloy. Data in table I.5 are obtained by a simple interpolation considering the weight percentage of each element.

TABLE I.6: Experimental data for the reference case.

| Ref | $t_a$ (s) | $t_{sr}$ (s) | $m_{atomized}$ (g) | mass flow rate (g/s) |
|-----|-----------|--------------|--------------------|----------------------|
| 1   | 60        |              | 36                 | 1.3                  |
| 2   | 70        | after 30     | 55                 | 1.45                 |
| 3   | 70        | to 35 s      | 59                 | 1.52                 |

can deduce that the fragmentation regime for the experimental reference case should be DDF. Moreover, the coefficient  $\kappa$  from equation I.4 is found to be equal to 0.04, which also suggests a fragmentation in the DDF regime.

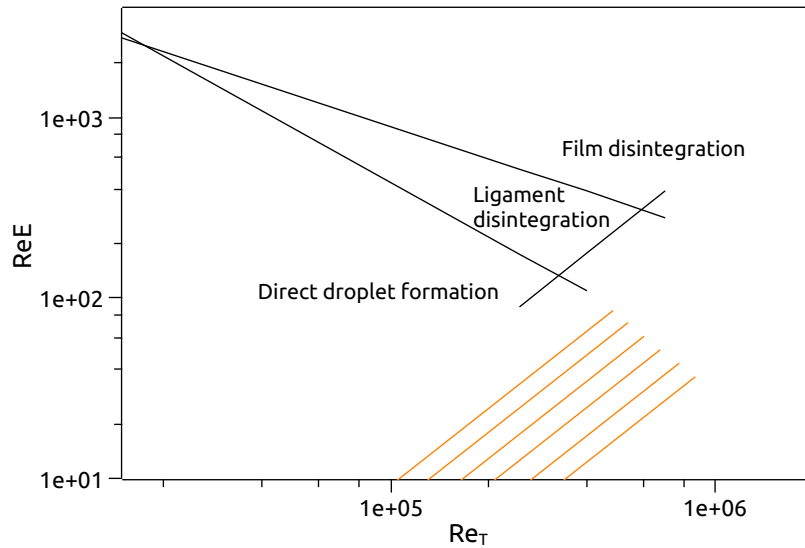


FIGURE I.5: Position of the reference case on the  $(Re_T, Re_E)$  graph for 316L.

Despite the fact that the direct laser impact is distributed over a diameter of 18.5 mm compared to the diameter of the rod of 20 mm, i.e. a rather homogenous heat distribution should be assumed, a hollow-cone shape is observed on the rod after atomization as shown in figure I.6. In addition, a small edge or rim is observed at the periphery of the atomized rod. This can be explained by the fact that the laser does not act on the entire top surface of the rod (18.5 mm for laser beam vs 20 mm for rod diameter). Moreover, due to convection and radiation, the peripheral surface of the rod cools faster than the bulk. To overcome this problem, the diameter of the rotating rod was decreased to 18 mm instead of 20 mm. For the same rotational speed and laser power, the decrease in the rod diameter significantly improved the usable powder yield efficiency which increased to 75 %. It was also observed that the proportion of non-spheric particles decreased.

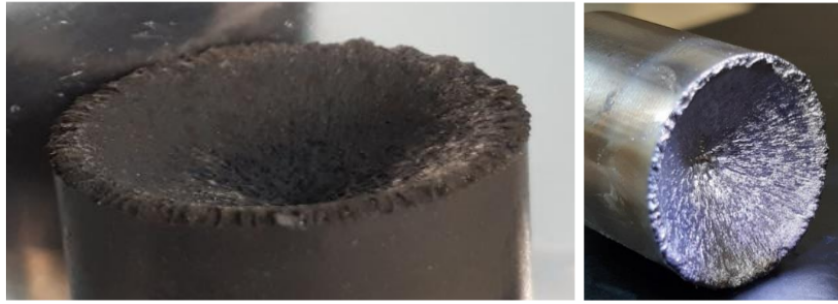


FIGURE I.6: Example of partial rod atomization.

To gain a better understanding of the atomization process at CERCA-Framatome, a high-speed camera is used [16]. Photos and recordings of the atomization process show that the melting process starts at the center of the rod (see figure I.7). In a second step, the liquid spreads in a ligament form on the surface until it reaches the edge. With time, the entire surface of the rod starts melting, leading to an increase in the production capacity and an improvement in the powder quality (more spherical powders).

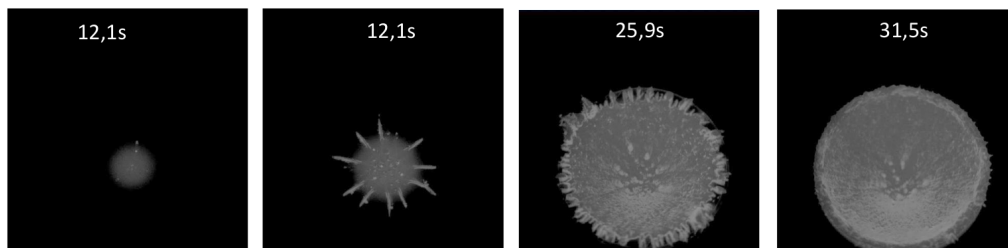


FIGURE I.7: Atomization steps for the reference test case. Top view of a laser irradiated steel rod (gray level is correlated to temperature: brighter region implies higher temperature).

## I.2.6 Vibrations

As mentioned earlier, the atomization results from instabilities that grow along the liquid surface. One possible way to control the fragmentation process is to apply defined external vibrations to the liquid jet or film. This method is effective if the vibrational frequency is properly chosen and the amplitude is large enough to trigger the natural instability.

Heinzen *et al.* [37] used external vibrations on laminar jets for producing beads and capsules. Their results showed that the main advantage of applying external vibrations is the possibility to control the droplet diameter with a very narrow size distribution. Furthermore, Zainoun *et al.* [38] used a piezoelectric cell to apply vibrations and trigger the fragmentation in the case of centrifugal atomization using a rotating disk. This technique has yielded promising results in the ligament formation zone: formation of a single droplet per wavelength and the jet is cut at a constant distance from the edge of the disk. Furthermore, the vibration of atomizing disks in the case of film disintegration was mathematically modelled by Deng and Ouyang [39]. It should be noted that it is important to consider both natural vibrations due to imbalance and imposed vibrations of the atomizing disk

---

when predicting the particle size.

### I.3 Experimental objectives

From an industrial point of view, complementary experimental and numerical studies must be performed in order to improve UMo powder production. These studies should offer a better qualitative and quantitative description of the physical phenomena taking place in the fragmentation process and the effect of the operating parameters governing the atomization.

In this objective, an experimental project was launched (PhD thesis of B. Ravry [16]) in parallel with this numerical study. The main objective of the experimental study is to design, set-up and test a REP atomizer for the production of UMo fuel powder at an industrial scale. The commissioning of the atomizer will be conducted with stainless steel as an UMo surrogate material. The idea is to carry out a parametric study to evaluate the effect of experimental conditions such as gas composition in the atomization chamber and laser intensity and operating parameters such as rotation speed, heating power and diameter of the rod on the particle size distribution and the quality of the powders. A high speed camera is also used to observe the atomization phenomenon as a function of the operating parameters.

The literature review, developed in this chapter, allowed us to understand the complexity of the fragmentation process. Thus, numerical modelling appears to be an appropriate tool to study the UMo atomization process. In this context, the specific objectives of the numerical study, stated in the next chapter, are defined in the same industrial framework.

In addition, a small experimental study will be carried out to study the effect of applying external vibrations on controlling the fragmentation process. The REP will be replaced by a simpler device: a liquid jet emerging from a small orifice. Besides, these experimental results will be used to validate the numerical model.





# Chapter II

## State of the art: Numerical simulation

### Contents

---

|          |  |    |
|----------|--|----|
| II.1     | Numerical simulation methods for fluid flows . . . . .         | 21 |
| II.1.1   | Mesh-based methods . . . . .                                   | 21 |
| II.1.1.1 | Lagrangian approach . . . . .                                  | 21 |
| II.1.1.2 | Eulerian approach . . . . .                                    | 22 |
| II.1.1.3 | Combined Lagrangian and Eulerian approaches . . . . .          | 22 |
| II.1.1.4 | Interface tracking techniques for grid-based methods . . . . . | 23 |
| II.1.2   | Mesh-free methods . . . . .                                    | 23 |
| II.1.2.1 | Smoothed Particle Hydrodynamics . . . . .                      | 24 |
| II.2     | SPH theory. . . . .  | 25 |
| II.2.1   | SPH method . . . . .   | 25 |
| II.2.1.1 | Model description . . . . .                                    | 25 |
| II.2.1.2 | Kernel function . . . . .                                      | 25 |
| II.2.1.3 | Discretization . . . . .                                       | 27 |
| II.2.1.4 | Derivatives in SPH . . . . .                                   | 27 |
| II.2.2   | Governing equations . . . . .                                  | 28 |
| II.2.2.1 | Mass conservation . . . . .                                    | 28 |
| II.2.2.2 | Momentum conservation . . . . .                                | 29 |
| II.2.2.3 | Energy conservation. . . . .                                   | 31 |
| II.2.3   | Implementation . . . . .                                       | 32 |
| II.2.3.1 | Numerical scheme and time integration . . . . .                | 32 |
| II.2.3.2 | Wall boundary conditions . . . . .                             | 33 |
| II.2.3.3 | Tensile instability . . . . .                                  | 34 |

- II.3 SPH and free surface flows . . . . . 35
  - II.3.1 Surface tension . . . . . 35
    - II.3.1.1 Main models . . . . . 35
    - II.3.1.2 Focus on the Continuum Surface Force approach with free surface simulations . . . . . 37
  - II.3.2 Density calculation for free surface . . . . . 42
- II.4 Numerical objectives . . . . . 44

---

---

This chapter presents a concise overview of the state-of-the-art for the SPH simulation method. First, the basics of this method will be detailed. Next, different models to express the surface tension force in SPH for free surface simulations will be explained in detail. Lastly, correction techniques to take into account the lack of the support domain in calculating the density for free surface flows will be presented.

## II.1 Numerical simulation methods for fluid flows

Numerical simulations translate a physical problem into a discrete form of mathematical description. The aim of the numerical simulations is to help the user understand and predict the final results of a physical system without the need to perform expensive, time consuming and sometimes not feasible experiments. Further, simulations might give access to observables, which are not directly accessible by an experiment. The main objective of our numerical work is to simulate the Rotating Electrode Process (REP) for metallic powder atomization and correlate the particle size distribution with operational parameters such as the diameter of the rod, the rotational speed, the melting strategy and others. From a practical perspective, the simulation will help in anticipating the most suitable operating conditions for the production of spherical powders of the desired size.

There are two fundamental categories for numerical simulation methods for fluid flows: mesh-based methods and mesh-free methods.

### II.1.1 Mesh-based methods

The main idea is to set up a discrete mathematical algorithm to solve a partial differential equation (PDE) on a compact domain with well-defined boundary conditions. In order to achieve this, the domain is discretized into many cells forming a grid. The PDE is solved at the nodes of the mesh and the continuous solution in the domain is obtained by interpolation. To date, numerical mesh methods have been widely used and are still the predominant methods in numerical simulations. However, these methods present some difficulties in several aspects which limit their domains of application. For instance, it is not straightforward to properly construct the mesh if the geometry of the domain is complex. In addition, these methods encounter enormous difficulties when dealing with problems involving free surfaces and large deformations. There are essentially two approaches for numerically solving problems in fluid mechanics. Namely, the Lagrangian approach and the Eulerian approach.

#### II.1.1.1 Lagrangian approach

In the Lagrangian approach, the fluid flow properties are determined by tracking the motion and properties of the meshes as they move in time. The grid is fixed or attached to the simulated object, and therefore it moves with it during the simulation. Thus, when the object deforms, the mesh deforms accordingly. Lagrangian grid-based methods are very

popular in solving computational solid mechanics problems, where the deformation is not as large as that in the fluid flows. However, it is very difficult to apply these methods for cases with extremely distorted meshes [40].

### II.1.1.2 Eulerian approach

In the Eulerian approach, the fluid properties are written as a function of space and time. The grid is fixed in space and remains unchanged during the simulation while the simulated object moves across the fixed mesh cells in the grid. This approach is used to simulate problems with large deformations because the grid remains fixed. However, there are many disadvantages associated with this method. First, it is not easy to treat irregular and complicated geometries and second, the grid should be large enough to cover the entire flow area which can cause the use of a coarse grid for computational efficiency at the dependency of the solution's accuracy. The difference between the Lagrangian and Eulerian descriptions is illustrated in figure II.1

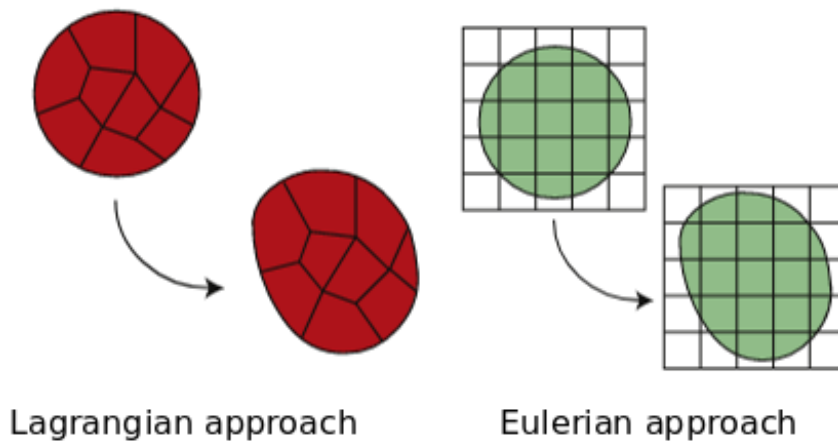


FIGURE II.1: Deformation of a continuum in a Lagrangian [left] and Eulerian [right] approach [41].

### II.1.1.3 Combined Lagrangian and Eulerian approaches

In attempt to combine the best features of both Lagrangian and Eulerian approaches, two numerical methods were developed: the Coupled Eulerian Lagrangian (CEL) [42] and the Arbitrary Lagrangian Eulerian (ALE) [43]. In general, for the CEL method, an Eulerian reference is used to discretize fluids while a Lagrangian frame is used to discretize solids. Different CEL algorithms can be characterized by the interaction between the Eulerian and Lagrangian regions. In the description of the ALE method, the nodes may be moved with the continuum like the Lagrangian approach, be held fixed in normal Eulerian fashion or be moved in some arbitrary way to suit the specific application. The ALE aims to move the mesh independently of the materials so that the mesh distortion can be

---

minimized. Thus, the main advantage of ALE method for free surface flow simulations is that it allows the free surface to be followed automatically without encountering the distortional errors of the Lagrangian approach. However, the main difficulty of the ALE method is that it does not allow new topological changes to be created and is limited to systems where the material flow is relatively predictable.

#### II.1.1.4 Interface tracking techniques for grid-based methods

Conventional grid-based numerical methods present many disadvantages related to the construction of a grid for irregular geometries and tracking the free surfaces which requires additional complex mathematical transformation that can be even more expensive than solving the problem itself. However, some mesh-based methods have been developed to simulate free surface flows, such as Volume Of Fluid method (VOF) [44, 45] and Level Set Method (LSM) [46]. The idea is to solve an additional equation to obtain the interface evolution and topology. The equation of the interface motion is expressed by:

$$\frac{\partial \Phi}{\partial t} + \vec{u} \cdot \vec{\nabla} \Phi = 0 \quad (\text{II.1})$$

where  $\Phi$  is a scalar indicator that represents the location of the interface and  $\vec{u}$  is the fluid velocity.  $\Phi$  is defined as a volume fraction for the VOF method and as a distance function for LSM. The main advantage of the VOF method over LSM is its accurate mass conservation. The normal and curvature of the interface are derived from the interface function. Both methods pose problems related to the refinement of the meshes close to the interface zones and thus re-meshing in case of large deformations. However, the implementation of a quad/core discretisation showed its efficiency in accurately representing the surface [47].

#### II.1.2 Mesh-free methods

The key idea of mesh-free methods is to provide an accurate solution for integral equations or PDEs using a set of particles instead of meshes. The simulated object is discretized into a series of particles each having a set of properties that can evolve in time. Because the computational domain is not discretized into grids, mesh-free methods can naturally handle large deformations and fluid fragmentation problems. Many mesh-free methods for fluid dynamics and for solid mechanics have been proposed so far, and since a strong interest is focused on the development of these methods, some new ones will continue to appear in the future. These methods share some common features but each one of them has its own approach for function approximation and implementation process.

One of the first mesh-less methods is the Smoothed Particle Hydrodynamics (SPH). It was first developed by Gingold and Monaghan [48] and Lucy [49] for the simulation of astrophysics problems; it was then extensively studied and extended to solve a wide range of physical problems. In the SPH method, which is a Lagrangian method, the fluid is discretized by a set of points or particles. The SPH method uses kernel interpolation to approximate the field variables at any point in a domain. Liu *et al.* [50] proposed a Reproducing Kernel Particle Method (RKPM) which improves the accuracy of the continuous

SPH approximation by introducing a correction function into this approximation.

The Diffuse Element Method (DEM) was developed by Nayroles *et al.* [51] for modelling solid mechanics problems. It uses the Moving Least Square (MLS) approximation in a Galerkin method. Later, the Element Free Galerkin (EFG) was introduced by Belytschko *et al.* [52] based on the DEM method.

Liu and his colleagues [53] developed the Point Interpolation Method (PIM). It establishes radial basis functions along with polynomials approximations by utilizing scattered nodes within the local support domain of the a point of interest. Recently, the Smoothed Point Interpolation Method (S-PIM) was introduced [54]. The formulation of S-PIM uses the weak formulation ( $W^2$ ) based on the so-called G-space, which included both continuous and discontinuous functions.

Details on these mesh-free methods and many more existing methods can be found in the book of Liu [55] .

### II.1.2.1 Smoothed Particle Hydrodynamics

#### II.1.2.1.1 General overview

The mathematical basis of the SPH method lies in the fact that the value of any function  $f$  at a point  $\vec{r}$  of a defined domain can be written using a smoothing kernel function  $W$  in the following form:

$$f(\vec{r}) = \int f(\vec{r}')W(\|\vec{r} - \vec{r}'\|)d\vec{r}' \quad (\text{II.2})$$

The kernel function  $W$  is characterized by a smoothing length  $h$  defining the influence or support area of  $W$ . The value of the kernel function tends to zero in the limit of the vanishing smoothing length. After representing the computational domain by a set of particles each having a well defined position, the continuous integral can be approximated by a discrete form as a summation of the effect of all the particles in the support domain. This method is robust for large free-surface deformation and relatively easy to code.

#### II.1.2.1.2 Advantages and disadvantages of SPH

The Lagrangian nature of SPH provides the method with some advantages when compared to usual Eulerian methods. SPH can easily deal with complex geometries with high deformations because it has an automatically adaptive resolution. Another advantage is that the computational effort is mainly concentrated in regions where the fluid is present. Moreover, SPH has excellent conservation properties for energy, linear and angular momentums.

The main drawback of this method is its high computational cost when compared to

---

other modern grid-based methods, particularly in 3D simulations. Furthermore, the implementation of proper boundary conditions to avoid particles penetration is not straightforward. Another disadvantage is the inaccuracy of the pressure prediction, especially for Weakly Compressible SPH (WCSPH).

### II.1.2.1.3 Applications of SPH

Since 1977, the SPH method has been developed and improved significantly to model a wide range of problems. By way of illustration and in a non-exhaustive manner, SPH method was used to simulate visco-elastic [56] and elasto-plastic flows [57], magneto-hydrodynamic [58, 59], multi-phase flows [60–63], turbulence [64–66], free surface flows [67–71], fusion-solidification phenomena [72], formation of spray drops [73], jet fragmentation [74–76] and many other applications.

## II.2 SPH theory

### II.2.1 SPH method

#### II.2.1.1 Model description

The mathematical basis of the SPH method lies in the fact that the value of any function  $f$  at a point  $\vec{r}$  of a defined domain  $\Omega$  can be written using a Dirac distribution  $\delta$  in the following form:

$$f(\vec{r}) = \int f(\vec{r}') \delta(\|\vec{r} - \vec{r}'\|) d\vec{r}' \quad (\text{II.3})$$

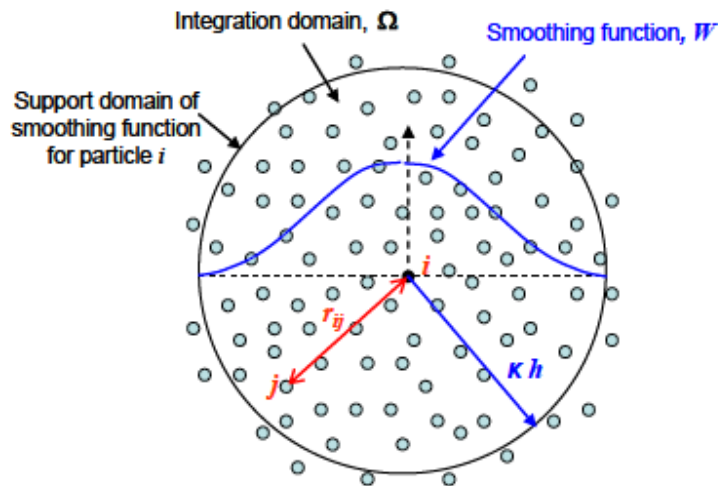
The Dirac distribution function  $\delta$  can be approximated by a smoothing kernel function  $W$  which is characterized by a smoothing length ( $h > 0$ ) defining the influence or support area of  $W$ .

#### II.2.1.2 Kernel function

The kernel function is desired to satisfy the following requirements [68, 77]:

|   |  |
|---|--|
| Parity of unity                             | $\int_{-\infty}^{+\infty} W(r - r', h) = 1$            |
| Positivity                                  | $W(r - r', h) \geq 0$                                  |
| Symmetry                                    | $W(r - r', h) = W(-(r - r'), h)$                       |
| Monotonous decrease                         | $\frac{\partial W}{\partial r} \leq 0$                 |
| Convergence towards Dirac $\delta$ function | $\lim_{h \rightarrow 0} W(r - r', h) = \delta(r - r')$ |
| Compact support                             | $ r - r'  \geq kh \implies W(r - r', h) = 0$           |

where  $kh$  is referred to as cut-off distance  $R_c$ , and the parameter  $k$  varies with the chosen kernel function. Figure II.2 gives a better understanding of how the kernel function is used to approximate a field variable of a particle  $i$  within a radius  $kh$ .

FIGURE II.2: Domain and kernel function for particle  $i$  [78].

The choice of a suitable kernel function is essential for the simulation since it has an effect on the accuracy, the time taken to perform the calculations and the numerical stability. In their original paper, Gingold and Monaghan selected a Gaussian kernel [48]. The derivatives of this function exist for all orders but it does not have a compact support and therefore it has a high computational cost (even if it is truncated the cost of the exponential remains high).

Numerous types of kernel functions are discussed in the literature [79]. The choice of the kernel function is closely related to the numerical instabilities. The most common used kernels are the B-Splines [80] having a continuous derivative up to  $(n-2)$ . Swegle *et al.* [81] showed that the stability in tension or compression depends on the sign of the second derivative  $W''$ . Furthermore, Dehnen and Aly [82] showed that the Wendland kernel helps in avoiding the pairing instability because of its non-negative Fourier transform. Moreover, Sirotkin *et al.* [75] used the Spike kernel for its stability against compression. In fact, the gradient of the kernel function is used for the calculation of the pressure force in SPH. For Spike kernel functions, this gradient does not vanish as the distance between particles is reduced. Therefore, the repulsive force between particles as they move towards each other is not neglected preventing them from overlapping. Table II.1 presents some of the most common used kernel functions.



TABLE II.1: Examples of kernel functions.

| Kernel           | Function $W$  | $\alpha_{1D}$           | $\alpha_{2D}$          | $\alpha_{3D}$            |
|------------------|---|-------------------------|------------------------|--------------------------|
| Gaussian         | $\alpha \begin{cases} \exp(-(\frac{r}{h})^2) & \text{if } (0 \leq \frac{r}{h} \leq 3) \\ 0 & \text{Otherwise} \end{cases}$  | $\frac{1}{\sqrt{\pi}h}$ | $\frac{1}{\pi h^2}$    | $\frac{1}{\pi^{3/2}h^3}$ |
| Cubic B-Spline   | $\alpha \begin{cases} (2 - \frac{r}{h})^3 - 4(1 - \frac{r}{h})^3 & \text{if } (0 \leq \frac{r}{h} \leq 1) \\ (2 - \frac{r}{h})^3 & \text{if } (1 \leq \frac{r}{h} \leq 2) \\ 0 & \text{Otherwise} \end{cases}$  | $\frac{1}{6h}$          | $\frac{5}{14\pi h^2}$  | $\frac{1}{4\pi h^3}$     |
| Quintic B-Spline | $\alpha \begin{cases} (3 - \frac{r}{h})^5 - 6(2 - \frac{r}{h})^5 + 15(1 - \frac{r}{h})^5 & \text{if } (0 \leq \frac{r}{h} \leq 1) \\ (3 - \frac{r}{h})^5 - 6(2 - \frac{r}{h})^5 & \text{if } (1 \leq \frac{r}{h} \leq 2) \\ (3 - \frac{r}{h})^5 & \text{if } (2 \leq \frac{r}{h} \leq 3) \\ 0 & \text{Otherwise} \end{cases}$ | $\frac{1}{120h}$        | $\frac{7}{478\pi h^2}$ | $\frac{3}{359\pi h^3}$   |
| Wendland C2      | $\alpha \begin{cases} (1 - \frac{r}{2h})^4 \cdot (2\frac{r}{h} + 1) & \text{if } (0 \leq \frac{r}{h} \leq 2) \\ 0 & \text{Otherwise} \end{cases}$   | $\frac{3}{4h}$          | $\frac{7}{4\pi h^2}$   | $\frac{21}{16\pi h^3}$   |
| Spike            | $\alpha \begin{cases} (1 - \frac{r}{3h})^3 & \text{if } (0 \leq \frac{r}{h} \leq 3) \\ 0 & \text{Otherwise} \end{cases}$  | $\frac{2}{3h}$          | $\frac{10}{9\pi h^2}$  | $\frac{15}{27\pi h^3}$   |

### II.2.1.3 Discretization

Equation II.3 can be approximated for small values of  $h$  by:

$$f(\vec{r}) = \int f(\vec{r}')W(\|\vec{r} - \vec{r}'\|, h)d\vec{r}' \quad (\text{II.4})$$

After representing the computational domain by a set of particles at positions  $\vec{r}_j$ , the continuous integral expressed in equation II.4 can be approximated by the following discrete form (equation II.5) as a summation of the effect of all the particles. In practice, the summation is over the particles in the support domain weighted by the smoothing function, because  $W$  falls off rapidly with distance.

$$f(\vec{r}_i) = \sum_j f(\vec{r}_j)W(\|\vec{r}_i - \vec{r}_j\|, h)V_j \quad (\text{II.5})$$

For simplicity reason,  $W(\|\vec{r}_i - \vec{r}_j\|, h)$  will be replaced by  $W_{ij}$ , where subscripts  $i$  and  $j$  denote particle  $i$  and particle  $j$ , respectively. The summation includes the particle  $i$  itself.

### II.2.1.4 Derivatives in SPH

The SPH formulation allows derivative to be estimated easily. The gradient of the function  $f$  at the position  $\vec{r}_i$  of particle  $i$  is obtained by differentiating the interpolation equation (equation II.5):

$$\nabla f_i = \sum_j V_j f_j \nabla_i W_{ij} \quad (\text{II.6})$$

However, this form of derivative does not vanish if  $f$  is constant. There are in fact, a number of ways to obtain a more accurate gradient approximation. A comprehensive study on these different ways is given in [58, 83]. One way is to write the gradient of a product of two derivable functions  $\nabla(f\phi)$  and to isolate  $\nabla f$ :

$$\nabla f_i = \frac{1}{\phi_i} \sum_j V_j \phi_j (f_j - f_i) \nabla_i W_{ij} \quad (\text{II.7})$$

We can distinguish two forms, by replacing  $\phi$  by 1 or by  $\rho$ , we obtain respectively:

$$\nabla f_i = \sum_j V_j (f_j - f_i) \nabla_i W_{ij} \quad (\text{II.8})$$

$$\nabla f_i = \frac{1}{\rho_i} \sum_j m_j (f_j - f_i) \nabla_i W_{ij} \quad (\text{II.9})$$

Another way to calculate the gradient of a function is to consider the gradient of the quotient of two differentiable functions  $\nabla(\frac{f}{\phi})$  and to isolate  $\nabla f$ :

$$\nabla f_i = \sum_j V_j \left( \frac{f_i \phi_j}{\phi_i} + \frac{f_j \phi_i}{\phi_j} \right) \nabla_i W_{ij} \quad (\text{II.10})$$

As before, we can distinguish two particular cases, by replacing  $\phi$  by 1 and  $\rho$ , we obtain, respectively:

$$\nabla f_i = \sum_j V_j (f_i + f_j) \nabla_i W_{ij} \quad (\text{II.11})$$

$$\nabla f_i = \rho_i \sum_j m_j \left( \frac{f_i}{\rho_i^2} + \frac{f_j}{\rho_j^2} \right) \nabla_i W_{ij} \quad (\text{II.12})$$

One of the good features of the above equation is that the field function  $f$  involves anti-symmetric SPH formulation that conserves linear and angular momentum when applied to the pressure force in the momentum balance equation [63].

## II.2.2 Governing equations

### II.2.2.1 Mass conservation

The Navier-Stokes equations for mass conservation and momentum conservation describe the behaviour of incompressible Newtonian viscous fluids.

If we consider that the mass  $m$  of a fluid that occupies a volume  $V(t)$  is defined by  $\int_{V(t)} \rho dV$ ; where  $\rho$  is the density, the mass variation, according to Reynolds transport theorem, can be expressed as:

$$\frac{d}{dt} \int_{V(t)} \rho dV = \int_{V(t)} \left( \frac{\partial \rho}{\partial t} + \rho \nabla \cdot \vec{u} \right) dV \quad (\text{II.13})$$

---

Mass conservation implies that:

$$\frac{d}{dt} \int_{V(t)} \rho dV = 0 \quad (\text{II.14})$$

and therefore, by combining equations II.13 and II.14 and considering that the function to be integrated is continuous, we obtain the mass conservation equation as follows:

$$\frac{\partial \rho}{\partial t} = -\rho \nabla \cdot \vec{u} \quad (\text{II.15})$$

In standard SPH, a constant mass is assigned to each particle and does not evolve with time. The density can be evaluated directly from the kernel interpolation, this method is known as the density summation. By considering the field function  $f$  as the density  $\rho$  in equation II.5, we obtain:

$$\rho_i = m_i \sum_j W_{ij} \quad (\text{II.16})$$

Another approach to estimate the density is to consider the continuity equation, this approach is known as the density evolution. By applying the gradient of the form of equation II.7 to the velocity field we obtain:

$$\frac{d\rho_i}{dt} = -\rho_i \sum_j V_j (\vec{u}_i - \vec{u}_j) \nabla W_{ij} \quad (\text{II.17})$$

It should be noted that by using different numerical tricks, it is possible to get other forms of SPH equations for computing the density. An overview of these different methods can be found in [83, 84].

The main disadvantage of equation II.17 is that the exact conservation of mass is not ensured and the density varies when the particles move relative to each other. Nevertheless, it has some advantages over the mass summation (equation II.16). Unlike the density summation approach, equation II.17 does not require a full support of the summation. There is also a computational advantage in using equation II.17 since the rate of change of all physical variables can be computed in one subroutine, contrary to equation II.16, where the density must be evaluated by summing over the particles before interpolating other quantities. A detailed study on computing the density for free surface flows is presented in the following section (section II.3.2).

### II.2.2.2 Momentum conservation

The conservation of the momentum is written in differential and Lagrangian form as follows:

$$\rho \frac{d\vec{u}}{dt} = -\nabla p + \text{div } \tau + \rho \vec{g} + \vec{f}^{surface} \quad (\text{II.18})$$

where  $p$  is the pressure,  $\vec{g}$  gravitational acceleration and  $\vec{f}^{surface}$  surface tension force. If we consider incompressible Newtonian fluid, the viscous stress tensor  $\tau$  is equal to  $\nu \nabla u$ ,

where  $\nu$  is the dynamic viscosity, and equation II.18 becomes:

$$\rho \frac{d\vec{u}}{dt} = -\nabla p + \nu \nabla^2 u + \rho \vec{g} + \vec{f}^{surface} \quad (\text{II.19})$$

There are multiple approaches in SPH for the approximation of the pressure gradient and the Laplacian of the viscous term in equation II.19.

### II.2.2.2.1 Pressure force

The direct form to compute the pressure force by volume unit is by replacing the field function  $f$  by the pressure  $p$  in equation II.6:

$$\nabla p_i = - \sum_j m_j \frac{p_j}{\rho_j} \nabla W_{ij} \quad (\text{II.20})$$

In spite of the simplicity of equation II.20, this equation is not symmetric and therefore, the angular and linear momentum will not be conserved. In other words, the force of particle  $j$  on particle  $i$  will not be equal and opposed to the force of  $i$  on  $j$ .

One possible solution to symmetrize the pressure gradient was proposed by Hu and Adams [60] using SPH derivatives in equation II.12:

$$\nabla p_i = - \frac{1}{m_i} \sum_j (V_i^2 + V_j^2) p_{ij} \nabla W_{ij} \quad (\text{II.21})$$

where  $p_{ij} = \frac{\rho_j p_i + \rho_i p_j}{\rho_i + \rho_j}$ . This pressure term  $p_{ij}$  ensures a continuous gradient across the interface  $\nabla p / \rho$  even for discontinuous density field [85]. Other formulations for the pressure gradient that conserve linear and angular momentum are available in the literature [83, 84].

### II.2.2.2.2 Viscous force

In SPH, the viscous force by volume unit is given by:

$$\nu \nabla^2 \vec{u} = -\nu \sum_j m_j \frac{\vec{u}_j}{\rho_j} \nabla^2 W_{ij} \quad (\text{II.22})$$

Similar to the pressure force, this equation presents the drawback of being asymmetric because the velocity term varies from one particle to another. Moreover,  $\nabla^2 W_{ij}$  is very sensitive to particle disorder. As a solution, the viscosity force can be expressed as follows [63]:

$$\nu \nabla^2 \vec{u} = - \frac{1}{m_i} \sum_j (V_i^2 + V_j^2) \nu_{ij} \frac{\vec{u}_i - \vec{u}_j}{|r_{ij}|} \frac{\partial W_{ij}}{\partial r_{ij}} \quad (\text{II.23})$$

where  $\nu_{ij} = \frac{2\nu_i \nu_j}{\nu_i + \nu_j}$ . Similarly to the pressure term, the combined viscosity form  $\nu_{ij}$  ensures a continuous shear stress and velocity profile across the interface [85]. Other forms for the viscosity force can be found in [60, 83].

---

### II.2.2.2.3 Weakly compressible SPH

Modelling incompressible flows requires to solve the Poisson equation  $p = \rho \nabla u / \nabla t$ . However, solving the Poisson equation is time consuming. Monaghan [67] introduced an alternative approach in SPH for weakly compressible flows through an equation of state, where the fluid is considered slightly compressible (WCSPH). In this case, an artificially large speed of sound has to be chosen in order to limit the density variation to within 1%. Other methods for dealing with incompressible fluids have been developed, see for example [85, 86].

For weakly compressible flows, the pressure can be calculated from the Tait equation of state which enforces low density variations and is efficient to compute:

$$p = \frac{\rho_0 c_s^2}{\gamma} \left[ \left( \frac{\rho}{\rho_0} \right)^\gamma - 1 \right] \quad (\text{II.24})$$

The exponent  $\gamma$  taken equal to 7 for water, which means that small fluctuations in the density correspond to strong pressure variations and eventually larger errors in the SPH pressure profile. Furthermore, it was found in [87] that more accurate pressure estimations are obtained if  $\gamma$  is taken equal to 1, so that errors in density and pressure remain proportional. The artificial sound of speed  $c_s$  is estimated based on a scale analysis of the Navier-Stokes equation presented by Morris *et al.* [87, 88]. It should be greater than the maximum of the following velocities:

|                       |  |
|-----------------------|--|
| Reference velocity    | $\sqrt{\frac{u_{ref}^2}{\zeta}}$           |
| Viscous term          | $\sqrt{\frac{\nu u_{ref}}{l_{ref} \zeta}}$ |
| Volume force term     | $\sqrt{\frac{F^b l_{ref}}{\zeta}}$         |
| Surface tension force | $\sqrt{\frac{(DIM-1)\sigma}{\rho h}}$      |

Here,  $F^b$  is the body acceleration in  $m/s^2$  and  $\zeta = \frac{\Delta \rho}{\rho_0}$  represents the compressibility. It is usually taken equal to 1%.

### II.2.2.3 Energy conservation

The heat conduction equation with heat sources or sinks has the following form:

$$\rho C_p \frac{dT}{dt} = \nabla \cdot (K \nabla T) + Q_s \delta(r - R) \quad (\text{II.25})$$

where  $C_p$  is the heat capacity per unit mass at constant pressure,  $T$  is the temperature,  $K$  is the thermal conductivity,  $Q_s$  denotes the source (positive) or sink (negative),  $R$  denotes the position of the source or sink and  $\delta$  is a Dirac delta function. By replacing the  $\delta$  function by a smoothing kernel function, the SPH form corresponding to equation II.25

becomes [83]:

$$C_{pi} \frac{dT_i}{dt} = \sum_j \frac{m_j}{\rho_i \rho_j} \frac{4K_i K_j}{K_i + K_j} \frac{T_i - T_j}{r_{ij}^2} \vec{r}_{ij} \cdot \nabla W_{ij} + \frac{1}{\rho_i} Q_s \xi W(r_i - R_k) \quad (\text{II.26})$$

where  $\xi$  is a normalizing factor defined by:

$$\frac{1}{\xi} = \sum_j \frac{m_j}{\rho_j} W(r_j - R) \quad (\text{II.27})$$

With phase change, the internal energy and therefore the latent heat must be considered. According to Monaghan [83], the energy equation can be written as:

$$\frac{de_i}{dt} = \frac{1}{2} \sum_j m_j \left( \frac{p_j}{\rho_j^2} + \frac{p_i}{\rho_i^2} + \pi_{ij} \right) \vec{u}_{ij} \cdot \nabla W_{ij} + C_{pi} \frac{dT_i}{dt} \quad (\text{II.28})$$

where  $\pi_{ij}$  is the artificial viscosity term, and needs only to be present during material compression. Depending on the internal energy, the phase of the SPH particle can be determined:

- if  $e_i$  is smaller than  $C_p T_{melting} \Rightarrow$  the particle is in the solid phase
- if  $e_i$  is greater than  $(C_p T_{melting} + H_{latent}) \Rightarrow$  the particle is in the liquid phase
- if  $e_i$  is in-between  $\Rightarrow$  the particle is in the melting phase.

## II.2.3 Implementation

### II.2.3.1 Numerical scheme and time integration

Because the SPH algorithm is based on regular differential equations, any stable time stepping algorithm can be used. Some of the most regularly implemented methods for numerical time integration are Euler, Leap-frog, predictor-corrector and Verlet schemes. However, in cases with no dissipation, it would be advantageous to use a symplectic integrator such as the Verlet second integrator which is reversible in time [83]. It starts with the prediction of the intermediate velocity:

$$\vec{u}^{(t+\frac{1}{2}dt)} = \vec{u}^{(t)} + \frac{1}{2} \vec{a}^{(t)} dt \quad (\text{II.29})$$

Then, the position is updated by:

$$\vec{r}^{(t+dt)} = \vec{r}^{(t)} + \vec{u}^{(t+\frac{1}{2}dt)} dt \quad (\text{II.30})$$

The new density and forces are calculated at this new position, the acceleration is deduced from Newton's second law of motion. Finally the velocity is updated by:

$$\vec{u}^{(t+dt)} = \vec{u}^{(t+\frac{1}{2}dt)} + \frac{1}{2} \vec{a}^{(t+dt)} dt \quad (\text{II.31})$$

For stability reasons the time step  $dt$  should be limited. To satisfy all the conditions, the minimum of these four time steps should be used [88]:

---

|                                 |             |   |
|---------------------------------|-------------|---|
| CFL condition                   | $dt_{CFL}$  | $0.25 \frac{h}{c_s + v_{ref}}$                          |
| Viscous diffusion condition     | $dt_{visc}$ | $0.125 \frac{\rho h^2}{\nu}$                            |
| Body force condition            | $dt_g$      | $0.25 \left[ \frac{h}{F^b} \right]^{1/2}$               |
| Surface tension force condition | $dt_{ST}$   | $0.25 \left[ \frac{\rho h^3}{2\pi\sigma} \right]^{1/2}$ |
| Heat transfer condition         | $dt_{HT}$   | $0.125 \frac{\rho C_p h^2}{K}$                          |

### II.2.3.2 Wall boundary conditions

The implementation of boundary conditions is a crucial aspect of any discretization method. However, solid boundary treatment in SPH which is a continuum scale particle method is more difficult due to the full support requirement of kernel smoothing functions. A lot of papers have been published addressing the treatments of solid wall boundary conditions, which can be globally split into two fundamental concepts. The first one is to fill the walls with virtual or ghost boundary particles [87, 89, 90]. The properties of these particles are evaluated by an extrapolation of the fluid particle properties. As for the second concept, no additional particles are required. Instead, the non-vanishing surface integral is solved or artificial repulsion forces are introduced in the momentum equation to account for the lacking support of the kernel function and to prevent penetration of the interface [91, 92].

In this work, the boundary formulation introduced by Adami *et al.* [90] is adopted. It follows the first approach and presents the advantage of handling arbitrarily complex geometries in two and three dimensions. It is applicable to both stationary and moving walls. With this formulation, the solid wall is discretized with dummy particles that contribute to the continuity and momentum evolution in the fluid phase. The properties of the dummy particles do not evolve in time. Instead, they are extrapolated from the adjacent fluid particles (figure II.3).

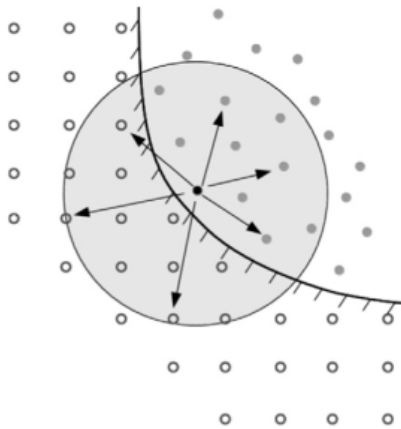


FIGURE II.3: Illustration of fluid particles (●) interacting with wall particles (○) [90].

Depending on the choice of the wall velocity, a free-slip or non-slip condition can be imposed. A free-slip condition is accomplished by omitting the viscous interaction between the fluid particles and the adjacent dummy particles. As for the non-slip condition, the

velocity of the fluid particles is extrapolated to the dummy particles. Thus, the velocity of the dummy or wall particles used in the viscous force calculation is obtained by [90]:

$$\vec{u}_w = 2\vec{u}_i - \frac{\sum_j \vec{u}_j W_{ij}}{W_{ij}} \quad (\text{II.32})$$

where the subscript  $w$  indicates wall particles.

The impermeability condition of rigid walls is respected, when moving towards a wall the density of the fluid particle increases, which in turn leads to an increase in the pressure force and prevents particles from penetrating the wall. Furthermore, the pressure and density of wall particles have to be calculated from the adjacent fluid particles via extrapolation. The pressure of these wall particles can be obtained from:

$$p_w = \frac{\sum_f p_f W_{wf} + (g - a_w) \sum_f \rho_f r_{wf} W_{wf}}{\sum_w W_{wf}} \quad (\text{II.33})$$

where the subscript  $f$  indicates fluid particles and  $a_w$  is the acceleration of wall particles.

### II.2.3.3 Tensile instability

When dealing with free surface flows in SPH, another numerical problem arises, the so-called tensile instability. In this case, attractive forces can help the formation of particle clusters. As the distance between the particles decreases, these attractive forces become even greater, causing the tensile instability. This instability can sometimes lead to divergent simulations. To avoid this problem, Xu *et al.* [93] proposed a particle displacement technique called Shift position, suitable for free surface simulations. The principle of this correction is to move the particles according to Fick's law of diffusion, i.e. from regions of high concentration to those of low concentration.

For bulk particles, the shifting vector  $\Delta\vec{r}_i$  is formulated as:

$$\Delta\vec{r}_i = -5h\vec{u}_i \nabla c_i dt \quad (\text{II.34})$$

For free surface particles,  $\Delta\vec{r}_i$  is modified as:

$$\Delta\vec{r}_i = -5h\vec{u}_i (I - \hat{n}_i \otimes \hat{n}_i) \nabla c_i dt \quad (\text{II.35})$$

where  $c_i$  is the color function (equation II.38) and  $\hat{n}_i$  is the normal vector (equation II.40).

However, it was found that the implementation of this correction may lead to an energy increase of the system and errors in the velocity profile. Moreover, because this correction is directly proportional to the velocity, the more the velocity of the system increases, the more the error will increase. Other approaches to define the intensity of this correction can be found in literature, see for example [94]. In this case, the shifting distance must be limited for stability reasons probably because the same coefficient is adopted for all fluid particles.



---

## II.3 SPH and free surface flows

### II.3.1 Surface tension

#### II.3.1.1 Main models

Surface tension force is a phenomenon of great importance in many engineering and industrial applications, such as liquid atomization. Usually, this phenomenon occurs on small space scales. Therefore, the development of a proper surface tension model can help greatly in physically developing these applications. For calculating the surface tension force with SPH, several models have been developed. These models can be divided into three major categories: Inter Particle Force (IPF), Continuum Surface Force (CSF) and Continuum Surface Stress (CSS).

##### II.3.1.1.1 Inter-particle force approach (IPF)

The IPF approach mimics microscopic inter molecular forces, where an attractive/repulsive force is applied to all SPH particles, whether they are located at the surface or not [95]. The implementation of the IPF is simple, and different formulations of the particle-particle interaction force can be found in the literature [95–97]. One example of this interaction force is given by [95]:

$$F_{ij} = \begin{cases} s_{ij} \cos\left(\frac{\pi}{2kh} r_{ij}\right) \frac{\vec{r}_{ij}}{r_{ij}} & \text{if } r_{ij} \leq kh \\ 0 & \text{if } r_{ij} > kh \end{cases} \quad (\text{II.36})$$

where  $s_{ij}$  is the strength of the force acting between particles  $i$  and  $j$  and  $kh$  is the cut-off distance. The total force acting on particle  $i$  is obtained by:

$$\vec{f}_i^{surface} = \sum_j \vec{F}_{ij} \quad (\text{II.37})$$

In general, the inter-particle force is repulsive for short distances and attractive for long distances. If the particles are regularly distributed, the force vanishes in the bulk. For boundary particles near the interface, the force is non-negligible because of the difference in the interaction coefficients  $s_{ij}$ . The force is pointing to the denser phase in the normal direction. This approach presents the advantage of being straightforward and does not require to calculate the surface curvature. Furthermore, it allows to model a variety of wetting behaviours at the fluid-solid interface, simply by assigning different interaction coefficients  $s_{ij}$ . However, the main drawback of this method is that the surface tension force needs to be calibrated with experimental results and does not converge while increasing the resolution [98, 99]. Plus, this formulation is unable to accurately represent the Marangoni effect [100].

**II.3.1.1.2 Continuum surface force approach (CSF)**

The CSF approach is based on macroscopic model that was initially proposed by Brackbill *et al.* [101] for mesh-based applications and then extended by Morris *et al.* [88] to be applied in the framework of SPH. In this model, the surface tension force is converted to a force per unit volume and is applied only on particles close to the interface. The main challenge here is to accurately calculate the normal vector and the local curvature for each particle close to the interface.

A color function  $c$  is used to define the interface and evaluate the normals and local curvatures, it is expressed as follows:

$$c_i = \begin{cases} 1 & \text{if particle } i \text{ belongs to phase } s \\ 0 & \text{otherwise} \end{cases} \quad (\text{II.38})$$

The normal vector  $\vec{n}$  can be expressed as the gradient of the color function:

$$\vec{n}_i = \vec{\nabla} c_i \quad (\text{II.39})$$

and

$$\hat{n}_i = \frac{\vec{n}_i}{|\vec{n}_i|}. \quad (\text{II.40})$$

The local curvature  $k$  for each particle is calculated as the divergence of the normalised normal vector:

$$k_i = \nabla \cdot \hat{n}_i \quad (\text{II.41})$$

The surface tension force by volume unit is expressed by:

$$\vec{f}_i^{surface} = -\Lambda \sigma_i k_i \hat{n}_i \delta_s \quad (\text{II.42})$$

where  $\Lambda$  is a numerical calibration coefficient,  $\sigma$  is the surface tension coefficient and  $\delta_s$  is called the surface delta function and is used to smooth the surface tension force over a transition band.

More work was invested in the CSF approach to provide more accurate approximation for the normal vector and the curvature at the interface. Hu and Adams [60] extended this method to simulate surface tension for two phases with high density and viscosity ratios. Adami *et al.* [102] proposed a new method for calculating the surface curvature by applying a divergence approximation. Furthermore, Qiang *et al.* [103] proposed modified equations for normal and curvature based on the Corrective Smoothing Particle Method (CSPM) derived by Chen [104].

**II.3.1.1.3 Continuum surface stress (CSS)**

The CSS approach is considered as a variant to the CSF model [60, 105]. The surface tension force is formulated as a divergence of the stress tensor, which is calculated from

---

the surface normal vectors with no need to calculate the curvature:

$$\vec{f}_i^{surface} = \nabla \cdot \pi_i \quad (\text{II.43})$$

where the surface stress  $\pi_i$  is expressed by:

$$\pi_i = \sigma(I - \hat{n}_i \hat{n}_i) |\nabla c_i| \quad (\text{II.44})$$

#### II.3.1.1.4 Summary

A detailed comparison of the IPF and CSF approaches for calculating surface tension for multiphase flow is presented in [99, 106, 107]. The comparison shows that even though the implementation of the IPF model is simple and straightforward, the CSF approach can give better results for particle distribution and pressure jump at the interface. However, a more accurate description of the curvature is still essential for the application of the CSF method, which is not trivial in SPH. Eventually, the choice of the suitable surface tension representation depends highly on the physical system being simulated.

For the simulation of atomization, a very accurate representation of surface tension is needed. For this reason, the CSF approach is chosen. More details on the application of the CSF model to free-surface flows and the correction for the lack of the full support are presented in the following section.

#### II.3.1.2 Focus on the Continuum Surface Force approach with free surface simulations

In some cases, the surrounding fluid has a small effect on the fluid being studied and thus it could be advantageous to simply neglect it in order to reduce the computational time. In this case, for free surfaces, the standard SPH approximations to calculate the normal vectors and curvatures at the interface suffer from the lack of "full support". Several review papers discussing free-surface flows in SPH have been published, see among others [108, 109].

For the specific case of surface tension force, Sirotkin *et al.* [75] proposed a corrected SPH model based on the correction matrix introduced by Bonet *et al.* [110] to adjust the kernel gradient for the calculation of the density, pressure force, normal vectors and curvatures. This kernel gradient modification increases the accuracy of the normal vectors and curvatures. However, a 1.5 times bigger smoothing length is required for more reliable results. Ordoubadi *et al.* [111] added imaginary particles near the free surface with a mirroring technique in order to take into account the missing gas particles and accurately simulate the surface tension force. Based on the examples shown in their paper, this method significantly improves the normal vectors and gives more accurate curvatures. Ehigiamusoe *et al.* [112] used a correction factor for only the curvature calculation without any additional correction for the normal vectors. This method may give stable and accurate results for simple examples, but for cases with large curvature and high surface deformation, another correction technique needs to be used for the normal vector calcu-

lation and curvature estimation. Russell *et al.* [100] applied free surface tension in order to model the selective laser melting. They proposed a correction factor for the normal vectors and curvatures. Their method gives acceptable results for their test case, but was not tested on more complex geometries, where surface tension is the dominant force. More recently, Fürstenau *et al.* [113] added a Dirichlet boundary condition on the pressure for free surface problems, thus improving the stability of the system.

Another interesting approach for calculating the surface tension force is the reconstruction of the interface with moving least squares. Subsequently, the local normal vector and curvature are calculated from the resulting smoothed interface [114]. Barecasco *et al.* [115, 116] developed a new method for detecting surface particles explicitly and used MLS for surface reconstruction in 3D. More recently, Yang *et al.* [117] presented another approach, where the surface reconstruction was done based on marching cubes method. This approach differs from the standard CSF implementation in SPH, in a sense where the surface properties are not calculated directly from the particles properties. Furthermore, it was reported to be computationally more expensive than the standard SPH calculations.

The main issue when dealing with surface tension is to maintain the stability of the system when the particle distribution is perturbed. To overcome this, a high viscosity fluid is used in many of the presented models so that the movement of the particle, specially at the free surface, is more organised.

The most common techniques for detecting free surface particles, calculating normal vectors and estimating curvatures will be presented in the following section.

### II.3.1.2.1 Surface particle detection

#### Color function

One of the most common methods to detect the interface is the color function assigned to each phase, as presented in equation II.38. For single phase simulation, the color function of all liquid particles is equal to  $c_j^0 = 1$ . The smoothing of the color function gives:

$$c_i = \sum_j \frac{m_j}{\rho_j} c_j^0 W_{ij} \quad (\text{II.45})$$

The value of the smoothed color function  $c_i$  is theoretically equal to 1 for particles in the bulk with a full kernel support. Contrary, close to the free surface the number of neighbouring particles decreases and thus the value of  $c_i$  will also decrease and be less than 1. In general, a threshold value of 0.9 is defined for detecting surface particles. Because this method is based only on the kernel summation, it is very simple to implement and does not have a large computational cost. It presents the advantage of detecting a surface band instead of only surface particles by adjusting the threshold value. However, for some special cases, low density regions may appear inside the fluid. In these regions, spurious free surface particles can be detected due to the lack of neighbouring particles, inducing

non physical surface tension forces.

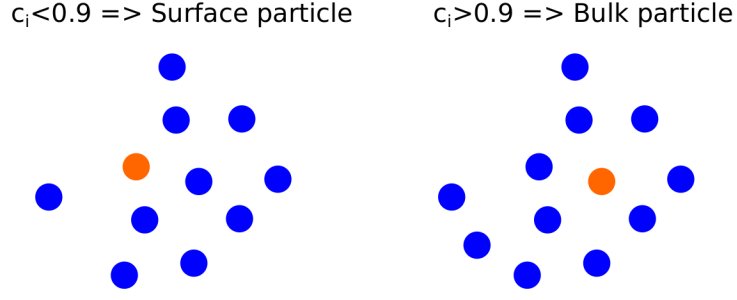


FIGURE II.4: Illustration of the color function for a surface particle [left] and a bulk particle [right].

### Disk sectors

To avoid this problem, more accurate surface tracking algorithms were developed. One method is to consider a disk around particle  $i$ , having a radius equal to the length of the supporting domain or even more for better accuracy [118]. In general, taking twice the size of the supporting domain is enough for good accuracy. This circular area is then split into sectors, and each sector is checked for neighbouring fluid particles. If at least one sector does not have any neighbouring particle, then particle  $i$  is considered as surface particle, see figure II.5 for an illustration with 8 sectors.

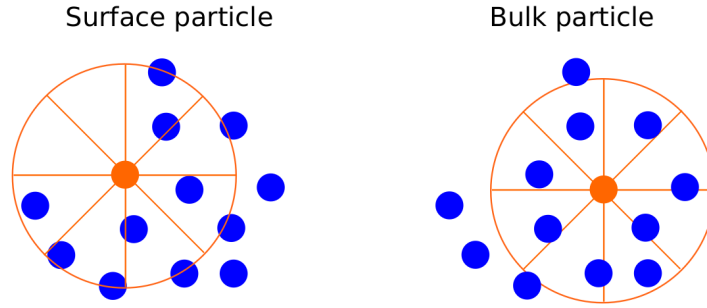


FIGURE II.5: Illustration of the sectors around a surface particle [left] and a bulk particle [right].

### Cover vector

Another accurate surface particle detection algorithm was proposed by Barescaso *et al.* [115]. This method is similar to the one presented above. Each particle  $i$  is represented by a sphere and has a cover vector defined by:

$$\vec{b}_i = \sum_j \frac{\vec{r}_{ij}}{\|\vec{r}_{ij}\|} \quad (\text{II.46})$$

For detecting surface particles, a cone of angle  $\theta_i$  (threshold angle) is considered around

each  $b_i$  (see figure II.6). If at least one of the neighbouring particles  $j$  is inside the cone, then particle  $i$  is not considered as a surface particle, otherwise particle  $i$  belongs to the free surface. The value of  $\theta_i$  plays an important role in boundary particle detection, it is usually chosen equal to  $\frac{\pi}{3}$ .

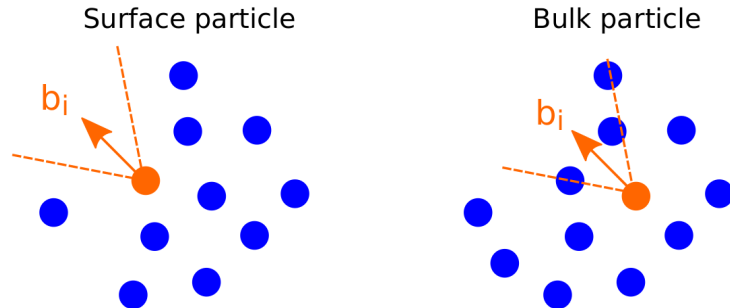


FIGURE II.6: Illustration of the cover vector for a surface particle [left] and a bulk particle [right].

### II.3.1.2.2 Normal vector

As mentioned in equation II.39, the normal vector  $\vec{n}_i$  can be expressed as the gradient of the color function:  $\vec{n}_i = \nabla c_i$ , with:

$$\nabla c_i = \sum_j V_j (c_j - c_i) \nabla W_{ij} \quad (\text{II.47})$$

To overcome the problem of lacking full support for free-surface flows, the correction matrix to adjust the kernel gradient proposed by Bonet *et al.* [110] can be used. Sirotkin *et al.* [75] used this correction technique for the normal vector and curvature calculation, while also increasing the support domain radius by a factor of 1.5.

For each particle  $i$ , the correction matrix is defined as:

$$L_i = \sum_j V_j \nabla W_{ij} \otimes \vec{r}_{ij} \quad (\text{II.48})$$

and the corrected kernel gradient is expressed as follows:

$$\nabla \tilde{W}_{ij} = L_i^{-1} \nabla W_{ij}. \quad (\text{II.49})$$

Other corrections for the normal vectors were proposed in the literature, Russell *et al.* [100] used the normalized SPH gradient of the color function for example and the corrected normal vector is expressed as follows:

$$\vec{n}_i = \sum_j V_j \left( \frac{1}{c_i} + \frac{1}{c_j} \right) \nabla W_{ij} \quad (\text{II.50})$$

Ordoubadi *et al.* [111] proposed another method that consists in adding imaginary particles by mirroring particles near the free surface. These particles have the same mass as the original particles but with a color function equal to zero. First, a transition band

---

is defined near the free surface. Then, for each particle within this transition band a special treatment is applied, whether this particle is a surface particle or not. This method presents a more complicated work for dealing with the omitted particles specially with cases with strong and abrupt deformations.

In fact, the direction and magnitude of the normal vectors are only accurate near the interface. In the bulk, the normal vectors have small magnitude with erroneous directions. This may cause a problem when calculating the curvature because in this case, the normalized normal vectors are considered. To address this issue, only well defined normal vectors are used in the surface tension force calculation by applying the following filtering as suggested in [88]:

$$R_i = \begin{cases} 1 & \text{If } \|\vec{n}_i\| > \psi \\ 0 & \text{Otherwise} \end{cases} \quad (\text{II.51})$$

where the value of  $\psi$  is typically  $0.01/dx$  and  $dx$  is the initial particle spacing.

### II.3.1.2.3 Delta function

In SPH, every field function is evaluated by a smoothing function. Thus, it seems preferable to apply the surface tension force over a few smoothing lengths or what we define as a transition band rather than on only one layer of surface particles.

First, the transition band is usually defined by taking the neighbours of the surface particles, i.e; particles in the support domain defined by the kernel function. However, a more accurate definition of this transition band could be achieved by considering the normal vectors, as in equation II.51. After defining the thickness of the transition band, it is necessary to define an appropriate surface delta function  $\delta_s$  to smooth the surface tension force. The force should be maximum at the free surface or at the tip of sharp corners and should decrease gradually while moving away from the free surface. One possible configuration is to use the norm of the normal vector. In this case, the delta function  $\delta_s$  for each particle  $i$  can be approximated as:

$$\delta_i = \Lambda \|\vec{n}_i\| \quad (\text{II.52})$$

where  $\Lambda$  is a constant calibration parameter.

### II.3.1.2.4 Curvature

In a continuum approach the curvature is a surface property. For SPH, it is defined for each particle. Thus, the local curvature for each particle is calculated as the divergence of the normalised normal vectors, as in equation II.41. Only reliable normal vectors ( $R_i = 1$ ) are considered for the curvature calculation.

Morris [88] added a normalization factor that reflects the local number density of par-

ticles with reliable normal vectors, so that the curvature is obtained by:

$$k_i = \frac{\sum_j \min(R_i, R_j) V_j (\hat{n}_j - \hat{n}_i) \cdot \nabla W_{ij}}{\sum_j \min(R_i, R_j) V_j W_{ij}} \quad (\text{II.53})$$

Sirotkin *et al.* [75] replaced the above normalization factor by the matrix correction of the kernel gradient. The curvature is then calculated as follows:

$$k_i = \sum_j \min(R_i, R_j) V_j (\hat{n}_j - \hat{n}_i) \cdot \vec{\nabla} \tilde{W}_{ij} \quad (\text{II.54})$$

Adami *et al.* [102] proposed another divergence approximation for the curvature calculation. It was originally developed for multi-phase flows but can be extended for free surface flows. The curvature is expressed as:

$$k_i = DIM \frac{\sum_j \min(R_i, R_j) V_j (\hat{n}_j - \hat{n}_i) \cdot \nabla W_{ij}}{\sum_j V_j \|\vec{r}_{ij}\| \frac{dW_{ij}}{dr}} \quad (\text{II.55})$$

where *DIM* stands for the dimension of the simulation (1, 2 or 3). Ehigiamusoe *et al.* [112] simply modified this approach by introducing a control parameter  $\epsilon$  for ignoring the gas phase.

Fürstenau *et al.* [113] found that equation II.54 overestimates the geometric curvature by almost a factor 2 in 3D simulations. To overcome this problem, they calculated the mean curvature based on a local coordinate system. First, the global curvature tensor is calculated by:

$$\Xi_{ij} = \sum_j \min(R_i, R_j) (\hat{n}_j - \hat{n}_i) \otimes \nabla \tilde{W}_{ij} \quad (\text{II.56})$$

Then, this global curvature tensor is rotated into the local coordinate system. After this transformation, the new matrix is reduced to a 2D matrix and the eigenvalues are calculated. The mean curvature is obtained as the average of the eigenvalues which are considered the principal curvatures.

Once the normal vectors, local curvatures and surface delta function are correctly obtained, the surface tension force should be applied for particles in the transition band according to equation II.42. In the next chapter III, we investigate these different correction techniques and schemes for calculating the free surface tension force.

### II.3.2 Density calculation for free surface

Another major problem for free surface flows relates to the density estimation for surface particles. As mentioned earlier, the standard SPH approximations suffer from the lack of full support. This mainly affects the density estimation and, consequently, leads to potential pressure oscillations. Many techniques have been proposed in the literature to overcome this problem.



---

The first attempt to apply SPH to free surface flow was introduced by Monaghan [67] for the simulation of wave run-up and breaking in shallow water. Monaghan used the continuity equation to calculate the change rate of the density as a function of the velocity gradient. He also introduced the XSPH velocity variant algorithm to improve the particle distribution. In XSPH, the velocity of each particle is modified to take into account the average velocity of all nearby particles. The velocity of each particle  $i$  is modified as follows:

$$\vec{u}_i^{XSPH} = \vec{u}_i - \Delta\vec{u}_i \quad (\text{II.57})$$

where  $\Delta\vec{u}_i$  is the velocity variant defined as:

$$\Delta\vec{u}_i = \varepsilon \sum_j \frac{m_j}{\bar{\rho}_{ij}} \vec{u}_{ij} W_{ij} \quad (\text{II.58})$$

where  $\varepsilon$  is a constant ( $0 \leq \varepsilon \leq 1$ ), commonly taken as 0.5 and  $\bar{\rho}_{ij} = \frac{\rho_i + \rho_j}{2}$ .

A second common approach to smooth out the pressure oscillations is to apply a density filter. Colagrossi and Landrini [89] applied a periodic re-initialization of the density field based on the Moving Least Squares Approach (MLS) proposed by Belytschko *et al.* [119] and Diltz [118]. This proposed kernel correction ensures a consistent interpolation of the density field. However, Sibilla [120] indicated that the use of integral interpolations for long simulations does not properly conserve the total volume of the particle system since the hydrostatic component of the pressure is improperly filtered.

Bonet and Lok [110] proposed a simple correction of the density field by considering a constant correction instead of a linear one or what is known as the Shepard filter. By applying this correction, equation II.16 becomes:

$$\rho_i = m_i \frac{\sum_j W_{ij}}{\sum_j V_j W_{ij}} \quad (\text{II.59})$$

These density correction methods must be applied every  $n$  time steps, where  $n$  is typically chosen between 20 and 50.

Bonet and Lok [110] also introduced another correction technique based on the modification of the kernel gradient by a correction matrix, see equation II.48. A combination of these two techniques, i.e. the constant kernel correction and the kernel gradient correction, is also possible. Various schemes for applying the kernel gradient correction can be found in the literature [121, 122].

Furthermore, Molteni and Colagrossi [123] introduced an artificial density diffusion term to smooth out the numerical noise of the pressure field. The intensity of this numerical correction is to be defined according to the problem at hand. The density evolution equation II.17 becomes:

$$\frac{d\rho_i}{dt} = -\rho_i \sum_j V_j \left[ (\vec{u}_i - \vec{u}_j) + (k_i + k_j)(\rho_i - \rho_j) \frac{\vec{r}_{ij}}{r_{ij}^2} \right] \cdot \nabla W_{ij} \quad (\text{II.60})$$

More recently, Seo *et al.* [124] proposed to correct the density of each particles based on shape functions adopted from the interpolation scheme of FEM.

All these procedures give good results, some of them are more suitable than the others depending on the application. However, these corrections can be insufficient when dealing with surface tension force. In this case, the force should be applied at each time step on surface particles. Thus, it is important to estimate the density of these particles accurately. For applications where the surface tension force is not the dominant force, Calderon *et al.* [125] developed very recently a geometrical formulation that improves the Shepard correction coefficient. In their work, the dimensionality of the problem is reduced by defining the kernel in such a way that the volume integral is cast into a surface integral. Despite the promising results, this method still contains complex and computationally expensive numerical evaluation [126].

In this present work, we propose a new density evaluation method. The idea behind this method is to calculate analytically a coefficient that represents the weight of the missing particles from the support domain and use it to correct the density summation for particles near the free surface. This new correction factor depends on the distance to the surface as well as on the curvature of the particles near the free surface. A variant of this method has originally been proposed by Herant [127] and also used by Vanhala and Cameron [128] in order to implement boundary conditions in cases where boundaries are only used for confinement. The details of this method will be presented in the next chapter (chapter III) along with verification and validation examples.

## II.4 Numerical objectives

The main objective of this work is to model the fragmentation process in the REP configuration. The previous bibliographical study highlighted the basics of the SPH method and the challenges relative to the simulations of free surface flows.

Based on the state-of-the-art, the overall main objective can be divided into the following specific objectives:

- Implementation of a proper surface tension model for simulating the beak-up of free surface flows.
- Implementation of a proper density correction technique for an accurate evaluation of the density of particles near the free surface.
- Definition of the proper boundary conditions, initial parameters and geometry of the system to be simulated.
- Verification and validation of the SPH model implemented/developed in the previous sub-objectives.
- Evaluating the effect of the operational parameters and external vibrations on the powder size distribution, using the developed SPH model.

# Chapter III

## Numerical developments

### Contents

---

|   |    |
|---|----|
| III.1 Program outline . . . . .   | 47 |
| III.2 Surface tension . . . . .   | 48 |
| III.2.1 Surface particle detection . . . . .  | 48 |
| III.2.2 Normal vector. . . . .  | 49 |
| III.2.3 Surface delta function. . . . .   | 50 |
| III.2.4 Curvature . . . . .   | 51 |
| III.2.5 Surface tension model. . . . .  | 53 |
| III.2.6 Verification examples . . . . .   | 54 |
| III.2.6.1 Square droplet . . . . .  | 54 |
| III.2.6.2 Droplet Oscillation . . . . .   | 56 |
| III.3 New density calculation . . . . .   | 58 |
| III.3.1 Method description. . . . .   | 58 |
| III.3.2 Verification examples . . . . .   | 61 |
| III.3.2.1 Square droplet . . . . .  | 61 |
| III.3.2.2 Rayleigh-Plateau instability . . . . .                                    | 63 |
| III.4 Continuous inlet flow . . . . .   | 66 |
| III.4.1 Method description. . . . .   | 66 |
| III.4.2 Verification example . . . . .  | 67 |
| III.5 Vibrations . . . . .  | 68 |
| III.5.1 Method description. . . . .   | 68 |
| III.5.2 Verification example . . . . .  | 69 |
| III.6 Case study: Application to the break-up of unidirectional water jet . . . . . | 70 |
| III.6.1 Literature review . . . . .   | 70 |
| III.6.2 Experimental set-up . . . . .   | 70 |
| III.6.3 SPH simulation set-up . . . . .   | 72 |
| III.6.4 Results . . . . .   | 73 |

III.7 Conclusion . . . . . 77

---

---

In the previous chapter (II), the state of the art of the tools in SPH and the special treatments for free surface flows were described. The aim of this chapter is to present the specific SPH model developed in this work to simulate the REP atomizer. This model is supported by the tools detailed in chapter II, but also requires original ones. Within this chapter, a comparison of the different correction techniques for applying surface tension to free surface flows in SPH is given. In the second part, a novel method for correcting the density near the free surface is presented. Finally, the changes applied to the SPH model in order to adapt it for the simulation of the REP atomization technique will be detailed.

### III.1 Program outline

The code used is the Weakly Compressible Smoothed Particle Hydrodynamics (WC-SPH) code of the Chair of Aerodynamics and Fluid Mechanics at Technical University Munich written in C++. The version of the code used for this project works on CPUs. The implemented SPH equations for force computation, wall boundary treatment and system update are the ones proposed and detailed by Adami *et al.* [63] and briefly explained in chapter II. This code is coupled with the open-source openFPM framework from the MOSAIC Group at the Center for Systems Biology in Dresden-Germany [129]. The library handles the domain decomposition and parallelization using openMPI. The performance of OpenFPM is listed in [129] for a strong scaling using 216 000 particles across an increasing number of processors from 1 to 1536 for 5000 time steps. The scaling normalised to 1 core is presented in Table III.1.

TABLE III.1: Strong scaling for the OpenFPM framework [129].

| #cores | Absolute timing (s) | Efficiency (%) |
|--------|---------------------|----------------|
| 1      | 1010.69             | 100.0          |
| 4      | 262.55              | 96.2           |
| 8      | 143.81              | 89.0           |
| 16     | 77.1                | 83.6           |
| 24     | 52.7                | 81.5           |
| 48     | 29.7                | 70.9           |
| 96     | 15.16               | 69.4           |
| 192    | 8.07                | 65.2           |
| 384    | 4.73                | 55.6           |
| 768    | 3.15                | 41.8           |
| 1536   | 2.2                 | 29.9           |

In pre-processing, the user defines the initial configuration of the numerical case using an eXtensible Markup Language (XML) file. For post-processing, the output files can be written into a comma-separated-values (CSV) file format or into a visualization toolkit (VTK) file format which can be visualized using ParaView. The code was initially developed for multi-phase problems and it is not fully adapted for the type of problem studied

here. To address this issue, several modifications were introduced. These modifications mainly include an implementation of a proper surface tension model, an introduction of a new coefficient for correcting the density near the free surface and an establishment of a continuous fluid inlet flow. All these models are explained in details within the scope of this chapter.

## III.2 Surface tension

The implementation of a proper surface tension model is of fundamental importance for describing the atomization process. The main issue when dealing with free surface flows is to adequately correct the surface properties for a better stability without affecting the physics involved in the fragmentation process. As mentioned in chapter II, the Continuum Surface Force (CSF) model was chosen to represent the surface tension force. With this approach, the surface tension force is calculated with the normal vector, the curvature of the interface particles and the surface delta function to smooth the surface tension force over a transition band near the free surface. In this section, the different methods for correcting the SPH approximations are compared in order to find the surface tension model that works best for the considered application.

### III.2.1 Surface particle detection

The three methods (Color function, Disk sectors and Cover vectors) described in chapter II for detecting surface particles were tested and compared with each other. Figure III.1 shows a comparison between these methods for a classical 2D dam break simulation. With all methods, surface particles can be detected, even when the surface undergoes major deformations. Each method requires an appropriate tuning of the threshold value. For the Color function method (equation II.45), using the Spike3 kernel function with a smoothing length of  $3 dx$ , the suggested range of the threshold value is  $0.8 \sim 0.9$ . This threshold can cover a wide range of geometries and problems, however, for complex geometries or important deformations near the interface, the threshold value should be adjusted. For the Disk sectors method, a disk of radius equal to the smoothing length divided into 8 sectors was considered. This configuration gives good results in terms of accuracy in detecting the surface particles. For the Cover vectors method, an angle of  $\pi/3$  was considered. Similarly to the other two methods, the value of the threshold angle plays an important role in the accuracy in detecting surface particles.

Nevertheless, with the Color function method, low density zones inside the fluid can be wrongly detected as free-surface, see figure III.1a (right side). In this case, non-physical surface tension force will be applied to these particles. The computational load is another important parameter that must be considered in the final choice of the appropriate method.

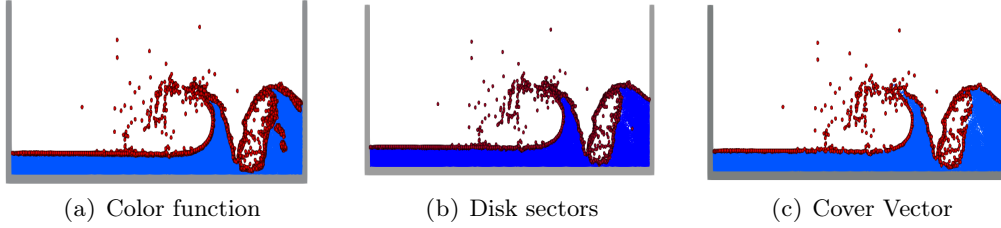


FIGURE III.1: Surface particles detection (red particles): comparison between the three methods described in II.

Figure III.2 presents the computational time as a function of the number of particles for the three methods for the dam break test case in 2D and 3D. The number of particles and the computational time are normalized with respect to the simulation having the smallest number of particles. Because the Disk sector and the Cover vector methods are more time-consuming compared to the simple summation, it is interesting to combine these two techniques. The first step consists in detecting the surface particles using the Color function and then the Cover vector method is performed only on surface particles detected in the first step.

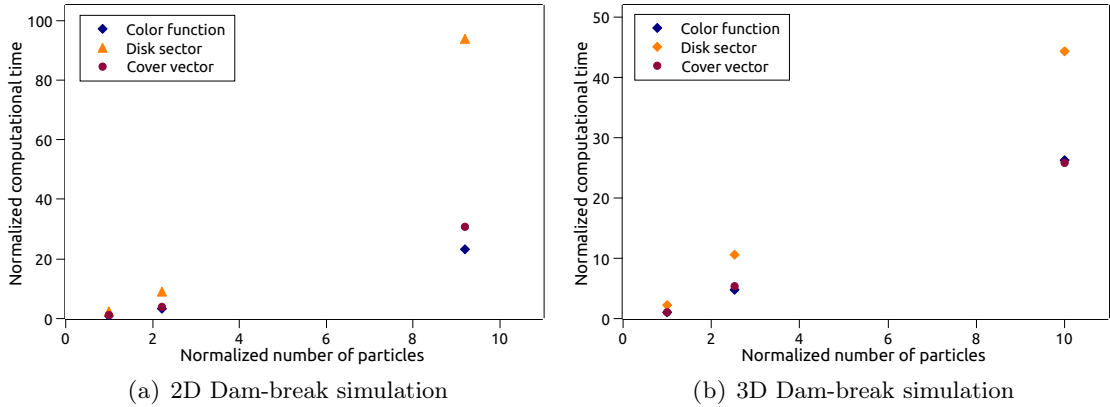


FIGURE III.2: Computational time as a function of the number of particles in 2D and 3D.

### III.2.2 Normal vector

The normal vector is required to identify the direction of the surface tension force. Its norm is also used to calculate the surface tension force intensity for particles that are in the transition band. The transition band where the surface tension force will be applied will consist of the particles that are in the support domain of the surface particles and have well defined normal vectors according to equation II.51. The different techniques to compute the normal vectors for free surface flows described in chapter II are compared in this section. Figure III.3 presents a comparison between the different methods for normal vectors calculation. For this comparison, a disk of radius equal to 5 mm is considered. The particle spacing  $dx$  is equal to 0.3 mm and a total number of 865 particles is considered.

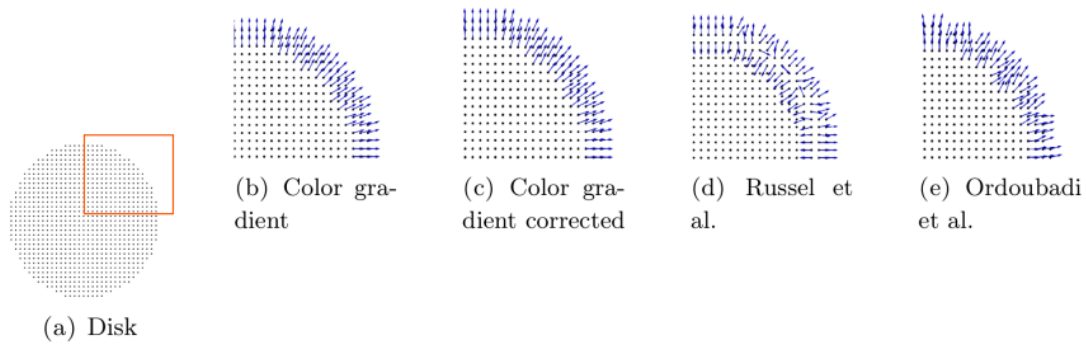


FIGURE III.3: Representation of the normal vectors in the transition band.

The results show that the color gradient method, with or without the correction, presents the most regular normal vectors (see figure III.3). The method presented by Russell *et al.* [100] is only valid for the first layer of particles (see figure III.3 d). The method presented by Ordoubadi *et al.* [111] gives acceptable normal vectors for regular surfaces but, near the corners, the normal vectors seem to be slightly crooked. Based on this comparison, the color gradient correction will be used to define the normal vectors for the surface tension model.

### III.2.3 Surface delta function

According to equation II.52, the surface delta function  $\delta_s$  is usually taken proportional to the norm of the normal vector. The comparison between different surface delta functions is presented in figure III.4. In order to compare them, the normal vectors are normalized with respective maximum value.

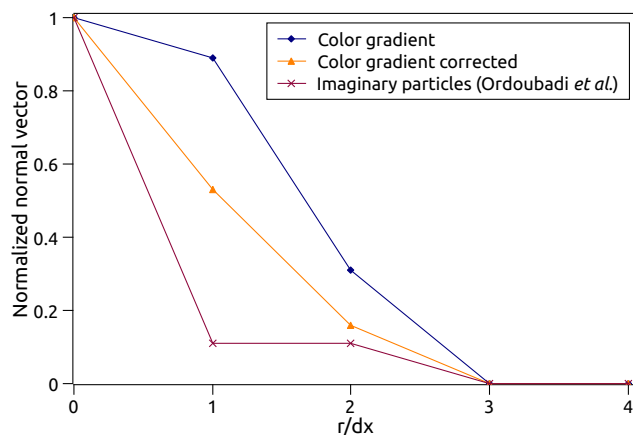


FIGURE III.4: Comparison between the different surface delta functions.

The results show that the smoothing over the transition band, with and without correction for the kernel gradient, are completely different, despite the fact that the direction of the normal vectors are almost the same. We can conclude, that the surface delta function profile using the kernel gradient correction presents the smoothest decrease for the surface tension force intensity and, consequently, leads to a potentially more stable scheme.



### III.2.4 Curvature

A similar approach was adopted to compare the different methods for estimating the curvature  $k$  of the free surface particles in SPH detailed in chapter II. A comparison between these different methods is presented in figure III.5. They all compute the curvature as the divergence of the normal vector. For this comparison, the same disk of radius  $R = 5$  mm was considered with 865 particles. In order to eliminate the effect of the normal vector directions and correction techniques, prescribed normal vectors are used, that is to say that the normal vector of particle  $i$  is set to be exactly:

$$\vec{n}_i = \vec{r}_i - \vec{r}_{center} \quad (\text{III.1})$$

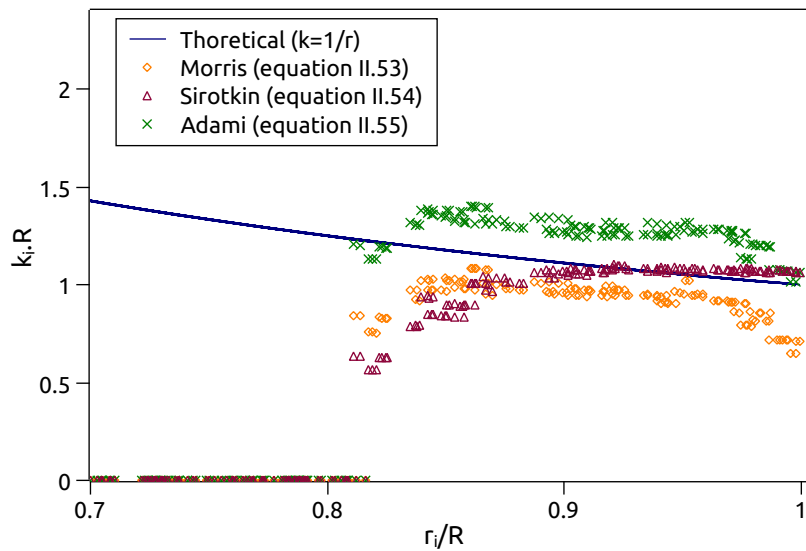


FIGURE III.5: Estimating the curvature  $k_i$  for particles located at  $r_i$  near the free surface of a 2D disk.

According to the results presented in figure III.5, the three methods give acceptable results for the curvature estimation in 2D. We are more interested in the region close to the free surface ( $r_i/R > 0.95$ ) where the surface delta function is maximum. In Adami [102] and Morris [88] models, the curvature tends to decrease slightly near the free surface because of the lack of the full support. On the other hand, the correction matrix for the kernel gradient compensates the missing particles near the free surface and hence gives more accurate results. Thus, equation II.54 [75] with the kernel gradient correction will be used to calculate the curvature for the particles inside the transition band. Note that Ordoubadi *et al.* [111] used the imaginary particles to calculate the curvature based on equation II.53.

According to Fürstenau *et al.* [113], equation II.54 overestimates the curvature calculation by almost a factor 2 for 3D simulations. Indeed, we observed this effect with a sphere of radius  $R = 5$  mm. The results are presented in figure III.6. The method presented by Fürstenau *et al.* to calculate the curvature in the local basis instead of global basis gives

good results, however it is computationally more expensive than calculating the curvature by applying equation II.54. Thus, the idea was to check if the curvature can be simply corrected by dividing with a constant coefficient. For this objective, different resolutions were tested and the method presented by Fürstenau *et al.* was compared to the results obtained by simply dividing the curvature by a factor 2. Table III.2 presents the results of this comparison. The root mean square deviation (equation III.2) and the maximum relative deviation (equation III.3) are presented.

$$RMSD = \sqrt{\frac{\sum (value_{case1} - value_{case2})^2}{n}} \quad (III.2)$$

$$MRD = \max \left( \frac{|value_{case1} - value_{case2}|}{value_{case1}} \right) \quad (III.3)$$

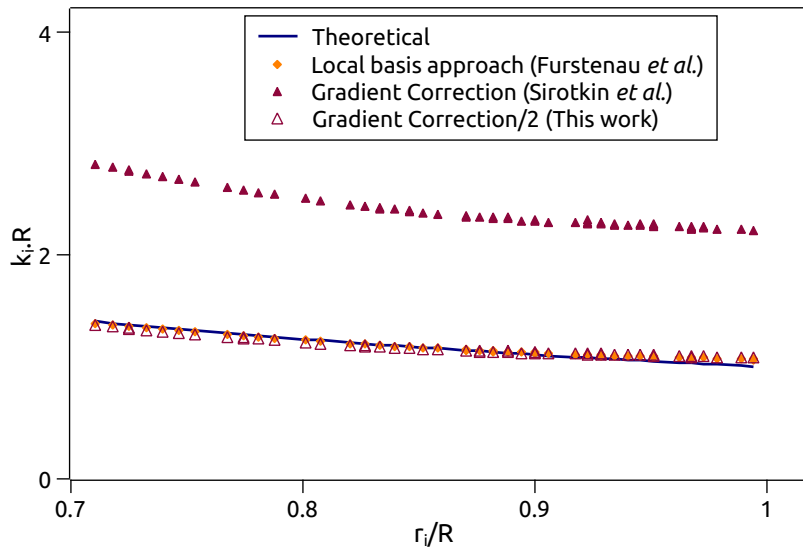


FIGURE III.6: Comparison of different methods for estimating the curvature  $k_i$  of particles located at  $r_i$  near the free surface of a sphere.

TABLE III.2: Comparison of curvature estimation between the method presented by Fürstenau *et al.* and dividing the curvature of equation II.54 by a factor 2 for different particle resolutions.

|        | RMSD | MRD   |
|--------|------|-------|
| $dx_1$ | 10%  | 10 %  |
| $dx_2$ | 4%   | 4 %   |
| $dx_3$ | 1.2% | 1.8 % |
| $dx_4$ | 1%   | 0.7%  |

Given the results presented above, we can roughly consider that the curvature calculated by equation II.54 can be used as such in 2D and simply divided by a factor 2 to be correct in 3D. Nonetheless, the surface tension force is linearly proportional to the curvature and therefore the numerical calibration of the surface tension force should be adjusted with the appropriate choice of the  $\Lambda$  coefficient in equation II.42.

---

Because for special geometries, the curvature calculation can be erroneous, an additional correction was applied to the curvature calculation. The curvature was limited as a function of the discretization of the system as follows:

$$|k_i| = \min(k_i, \frac{DIM - 1}{3dx}) \quad (\text{III.4})$$

### III.2.5 Surface tension model

The calculation of the surface properties and the accurate representation of the surface tension play an important role in the numerical stability of the simulation. After the comparison of the most common methods found in literature for representing and correcting surface properties, the adopted surface tension model can be described as follows:

- Surface particle detection  
Combination of two methods to reduce the computational cost: first, a coarse method is used: surface particles are detected using the Color function (equation II.45). In a second step, the Cover vector method (equation II.46), which is a refined but more expensive method, is applied only on particles detected from the first step.
- Normal vector calculation  
Gradient of the color function using the correction matrix (equation II.47)
- Curvature calculation  
Divergence of the unit-normal vector using the correction matrix (equation II.54). This curvature is divided by a factor 2 for 3D simulations. Finally, a threshold is applied to the curvature to limit its value according to the discretization of the system.

The implementation of the employed surface tension force model is detailed in the algorithm below (algorithm 1).

---

**Algorithm 1** Surface tension force.

---

```

for all particles  $i$  do
  Define surface particles
  if particle  $i$  is a fluid particle then
    Calculate the correction matrix (equation II.48) and the corrected kernel (equation II.49)
    Calculate the normal vectors (equation II.47)
    Filter the normal vectors (equation II.51)
    Calculate the curvature (equation II.54)
    Apply surface tension force (equation II.42)
  end if
end for

```

---

### III.2.6 Verification examples

#### III.2.6.1 Square droplet

One common test case is the transformation of a square droplet into a circular droplet under the effect of surface tension. Following the example in Adami et al. [102], an initial square of  $L = l = 0.6$  is placed in the center of a square domain ( $10L$ ). The particle spacing is equal to 0.02 and a total number of 900 particles is considered. The fluid parameters are listed in table III.3. For all the test cases, a smoothing length of  $R_c = 3h$  is used. Figure III.7 presents the initial and final stable shape of the droplet after  $t = 1$ .

TABLE III.3: Square droplet : Simulation parameters

| Parameter                    | Value |
|------------------------------|-------|
| Density ( $\rho$ )           | 1     |
| Dynamic viscosity ( $\nu$ )  | 0.2   |
| Surface tension ( $\sigma$ ) | 1     |

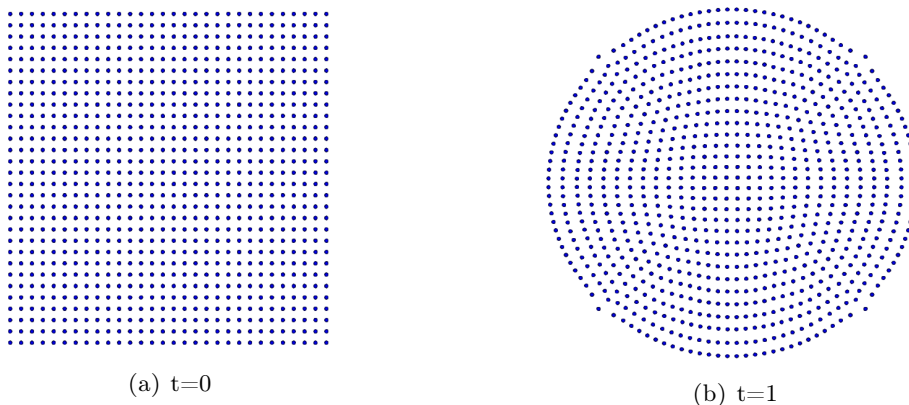


FIGURE III.7: Square droplet test case 2D: particles positions at  $t=0$  and  $t=1$ .

The pressure profile inside the droplet at  $t = 1$  is calculated for different spatial resolutions and compared to the Laplace pressure drop given by equation III.5. Figure III.8 shows that the pressure profile is almost constant inside the droplet and is equal to the theoretical Laplace pressure with some fluctuations near the free surface. Note, using this verification example the calibration of  $\Lambda$  in equation II.42 gives  $\Lambda = 3$  in 2D.

$$p = \begin{cases} \frac{\sigma(\pi)^{\frac{1}{2}}}{L} & \text{DIM}=2 \\ \frac{2\sigma}{L} \left(\frac{4\pi}{3}\right)^{\frac{1}{3}} & \text{DIM}=3 \end{cases} \quad (\text{III.5})$$

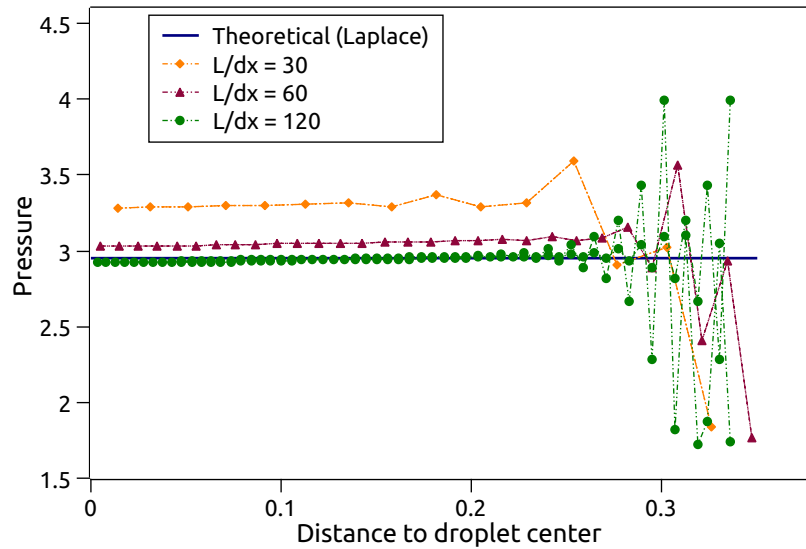


FIGURE III.8: Pressure profile inside the droplet at  $t=1$  for different resolutions (2D test case).

The square droplet was also tested in 3D with the same set up as for the 2D simulation. After  $t = 1$ , a stable spherical droplet is obtained as shown in figure III.9. Additionally, the pressure profiles inside the droplet for different spatial resolutions are presented in figure III.10. The calculated pressure profiles agree well with the Laplace law. Here, the value  $\Lambda = 5$  is used to obtain the best fit for 3D simulations.

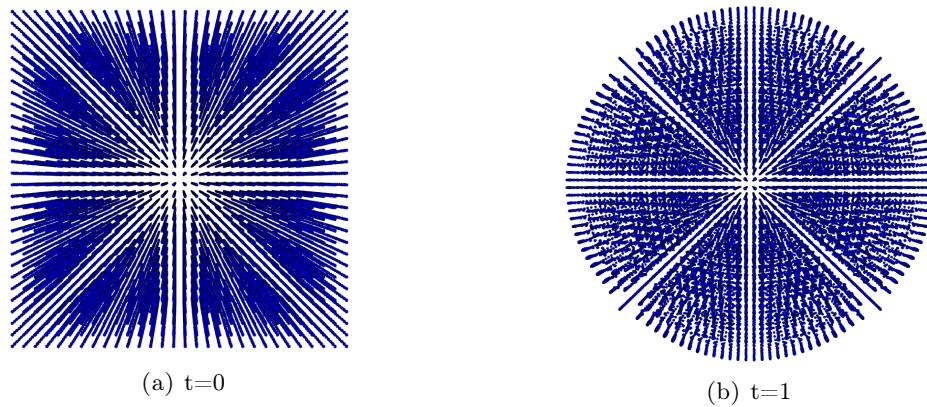
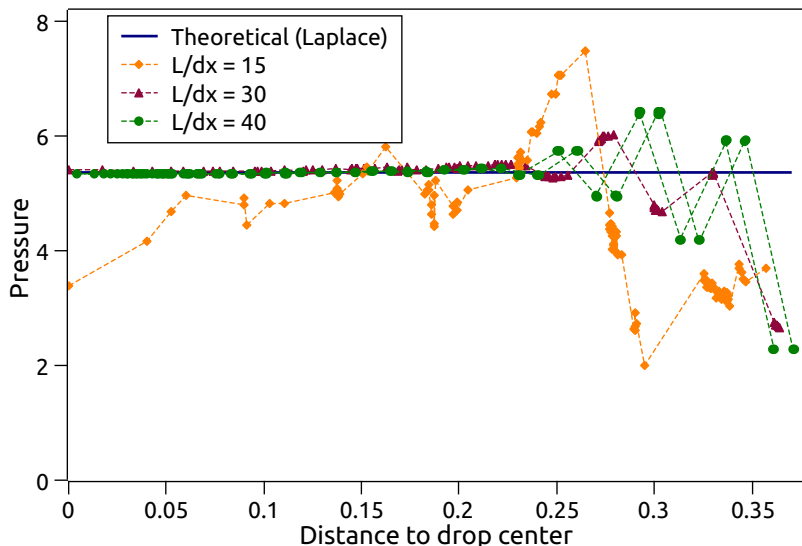


FIGURE III.9: Square droplet test case 3D: particles positions at  $t=0$  and  $t=1$ .

FIGURE III.10: Pressure profile inside the droplet at  $t=1$  for different resolutions (3D test case).

### III.2.6.2 Droplet Oscillation

Another dynamic test case is the droplet oscillation in 2D under the effect of surface tension. Following the example in Adami et al. [102], instead of starting from an elliptic droplet, an initial velocity field is prescribed as follows:

$$u_x = -u_0 \frac{x}{r_0} \left( 1 - \frac{y^2}{r_0 r} \right) \exp \left( -\frac{r}{r_0} \right) \quad (\text{III.6})$$

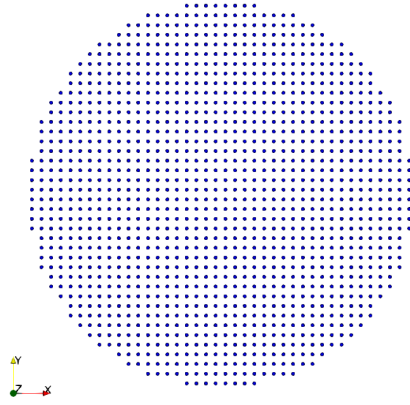
$$u_y = u_0 \frac{y}{r_0} \left( 1 - \frac{x^2}{r_0 r} \right) \exp \left( -\frac{r}{r_0} \right) \quad (\text{III.7})$$

The circular droplet of radius  $R = 0.2$  is placed at the center of the computational square domain. The total number of particles is equal to 1264 with a particle spacing equal to 0.01. The simulation parameters are listed in table III.4. The density and dynamic viscosity are taken equal to  $\rho = 1$  and  $\nu = 0.05$ , respectively. The surface tension coefficient is set to  $\sigma = 1$ . In this example,  $u_0$  and  $r_0$  were taken equal to 2 and 0.05, respectively. Figure III.12 shows the evolution of the particles positions with time. The distance between the top particle along the  $y$  axis and the center of the droplet is plotted over time in figure III.12. Once again, to study the numerical convergence of this method, three simulations were conducted with different spatial resolutions: 1264, 2230 and 5024 particles.

TABLE III.4: Square droplet : Simulation parameters

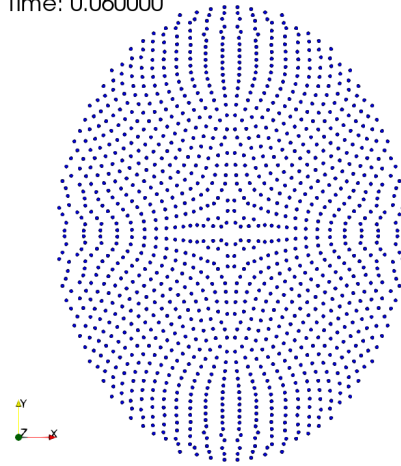
| Parameter                      | Value |
|--------------------------------|-------|
| Droplet radius ( $r$ )         | 0.2   |
| Initial perturbation ( $u_0$ ) | 10    |
| Initial perturbation ( $r_0$ ) | 0.05  |
| Density ( $\rho$ )             | 1     |
| Dynamic viscosity ( $\nu$ )    | 0.05  |
| Surface tension ( $\sigma$ )   | 1     |

Time: 0.000000



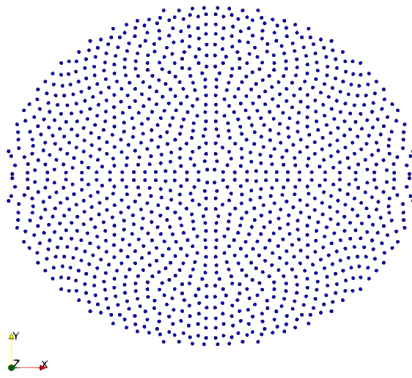
(a)

Time: 0.060000



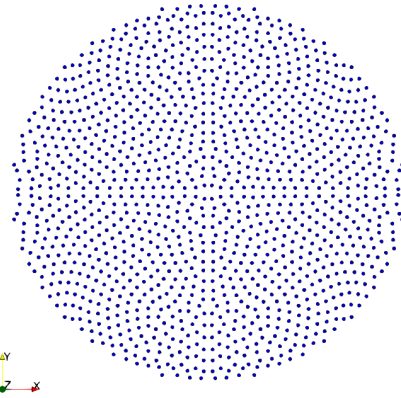
(b)

Time: 0.180000



(c)

Time: 0.230000



(d)

FIGURE III.11: Particles positions at different times.

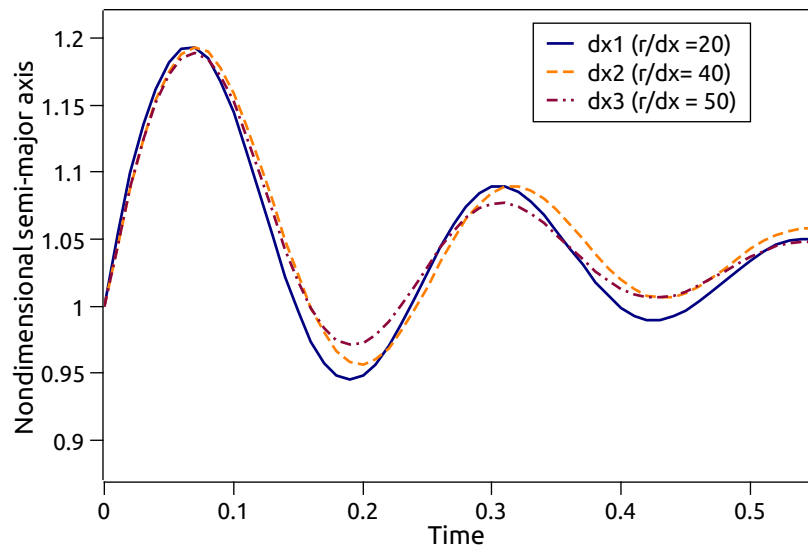


FIGURE III.12: Semi major axis as a function of time for different resolutions.

According to figure III.12, the SPH period of the oscillations is  $\Gamma_{SPH} = 0.23$ . This period remains constant within 5 % for all three resolutions. A good agreement was found by comparing the SPH period with the theoretical period of oscillations given by:

$$\Gamma_{theoretical} = 2\pi\sqrt{\frac{R^3\rho}{6\sigma}} = 0.229 \quad (\text{III.8})$$

### III.3 New density calculation

#### III.3.1 Method description

From the different density correction techniques summarized in chapter II, the Shepard density filter is the most common one. In this case, the density is calculated using the density evolution formula II.17. Then, the derived density is corrected every  $n$  time steps by the Shepard summation as follows:

$$\rho_i = m_i \frac{\sum_j W_{ij}}{\sum_j V_j W_{ij}} \quad (\text{III.9})$$

Note, equation III.9 can be written in the form of a corrective factor  $C_i$ , which will depend in this work on the distance of each particle to the free surface and the local curvature [130]:

$$\rho_i = C_i m_i \sum_j W_{ij} \quad (\text{III.10})$$

If we consider only the geometric aspect, then the correction coefficient  $C_i$  can be expressed as follows:

$$C_i \approx \frac{V_{SD}}{V_{SD} - V_{empty}} \quad (\text{III.11})$$

where  $V_{SD}$  and  $V_{empty}$  are the volume of the support domain of particle  $i$  and the empty volume represented by the missing particles at the free surface, respectively. Figure III.13 represents the support domain area and the empty volume of a particle at a distance  $d$  from the free surface. The support domain is represented by the small circle of radius  $R_c$  and the empty volume is represented by the hatched moon. The curvature of the free surface is equal to  $k$ .



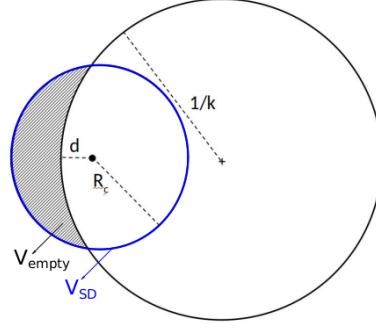


FIGURE III.13: Representation of the empty volume (hatched moon) for a particle at a distance  $d$  from the free surface.

In fact, the impact of missing neighbours on the density calculation depends on their location. The impact of removing a distant neighbour is much smaller than the impact of a closer one. Therefore, the weight of each missing particle, represented by the kernel function, should be taken into account when expressing  $C_i$ . Equation III.11 will be then modified to:

$$C_i = \frac{1}{1 - \frac{\int_{V_{empty}} W(r) dV}{\int_{V_{SD}} W(r) dV}} \quad (\text{III.12})$$

Because the kernel functions are normalized, the integral of  $W$  over all the support domain should theoretically be equal to 1 ( $\int_{V_{SD}} W(r) dV = 1$ ). Using spherical coordinates,  $dV$  can be calculated by:

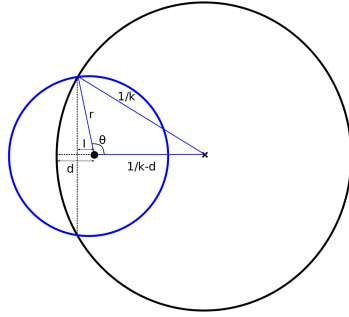
$$dV = r^2 \sin(\phi) d\phi d\varphi dr \quad (\text{III.13})$$

Thus, the integral over the empty volume can be expressed as:

$$\int_{V_{empty}} W(r) dV = \int_0^\theta \int_0^{2\pi} \int_d^{R_c} W(r) r^2 \sin(\phi) d\phi d\varphi dr \quad (\text{III.14})$$

where  $d$  represents the distance between particle  $i$  and the free surface and  $\theta$  varies from 0 to  $\arccos(I/r)$ ,  $I$  being the distance between the center and the intersection of the two spheres. By solving equation III.14 we obtain:

$$\int_{V_{empty}} W(r) dV = 2\pi \int_d^{R_c} W(r) r(r - I) dr \quad (\text{III.15})$$


 FIGURE III.14: Representation of the intersection distance  $I$ .

The intersection distance  $I$  can be calculated using the generalized Pythagorean theorem as a function of  $r$ ,  $d$  and  $k$  which represents the curvature of the surface particle (see figure III.14):

$$\left(\frac{1}{k}\right)^2 = r^2 + \left(\frac{1}{k} - d\right)^2 - 2 \cos(\theta) r \left(\frac{1}{k} - d\right) \quad (\text{III.16})$$

with  $\cos(\theta) = -\cos(\pi - \theta) = -\frac{I}{r}$ , we obtain:

$$I = -\frac{r^2 + \left(\frac{1}{k} - d\right)^2 - \left(\frac{1}{k}\right)^2}{2\left(\frac{1}{k} - d\right)} \quad (\text{III.17})$$

This the integral over the empty volume becomes:

$$\int_{V_{\text{empty}}} W(r) dV = \int_d^{R_c} W(r) 2\pi r \left[ r + \frac{r^2 + \left(\frac{1}{k} - d\right)^2 - \left(\frac{1}{k}\right)^2}{2\left(\frac{1}{k} - d\right)} \right] dr \quad (\text{III.18})$$

For 3D simulations, this integral can be expressed as a function of  $\delta = \frac{d}{h}$  and  $\varrho = \frac{1}{|k|h}$ . The kernel function used in this case is the Spike function with  $R_c = 3h$  (see table II.1).

Two cases must be considered. For positive curvatures, we have:

$$\int_{V_{\text{empty}}} W(r) dV = \frac{(\delta - 3)^5 (-4\delta^2 + 3\delta + 28\delta\varrho + 42\varrho + 27)}{20412(\delta - \varrho)} \quad (\text{III.19})$$

and for negative curvatures:

$$\int_{V_{\text{empty}}} W(r) dV = \frac{(\delta - 3)^5 (-4\delta^2 + 3\delta - 28\delta\varrho - 42\varrho + 27)}{20412(\delta + \varrho)} \quad (\text{III.20})$$

The same scheme can be used in 2D simulations by integrating over a surface instead of a volume. However, the analytical solution for surface integrals is surprisingly not as simple as for 3D cases. Thus, numerical integration is necessary in these cases. The same problem was reported by Herant [127] although he used another kernel function for the integration.

It should be noted that when  $\delta$  tends to or is bigger than  $\varrho$ , equation III.19 can diverge. To avoid this problem, the correction coefficient  $C_i$  is only calculated for values of  $\varrho$  bigger

---

than the maximum value of  $\delta$  defined by the radius of the support domain, which is in this case equal to 3. For values of  $\varrho$  below 3, the standard Shepard summation (Equation III.9) is used for the density calculation. The implementation of this correction technique is detailed in algorithm 2.

---

**Algorithm 2** Density Computation.

---

```

At t=0 initial calculation of  $\rho_i$  with equation III.9
for all particles  $i$  do
  Identify surface particles
  Calculate curvature  $k_i$ 
end for
for all particles  $i$  do
  if particle  $i$  is a surface particle then
    Set  $\delta = \frac{1}{2}$ 
    Set  $\varrho = \frac{1}{|k_i|h}$ 
  else
    Find the nearest surface particle  $j$ 
    Compute the distance  $d = d_{ij} + \frac{h}{2}$ 
    Set  $\delta = \frac{d}{h}$ 
    Set  $\varrho = \frac{1}{|k_j|h}$ 
  end if
  if  $\varrho > 3$  then
    Compute  $C_i$  with equation III.12 and  $\rho_i$  with equation III.10
  else
    Compute  $\rho_i$  with equation III.9
  end if
end for

```

---

### III.3.2 Verification examples

#### III.3.2.1 Square droplet

The same set up as the square droplet test case in 3D presented in the previous section ( $L/dx = 15$ ) was considered for this test case. The spherical droplet formed after  $t=2$  is presented in figure III.15 for three different methods of density evaluation.

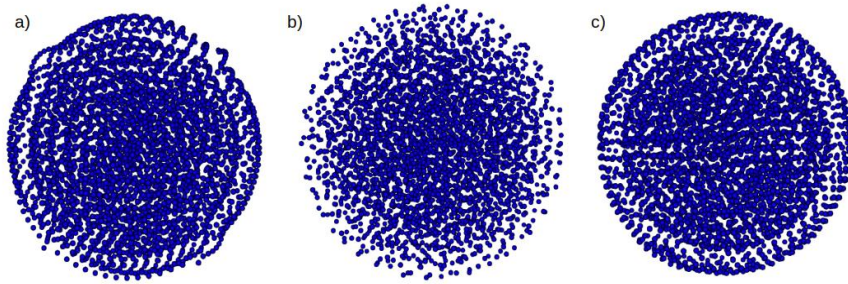


FIGURE III.15: Particles positions at  $t=2$ : a) Density evolution b) Density evolution with Shepard filter ( $n=30$ ) and c) New correction based on curvature.

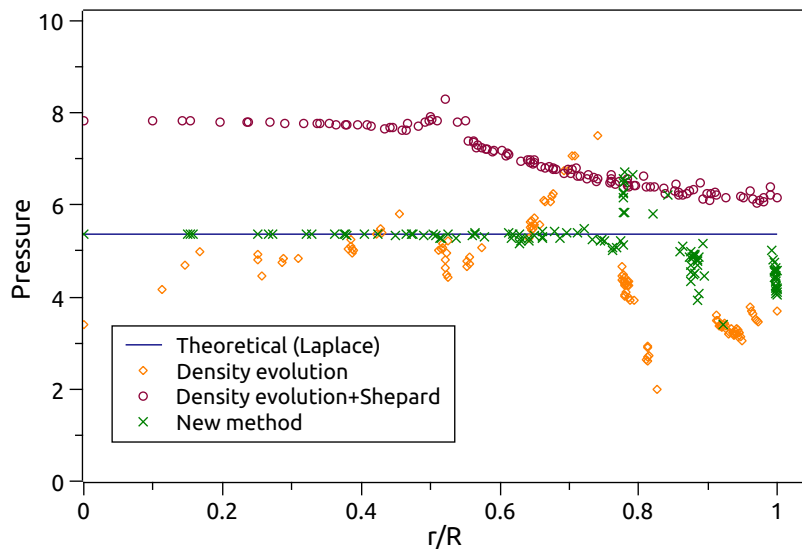


FIGURE III.16: Pressure inside the droplet as a function of the distance to the center.

Figure III.16 presents the pressure inside the droplet as a function of the distance to the center (all particles are considered). With the new method, the homogeneity of the density field is strongly improved. By comparing the results of the three methods, it can be found that the new method outperforms the existing approaches for the particle distribution at the interface.

Table III.5 shows the percentiles of the number of particles as a function of pressure, for a better comparison between the density calculation methods. It can be seen that with the new method, the pressure variation is smaller, with almost all particles having a pressure variation within 30% of the theoretical Laplace pressure.

TABLE III.5: Fraction in (%) of particles having a pressure within a certain range around Laplace pressure.

| Method            | Pressure    |              |              |              |
|-------------------|-------------|--------------|--------------|--------------|
|                   | $p \pm 1\%$ | $p \pm 10\%$ | $p \pm 30\%$ | $p \pm 50\%$ |
| Density evolution | 1.066       | 25           | 60           | 100          |
| New method        | 20          | 54           | 99           | 100          |

---

### III.3.2.2 Rayleigh-Plateau instability

The Rayleigh-Plateau test case was first presented by Dai and Schmidt [131] using a new moving mesh algorithm and then reproduced by Olejnik and Szewc [132] using SPH with two phases. For this simulation, we consider a fully periodic cubic ( $L \times L \times L$ ) domain containing in its center a liquid column of length  $L$  and a radius  $r = L/10$ . An initial perturbation is imposed by a sinusoidal velocity field applied to the liquid column in its longitudinal direction:

$$u_x = u_0 \sin\left(\frac{2\pi x}{L}\right) \quad (\text{III.21})$$

Since the particles are placed on a Cartesian grid and do not form a perfect cylinder, we let the system first relax by imposing a high viscosity. Then, we switch to the real properties of water before applying the velocity perturbation. The dimensionless numbers describing this case are the Reynolds number  $Re = 18$  and the Weber number  $We = 1.4$  calculated based on  $u_0$ . The simulation parameters are listed in table ???. The dimensionless time is defined by:

$$T_d = \frac{t}{\sqrt{\frac{\rho r_0^{DIM}}{\sigma}}}. \quad (\text{III.22})$$

TABLE III.6: Raleigh-Plateau instability: Simulation parameters

| Parameter                      | Value                    |
|--------------------------------|--------------------------|
| Fluid                          | Water                    |
| Jet diameter ( $D_{jet}$ )     | 3.3 $\mu\text{m}$        |
| Initial perturbation ( $u_0$ ) | 5.5 m/s                  |
| Density ( $\rho$ )             | 1000 kg/m <sup>3</sup>   |
| Dynamic viscosity ( $\nu$ )    | 0.001 N.s/m <sup>2</sup> |
| Surface tension ( $\sigma$ )   | 0.072 N/m                |

The simulations have been performed with a total number of fluid particles equal to 18000, which corresponds to  $dx = L/82$ . Figure III.17 shows several snapshots at different times for the density evolution with the Shepard density filter and the new approach. Clearly, the new method shows more stable results compared to the classic density evolution with the Shepard density filter. It should be noted that the two pictures on the last row correspond to the particles positions after the break-up. With this new density formulation, only 0.005% of the total particle number disintegrate (as compared to 1.2% for the standard method). Because the break-up does not occur at the same moment for both cases, the time  $T_d$  is not the same. The break-up time is defined as the time when the ligament diameter between droplets is composed of less than two particles.

We can clearly see from figure III.17 that the break-up with the new method is much smoother. With the classical algorithm, unstable flying particles are seen at the moment of the break-up. This phenomenon can be explained by two reasons: the density evolution with no additional correction can accumulate errors with time, and more important, for this specific test case with fragmentation, the density changes drastically when a bulk

particle becomes a surface particle, thus creating instabilities.

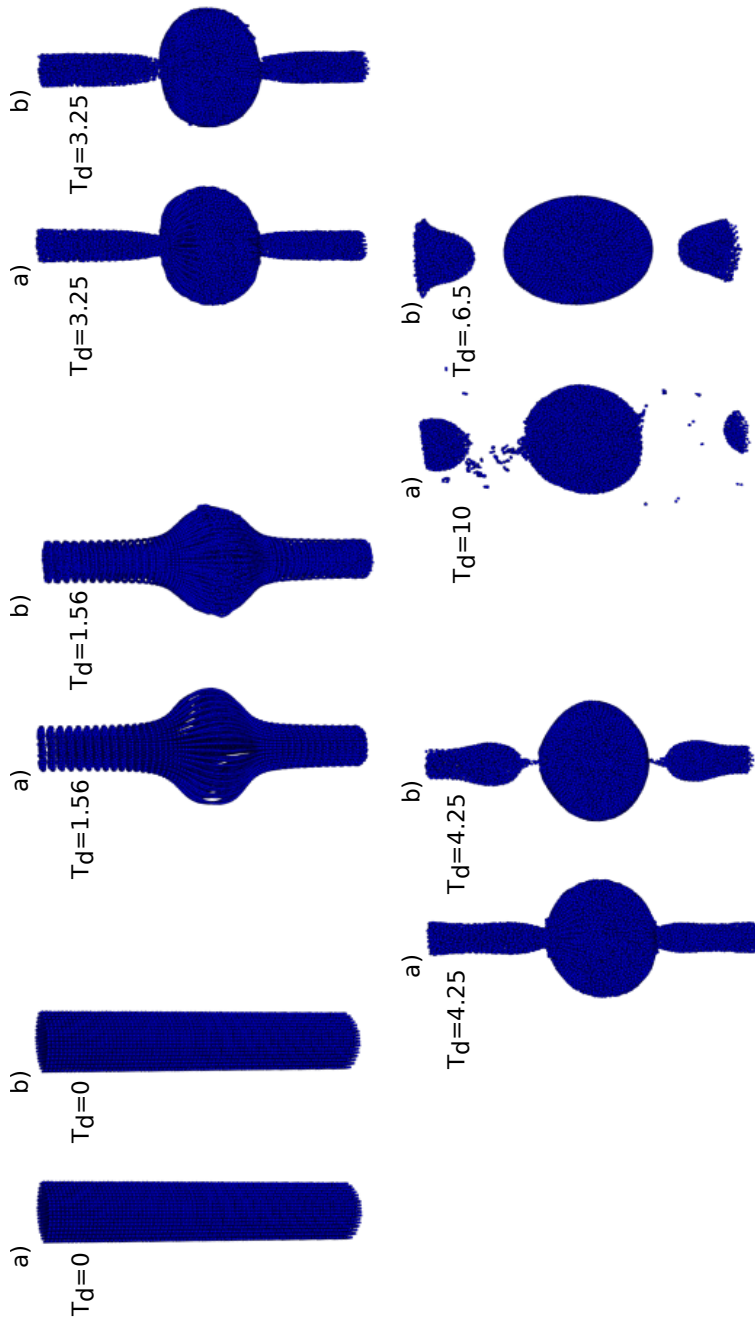


FIGURE III.17: Particles positions at different times for two density algorithms: a) Density evolution and Shepard summation ( $n=30$ ) and b) New correction based on curvature.

The correction coefficient for the Shepard technique ( $1/\sum_j V_j W_{ij}$ ) was compared with the new correction coefficient ( $C_i$  in equation III.12). Figure III.18 presents these two correction coefficients for surface particles as a function of their position along the column axis. The main difference is that this coefficient is slightly more dispersed in the case of the Shepard correction compared to the new technique presented here.

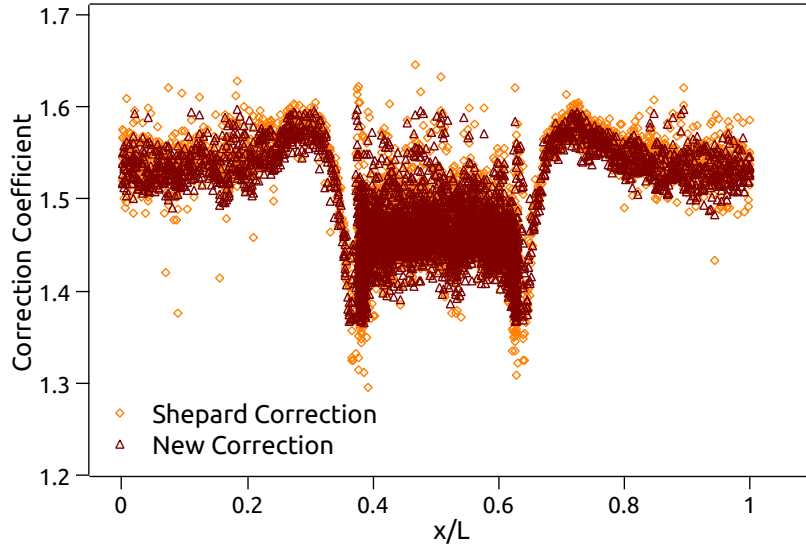


FIGURE III.18: Correction coefficients as a function of the position of the particles along the jet axis.

To compare both methods, the SPH simulations have been performed at different resolutions. Table III.7 presents the number of flying particles for each case. The result shows that the new method presents stable results, even for simulations with a lower resolution.

TABLE III.7: Number of "flying" particles for each method as a function of the system resolution.

| Resolution ( $L/h$ ) | 55         | 66         | 82          |
|----------------------|------------|------------|-------------|
| Method               | 30 (0.6 %) | 96 (1 %)   | 217 (1.2%)  |
| New method           | 4 (0.08 %) | 1 (0.01 %) | 1 (0.005 %) |

For a quantitative comparison, the relative disturbance size ( $\frac{r_{max}(t)-r_0}{r_0}$ ) as a function of time is presented in figure III.19 for the highest resolution. The results show that the growth dynamics for the two methods agree well with the reference data presented by Dai and Schmidt, even though the break-up time is not the same. Furthermore, the droplet diameter can be estimated from the volume of the liquid within the disturbance wavelength  $\lambda$  [17]:

$$D_{droplet}^3 = 6\lambda R_{jet}^2 \quad (\text{III.23})$$

For both cases, the droplet diameter after the break-up agrees well with the theoretical one, with an error around 5%.

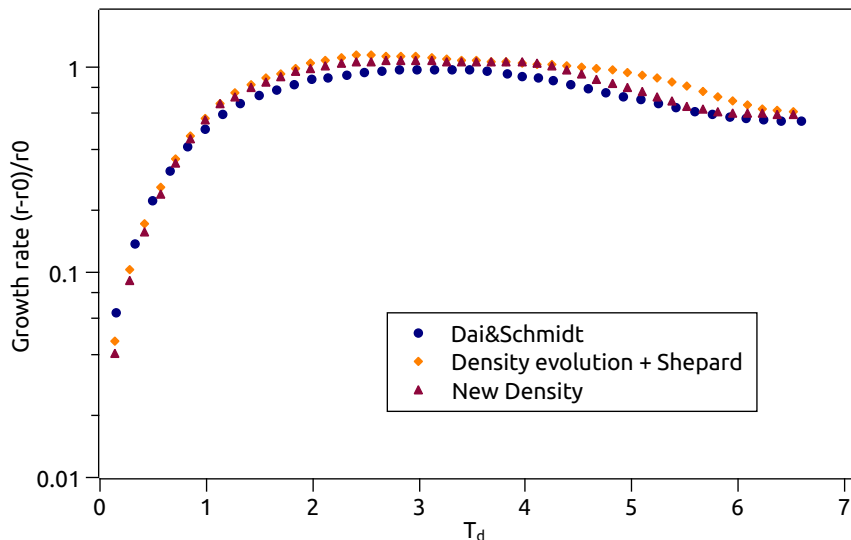


FIGURE III.19: Disturbance growth process in time: Comparing the growth rate as a function of time with the reference data from Dai and Schmidt.

This new method proved its efficiency for simulating free surface flows undergoing strong topological variations under the effect of surface tension force. We found the method to work best when the interface is well resolved with smoothed shapes. In fact, the density calculation presented above depends significantly on the curvature and the distance of each particle from the free surface. Thus, these two parameters must be calculated with great precision in order to have a reliable output result.

## III.4 Continuous inlet flow

### III.4.1 Method description

Because of the high computational cost of SPH method, the number of particles in the domain must be limited. Without a continuous and stable flow circulations, the application of SPH would be then restricted to short scale applications and/or small spatial domains and could not be extended to a level relevant for industrial applications. Therefore, for the simulation of the REP atomizer a correct and efficient method for the treatment of inflow and outflow boundaries is required. One of the first techniques was proposed by Lee *et al.* [133] for an open channel laminar flow. The idea is to apply periodic boundary conditions, so that each particle going out of the domain on one side will be re-injected on the opposite side. This method is straightforward and simple to implement, however it can only be applied when the flow is driven by an external force. A more flexible framework for modelling inlet and outlet boundaries was proposed by Lastiwka *et al.* [134]. It was then modified and extended by other authors, see among others [94, 135, 136]. The idea is to create buffer zones in which particles are created or removed. The boundary conditions are prescribed for the particles in these inlet and outlet zones. This method is flexible enough for imposing various analytical forms of boundary conditions. Another approach based on mirror particle technique similar to the approach applied for solid wall boundary



conditions is described in [137].

For this present work, we chose to adopt the buffer zones approach. The domain is divided into two parts: the inflow zone and the fluid zone. At the outflow, open boundary conditions are imposed: after the atomization, the fragmented particles will travel for a short distance in the domain and then leave it. The inflow zone is taken as wide as the kernel radius. In this zone, the particles are distributed on a Cartesian grid and move according to an imposed velocity profile and pressure field. Once a particle leaves the inflow zone, it becomes a fluid particle and a new inflow particle is created at the entrance of the inflow zone. The new fluid particle will then evolve according to the SPH equations. The sketch explaining the treatment of the inflow boundary condition and the creation of new fluid particles is presented in figure III.20. The algorithm is explained in algorithm 3.

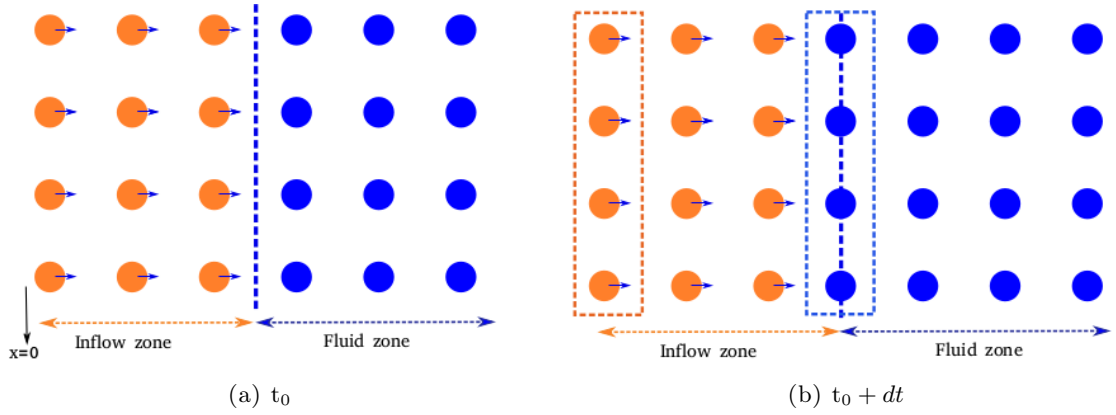


FIGURE III.20: Sketch of the process of particles creation.

---

**Algorithm 3** Continuous inlet flow.

---

At  $t=0$  create inflow particles with given pressure and velocity profile

**for all** particles  $i$  in the inflow zone **do**

**if** position of  $i$   $>$  threshold position **then**

    Create a new fluid particle at the same position having the same pressure and velocity

    Create a new inflow particle at position  $x = \frac{dx}{2}$ ,  $y$  and  $z$  are the same as the newly created fluid particle

    Delete particle  $i$

**end if**

**end for**

---

### III.4.2 Verification example

The continuous inlet flow approach was tested with the 2D Poiseuille flow between stationary infinite plates. For this test case, the fluid density  $\rho$  and viscosity  $\nu$  were taken equal to 1 and 0.01, respectively. The channel width  $L$  is taken equal to 0.8 and the driving force  $F_d$  is considered to be 0.1. With this configuration, the total number of fluid particles

between the two plates is 741. The velocity profile at the steady state is given by:

$$u_x(y) = \frac{F_d}{2\nu}y(L - y) \quad (\text{III.24})$$

This velocity profile was imposed to the inlet particles. The main objective of this test is to ensure that the steady state will be maintained for a long time and that the inflow configuration will not affect the stability of the fluid flow or change its hydrodynamic behaviour. The results are presented in figure III.21. The comparison shows a good agreement between the analytical and numerical velocity profile. The root mean square deviation (RMSD equation III.2) and the maximal relative deviation (MRD equation III.3) of the velocity between the analytical solution and the SPH with inflow boundary condition were calculated and found to be  $5.9 \times 10^{-5}$  and 2.7%, respectively.

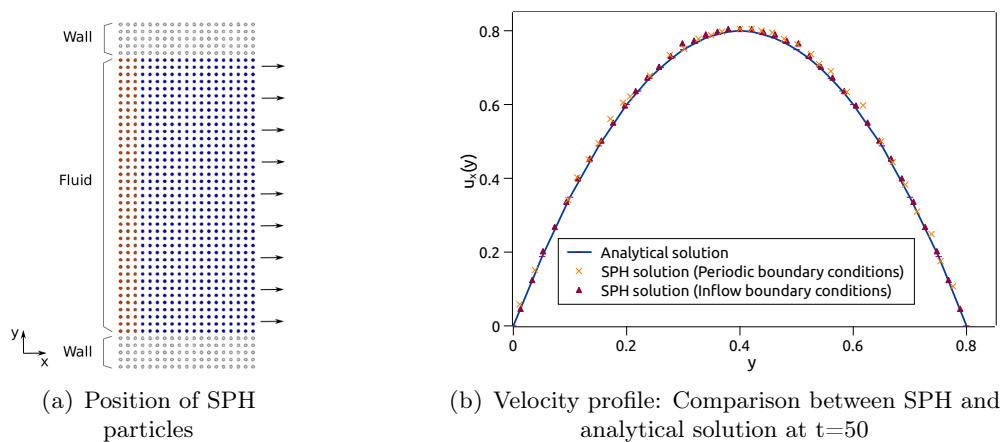


FIGURE III.21: Poiseuille flow simulation.

## III.5 Vibrations

### III.5.1 Method description

One possible way to control the fragmentation process is to apply external vertical vibrations on the rotating rod. This technique was used by Zainoun *et al.* [38, 138] to control the particle size distribution in the case of centrifugal atomization. For applying the vibrations, two configurations can be considered. First, the vibrations can be imposed on the fluid particles by adding an external sinusoidal acceleration as follows:

$$a(t) = A_0(2\pi F)^2 \sin(2\pi Ft) \quad (\text{III.25})$$

where  $A_0$  and  $F$  are the amplitude and frequency of the vibrations, respectively. The other set-up is to apply the vibrations on the solid below the liquid film by changing its position, according to:

$$z_w(t) = z_0 + A_0 \sin(2\pi Ft) \quad (\text{III.26})$$

This set-up is used for the specific case of the REP atomizer. In order to not disturb the

fluid inlet and avoid instabilities, the amplitude of the vibrations is progressively increased along the rod radius. This being so, the expression of  $A_0$  as a function of  $r$  is given by

$$A_0(r) = A_0 \exp\left(\frac{r}{R} - 1\right) \quad (\text{III.27})$$

where  $A_0$  stands for the maximum amplitude.

### III.5.2 Verification example

To ensure that, for the second configuration, the vibrations are well transmitted to the fluid particles, a simple test was conducted. Liquid particles were travelling horizontally on a vertically vibrating solid plate according to equation III.26, see figure III.22. The movement of the fluid particles along the  $z$  axis was compared to the movement of the solid particles. For a given  $x$  position on the solid plate, the average position of the liquid and wall particles along the  $z$  axis is plotted against time in figure III.23. The results show that the liquid is vibrating with the same frequency and amplitude as the solid plate, which means that the vibrations are well transmitted from the solid to the liquid particles.



FIGURE III.22: Simulation set-up; liquid travelling on a vibrating solid plate.

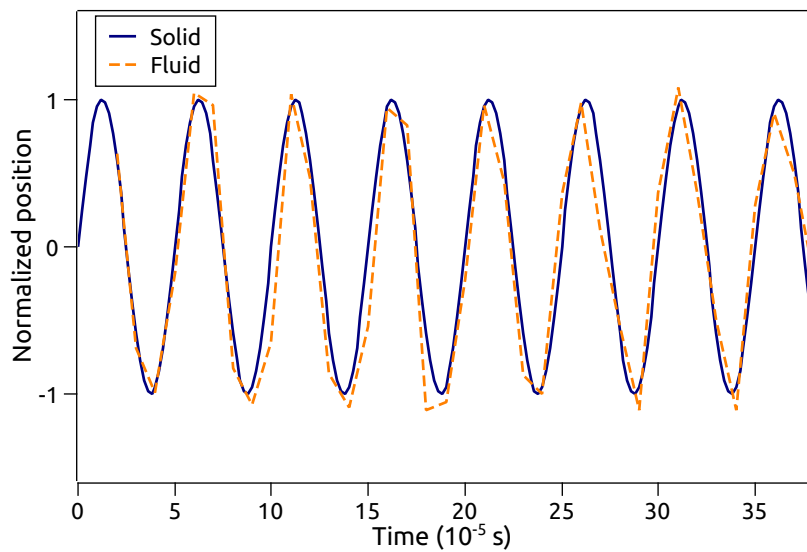


FIGURE III.23: Position of the solid and liquid particles as a function of time.

## III.6 Case study: Application to the break-up of unidirectional water jet

### III.6.1 Literature review

The behaviour of a vertical jet prior to rupture can be classified into mainly four regimes (see figure III.24) depending on the properties of the liquid jet and its outlet velocity: dripping, Rayleigh, wind-induced and atomization [139]. Basically, if the fluid has a high viscosity the break-up is delayed because the instabilities are damped by viscous forces. In the first two regimes, the capillary forces are dominant and the break-up process is axis-symmetrical which means that the droplet diameter can be directly related to the orifice diameter. In fact, the Rayleigh-Plateau instability is a surface tension phenomenon and thus, the effect of inertial and viscous forces can be ignored. Higher Reynolds numbers lead to an increase in the aerodynamic interaction with surrounding gas, which creates additional surface instabilities. The break-up in these regimes is more chaotic and the average droplet diameter is much more smaller than the orifice diameter.

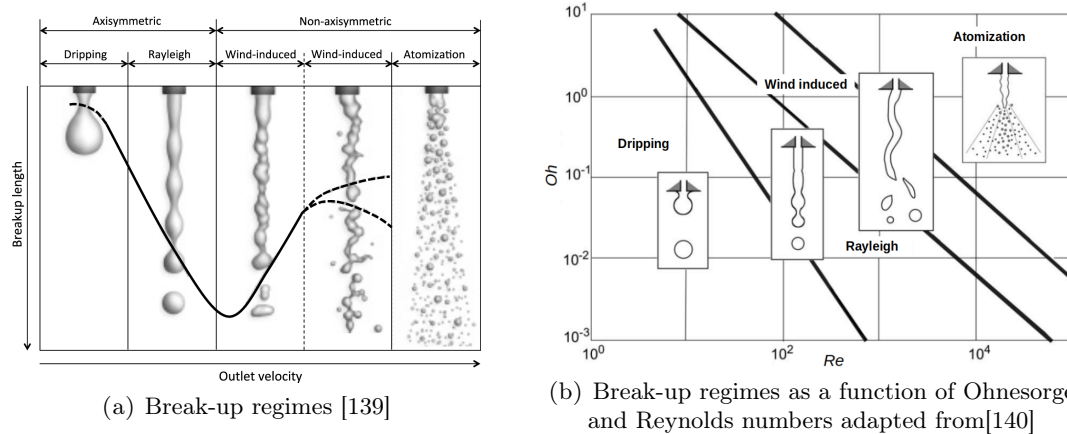


FIGURE III.24: Dependence of the break-up regimes on the fluid properties and the jet velocity.

Lord Raleigh was the first to propose a theoretical model for the capillary instability leading to the jet fragmentation in 1878 [18, 19]. Later, Weber [20] included the effect of viscosity on the jet break-up and reported a linear approximation for the Rayleigh model. The droplet formation mechanism is explained in chapter I section I.2.2.

### III.6.2 Experimental set-up

Many experimental studies of the jet breakup have been conducted, for example [37, 141–146]. These experiments have shown that the system behaves according to the Rayleigh Plateau instability analysis by studying the instability of a jet subjected to a harmonic disturbance. These external disturbances can be imposed by a magnetic, acoustic or mechanical force.

With the same aim, we have conducted an experimental campaign to study the effect of

external vibrations on the fragmentation of a unidirectional vertical liquid jet (water and Bolton 117). The experimental device is formed by two major parts: the body (cylinder + piston) and the atomization system. The latter consists of a Swagelock reducers and T connections. For droplet generation, a press applies a force to the piston and moves it with a controlled speed. Photos of the jet are taken by means of a fast camera. In order to trigger the fragmentation mechanism, vibrations were applied to the jet by using a piezoelectric cell, positioned in such a way that vibrations are applied in the direction of the jet flow. The scheme of the device is shown in Figure III.25. A series of experiments have been carried out with water and liquid metal for various orifice diameters, jet outlet velocities and position of the piezoelectric cell. For more details on the experimental results, refer to appendix A.

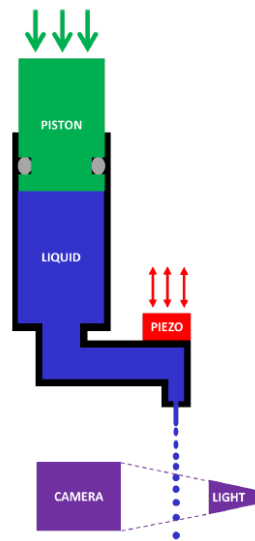


FIGURE III.25: Schematic representation of the atomization device.

The objective here is to evaluate the chosen numerical method and compare the simulation results to experimental and theoretical results (chapter I section I.2.2). For this purpose, the jet orifice diameter was taken equal to  $150 \mu\text{m}$  with an average jet velocity of  $5.5 \text{ m/s}$ . The average diameter for water droplets for different frequencies are listed in table III.8.

TABLE III.8: Variation of the droplet mean diameter as a function of the frequency.

| Frequency (kHz)             | 0 | 7   | 8   | 9   | 11  |
|-----------------------------|---|-----|-----|-----|-----|
| $D_{mean}(\mu\text{m})$     | - | 313 | 317 | 310 | 269 |
| Relative standard deviation | - | 12  | 8   | 6   | 8   |
| Photo of the jet            |   |     | ●   | ●   | ●   |
|                             |   |     | ●   | ●   | ●   |
|                             |   |     | ●   | ●   | ●   |

### III.6.3 SPH simulation set-up

Richards *et al.* [147] used the Volume Of Fluid (VOF) method to study the effect of the Reynolds number on the jet break-up length and droplet size. Pan *et al.* [148] used the Level Set Method (LSM) to simulate the breakup of laminar liquid jets into still air. Using the VOF method, Delteil *et al.* [149] simulated the growth rate dispersion relation predicted by Rayleigh theory. More recently, Yang *et al.* [150] also used the VOF method to study the effect of forced perturbation on jet breakup for low speed and high speed regimes. Lately, Shen *et al.* [151] simulated the transition between different break-up regimes and compared their numerical data with experimental photos. Saito *et al.* [152] used the Lattice Boltzmann Method (LBM) to study the jet breakup problem. Ménard *et al.* [153] combined LSM, VOF and Ghost Fluid Method (GFM) for the simulation of jet breakup in 3D. The above presented methods are mesh based methods that use specific interface tracking techniques and grid reconstruction process. Therefore, a high resolution grid is needed for capturing the interface accurately, which subsequently increases the calculation cost. On this basis, mesh-free numerical methods seem to be an interesting approach for simulating the jet breakup. Sirotkin *et al.* [75] used a corrected single phase SPH method to study viscous jet breakup and the transition from dripping to jetting by changing the Weber number. Takashima *et al.* [74] also used SPH for 3D simulation of water breakup. Pourabdian *et al.* [154] used SPHysics open source code to investigate the relation between the breakup length and the jet properties by changing Reynold and Weber numbers. Their results agreed well with experimental data. Farrokhpahanah *et al.* [155] used multi-phase SPH method to study the jet breakup phenomena and the transition between jetting and dripping regimes. More recently, Yang *et al.* [76] used a multi-phase SPH model based on Riemann solvers to investigate low-speed 2D jet break-up.

In this work, the SPH model detailed in chapter II is used to study the effect of the vibrations on the jet break-up and the particle size distribution with a comparison to the experimental data presented above and the theoretical model. The simulations have been performed for a water jet in the Rayleigh break-up regime. Water is issued from a cylindrical reservoir with an orifice diameter equal to 150  $\mu\text{m}$ . An initial velocity profile is imposed on liquid particles as follows:

$$u_z(r) = u_{max} \left( 1 - \frac{r^2}{R_{jet}^2} \right) \quad (\text{III.28})$$

where  $u_{max}$  and  $R_{jet}$  are the maximum output velocity and the orifice radius, respectively. The mean velocity is equal to  $u_{mean} = 0.5u_{max}$ . A constant flow rate is ensured by applying the continuous inlet flow method described in the previous section. The jet is falling vertically downwards under the force of gravity. It fragments into droplets along its trajectory downstream from the reservoir exit. The effect of imposing vibrations on the fragmentation process and the droplets size is studied by applying an external excitation to the fluid particles in the form of a sinusoidal acceleration in the jet direction (vertical direction) according to equation III.25. The simulation set-up is presented in figure III.26. The simulation parameters and the relevant dimensionless numbers are summarized in table III.9. According to the  $Re$  and  $Oh$  numbers, the break-up of the liquid jet follows the Rayleigh regime.

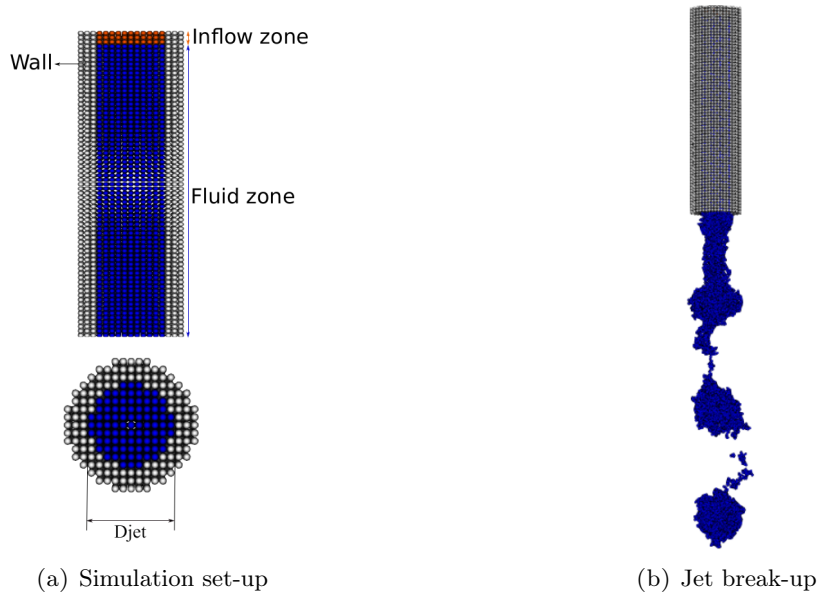


FIGURE III.26: Water jet break-up simulation.

TABLE III.9: Simulation parameters.

| Parameter                             | Value                    |
|---------------------------------------|--------------------------|
| Fluid                                 | Water                    |
| Jet diameter ( $D_{jet}$ )            | 150 $\mu\text{m}$        |
| Jet mean velocity ( $u_{mean}$ )      | 5.5 m/s                  |
| Density ( $\rho$ )                    | 1000 kg/m <sup>3</sup>   |
| Dynamic viscosity ( $\nu$ )           | 0.001 N.s/m <sup>2</sup> |
| Surface tension ( $\sigma$ )          | 0.072 N/m                |
| Gravitational acceleration ( $g$ )    | 9.81 m/s <sup>2</sup>    |
| Rayleigh frequency ( $F_{Rayleigh}$ ) | 8400 Hz                  |
| Reynolds number ( $Re$ )              | 825                      |
| Ohnesorge number ( $Oh$ )             | 0.0096                   |
| Weber number ( $We$ )                 | 63                       |

### III.6.4 Results

Figure III.27 represents snapshots of the jet break-up for different frequencies as a function of time. It can be seen that by applying external vibrations, the break-up process occurs in a more orderly manner and the main droplets have nearly the same size. Without any vibrations, the break-up process is not controlled. By increasing the frequency the number of satellite particles tends to slightly decrease. The break-up at the Rayleigh's frequency (table I.2) presents the most regular pattern results.

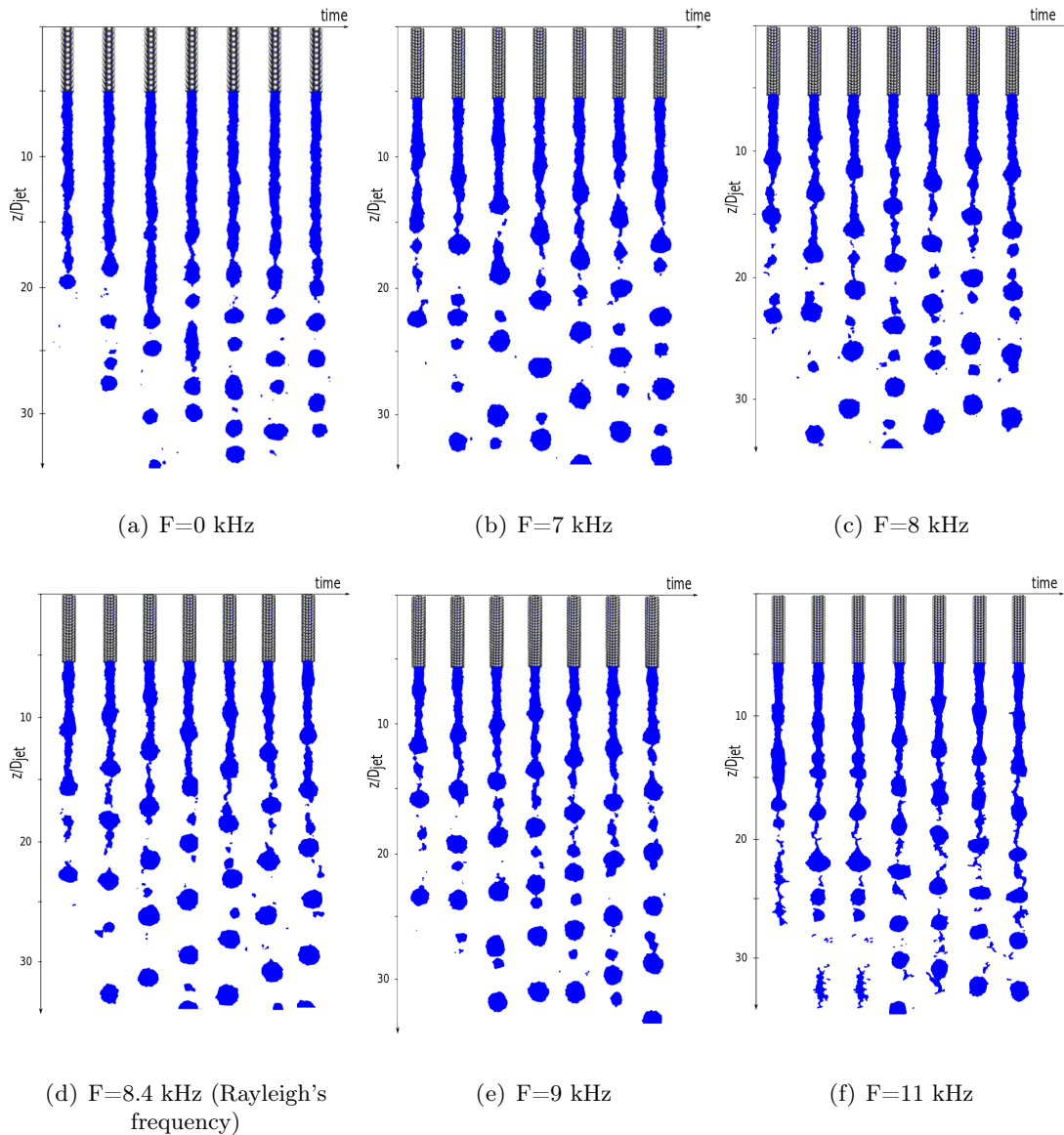


FIGURE III.27: Snapshots of the jet fragmentation for different frequencies and times ( $\Delta t = 0.2$  ms).

For a quantitative comparison, the average diameter of the main droplets obtained by the SPH simulations is compared to the theoretical and experimental data. The results are presented in table III.10 and figure III.28. The SPH results agree very well with the theoretical droplet diameter: for the range of frequencies studied here, the mean droplet diameter tends to decrease when the frequency increases. Furthermore, the size of the satellite droplets also tends to decrease with the increase of the frequency. By contrast, for the experimental data, no satellite droplets were observed in these frequency ranges. Yang *et al.* [150] also observed the formation of satellite droplets using the VOF method to simulate the jet break-up for the same frequency range. The SPH simulations show that some satellite droplets will merge with the main droplets on their trajectory as shown in figure III.29: the satellite droplet merged with the main droplet within approximately two wavelengths. This means that more satellite droplets could vanish during their trajectory.



However, in the SPH simulations the diameter of the droplets is measured at a distance equal to 1 cm from the nozzle orifice, that is to say at the outer limit of the computational domain, whereas in the experimental study, the camera was placed at a distance between 10 to 15 cm from the nozzle orifice. This might partially explain the difference observed between the experimental and SPH results regarding satellite droplets formation.

TABLE III.10: Theoretical, SPH and experimental mean droplet diameter as a function of the applied frequency.

|                                     |     |      |      |      |      |      |
|-------------------------------------|-----|------|------|------|------|------|
| F (kHz)                             | 0   | 7    | 8    | 8.4  | 9    | 11   |
| $F/F_{Rayleigh}$                    | 0   | 0.83 | 0.95 | 1    | 1.07 | 1.3  |
| $D_{Theoretical}(\mu m)$            | -   | 300  | 287  | 282  | 276  | 258  |
| $D_{SPH}(\mu m)$                    | 263 | 281  | 278  | 275  | 269  | 240  |
| $D_{Experimental}(\mu m)$           | -   | 313  | 317  | -    | 295  | 269  |
| Standard deviation ( $\mu m$ )(SPH) | 27  | 13   | 11.5 | 10.5 | 10   | 10.6 |
| Error $_{SPHvsTheoretical}$ (%)     | -   | 7    | 3.3  | 2.6  | 2.5  | 7    |

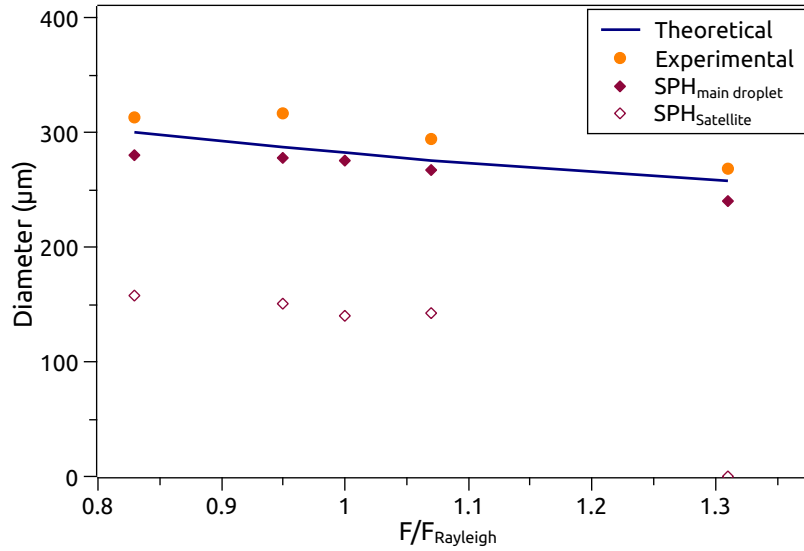


FIGURE III.28: Theoretical, SPH and experimental data for the variation of the mean and satellite droplet diameter as a function of the applied frequency.

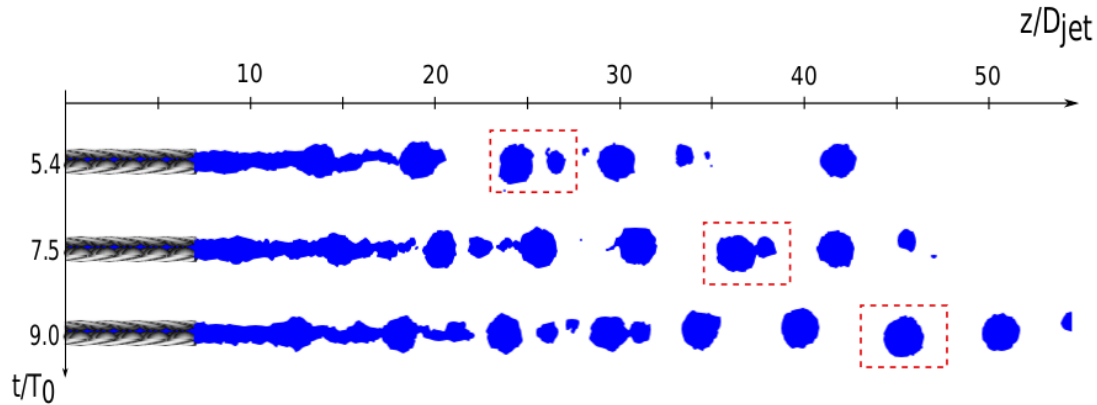


FIGURE III.29: Satellite and main droplet merging.

Figure III.30 shows the break-up time of the first droplet as a function of the perturbation frequency. Starting from low perturbation frequencies, the break-up time decreases and then tends to increase after reaching a minimum value for the optimum frequency predicted by Rayleigh's theory. In fact, the break-up time is directly influenced by the growth rate of the disturbance considering that the jet breaks when the disturbance amplitude is equal to the jet radius. The largest growth rate is obtained for frequencies around the Rayleigh frequency, therefore the break-up time is shortest for  $F/F_{Rayleigh} \simeq 1$ . For  $F \neq F_{Rayleigh}$ , the growth rate decreases resulting in an increase in the break-up time.

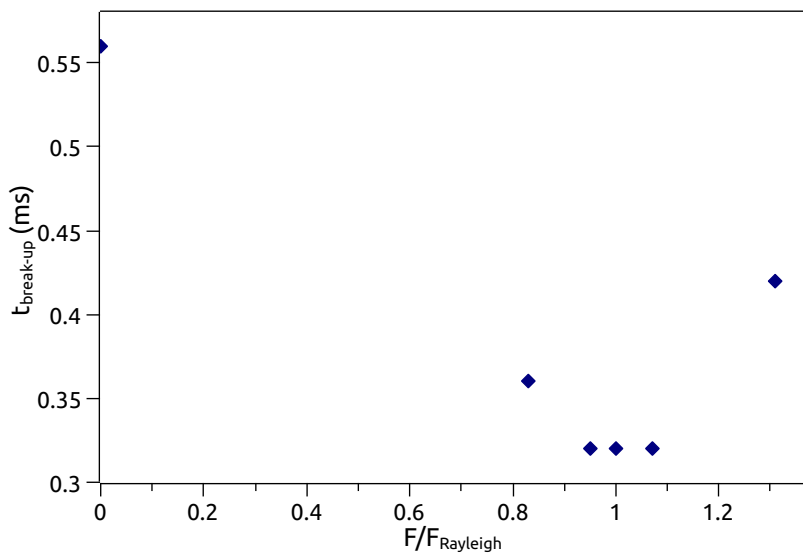


FIGURE III.30: Break-up time of the first droplet as a function of the frequency.

To better evaluate the effect of the vibrations on the particle size distribution, the curves for the cumulative mass are presented in figure III.31. For the SPH results, the effect of the satellite droplets can be seen by the slight increase of the curves for small diameters ( $140 \mu\text{m} < D < 160 \mu\text{m}$ ). These satellite droplets represent about 5 % of the total mass. When applying vibrations, the produced droplets have a sharper size distribution than for the case of the jet break-up without applying vibrations. The difference of about 10-15

% observed between the experimental and SPH mean diameter can be mainly explained by the fact that the experimental set-up was not completely controlled compared to the simulation set-up: there is uncertainty about the exact orifice diameter, the jet velocity and the calibration of the jet photos.

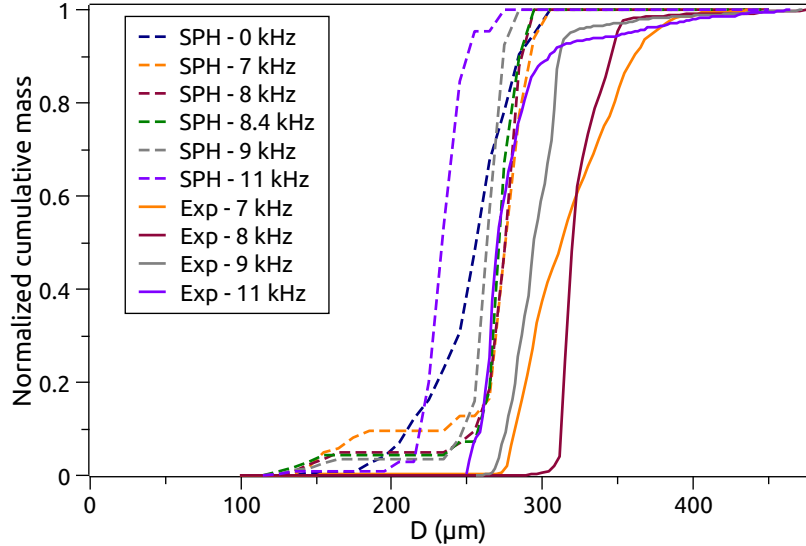


FIGURE III.31: Cumulative mass distribution as a function of the frequency.

It follows from the results presented above that the SPH model can simulate the break-up process of a liquid jet and reproduce the expected results when applying forced vibrations. The numerical results agree very well with the theoretical and experimental results.

### III.7 Conclusion

For the simulation of the REP, a proper surface tension model was implemented in the WCSPH code for free surface simulations and verified with two standard test cases: the square droplet and droplet oscillation. Moreover, to overcome the problem of the density calculation near the free surface, a new density calculation method based on the curvature and the distance of each particle from the surface was proposed here and successfully applied to the Rayleigh-Plateau breakup. In order to simulate an industrial process and optimize the computational cost, a continuous inlet boundary condition was implemented and tested with the Poiseuille flow test case. Finally, the overall SPH model was applied for the unidirectional jet break-up with vibrations. The SPH simulations gave satisfying results that agree well with the theoretical model. After validation of the SPH numerical model, the next step is to simulate the fragmentation process in the REP configuration.



# Chapter IV

## Simulation of the REP atomizer

### Contents

---

|  |     |
|--|-----|
| IV.1 Hypothesis . . . . .                              | 80  |
| IV.1.1 Model description . . . . .                     | 81  |
| IV.1.2 Results processing . . . . .                    | 82  |
| IV.2 Simulation parameters . . . . .                   | 84  |
| IV.2.1 Analytical calculation. . . . .                 | 84  |
| IV.2.1.1 Melting speed . . . . .                       | 84  |
| IV.2.1.2 Volume flow rate . . . . .                    | 85  |
| IV.2.1.3 Velocity profile. . . . .                     | 86  |
| IV.2.1.4 Film thickness . . . . .                      | 86  |
| IV.2.2 Simulations parameters choice . . . . .         | 87  |
| IV.3 REP simulation results and observations . . . . . | 89  |
| IV.3.1 Qualitative analysis . . . . .                  | 89  |
| IV.3.1.1 Contact angle . . . . .                       | 89  |
| IV.3.1.2 Atomization regime . . . . .                  | 90  |
| IV.3.2 Particle size distribution. . . . .             | 91  |
| IV.3.2.1 SPH simulations with 316L. . . . .            | 91  |
| IV.3.2.2 SPH simulations with UMo. . . . .             | 92  |
| IV.3.2.3 Droplet formation frequency . . . . .         | 101 |
| IV.3.3 Effect of external vibrations . . . . .         | 102 |
| IV.4 Conclusions . . . . .                             | 104 |

---

The main objective of this work is to simulate the REP industrial atomizer for UMo powder production. First of all, the geometry of the system to be modelled needs to be defined in order to optimize the computational cost. Secondly, the simulations input data are explained. Finally, the effect of the operational parameters on the fragmentation process and on the droplet size distribution is investigated. SPH simulations results are compared with semi-empirical models from literature and experimental data carried out in CERCA-Framatome facilities.

## IV.1 Hypothesis

Owing to the complexity of the physical processes, general assumptions/simplifications are made in order to reduce the computational cost, while capturing the droplet breakup phenomenon.

Experimentally, the thin liquid film on top of the rotating rod is formed due to the melting of the latter by a laser beam. Then, the molten metal is ejected centrifugally in the form of droplets that solidify in an inert atmosphere. These two phenomena do not occur at the same time scale. The time  $\tau_m$  required to melt the rod over a vertical distance equal to a film thickness of  $H \approx 5 \mu\text{m}$  can be estimated by a proportional rule. Knowing that it takes approximately 60 s to atomize a rod of height 2.5 cm, the time  $\tau_m$  is of the order of 10 ms. By contrast, the typical time  $\tau_f$  between two droplets ejection is estimated around 0.06 ms at 31000 rpm.  $\tau_f$  is much smaller than  $\tau_m$ , so it is reasonable to model only a stationary liquid flow and not consider the consumption of the rod. On account of this, the thermal and fluid mechanics aspects are decoupled, and only the atomization phenomenon is studied here. With this configuration, the representation of the total volume of the solid rod is no longer needed, thus the total number of particles considered is smaller which further reduces the computational cost.

This also means that for the SPH simulations, a homogenous liquid film is considered at the top of the rotating rod. However, it is not the case experimentally, where the heating of the consumable rotating rod is not fully controlled and thus the formation of the liquid film is not homogenous. This is mainly due to the fact that the diameter of the laser beam does not cover the entire top surface and the outer side surface of the rod is cooled faster due to convection and radiation, as explained in chapter I.

Moreover, the two main input parameters for the SPH model are the rotation speed and the film thickness. The first can be obtained directly from the experimental data. However, the film thickness is calculated from the mass flow rate. In our case, the experimental mass flow rate is calculated from experimental data, considering the mass of the rod before and after atomization and the total time for atomization. Thus, the exact mass flow rate in the steady state regime is unknown, but it is approximated as the total mass flow rate.

The implementation of an accurate contact angle model between the liquid melt and

---

the horizontal solid surface is currently not available in this version of the code. Only two configurations can be studied: perfect wetting and no-wetting. Based on experimental studies [156, 157], it was found that under controlled atmosphere with no oxidation, a liquid metal wets well a solid surface made from the same metal, with a contact angle  $\theta \ll 90^\circ$ . Therefore, a complete wetting approach ( $\theta = 0^\circ$ ) was adopted for this study.

The Coriolis effect is not considered in this study. This force is in competition with inertial and viscous forces. The Ekman number ( $Ek = \frac{1}{\omega} \frac{\rho h^2}{\mu}$ ) defined as the ratio between viscous forces and centrifugal forces is used to characterize liquid flows in centrifugal atomization. A large  $Ek$  number implies a small Coriolis force against viscous force. The Rossby number ( $Ro = \frac{1}{\omega} \frac{R}{u}$ ) defines the ratio between inertial force and centrifugal or Coriolis force. In general,  $Ro < 1$  indicates a dominance of Coriolis force over inertial force and the contrary for  $Ro > 1$ . For this specific application,  $Ek$  is in the range of 6-15 (Coriolis force  $\ll$  Viscous force) and  $Ro$  varies between 0.04-0.1 (Coriolis force  $\gg$  Inertial force) at the edge of the rotating rod. Given these values, we can conclude that: Inertial force  $\ll$  Coriolis force  $\ll$  Viscous force. Of these three, the viscous force is the most important and the other two are negligible. Additionally, according to Mohammadi [158], the Coriolis force can be neglected providing that  $Re_E^2/Re_T$  is less than unit. For the REP atomizer,  $Re_E^2/Re_T$  is in the range of 0.002 – 0.08 at the edge of the disk. This number tends to be even smaller towards the center of the disk. This justifies the assumption to neglect the Coriolis effect. Besides, Myers et al. [159, 160] showed that for axisymmetric flow and within the limits of the lubrication theory ( $(\frac{H}{L})^2 Re \ll 1$ ) the height of the thin liquid film at the edge of the disk is not affected by the Coriolis force.

The gas in the atomization chamber is not modelled to spare computational time. This means that the interaction between the liquid film and the surrounding gas is also not taken into account in the current model.

The statistical study on the particle size distribution was carried out on a limited number of droplets, ranging from 30 to 100 droplets approximately. This seems to be a fairly acceptable number because the simulations start from a steady state regime and no change was observed in the fragmentation process during the simulations.

#### IV.1.1 Model description

The system is reduced as shown in figure IV.1. Because the system is axisymmetric, the domain can be reduced to an angular sector with periodic boundary conditions. Second, the breakup process occurs at the edge of the rotating rod, so it seems reasonable to model the liquid flow only at the periphery of this angular sector. Finally, for simplification reasons, the edge of the angular sector is approximated to a parallelepiped. Thus, the angular coordinates ( $r$ ,  $\theta$  and  $z$ ) are replaced by Cartesian coordinates ( $x$ ,  $y$ , and  $z$ ).

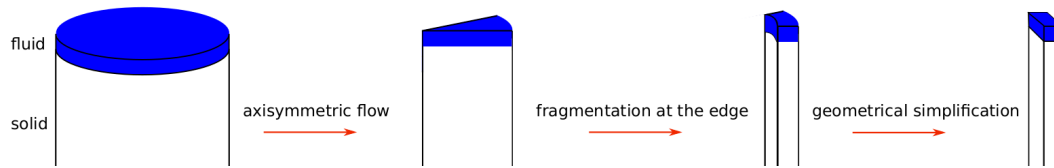


FIGURE IV.1: Reduced geometry.

Periodic boundary conditions are imposed in the tangential direction, as shown in figure IV.2. Liquid metal is assumed to flow continuously on the surface of the rotating rod with a constant flow rate. At the inlet in the transversal direction along  $x$ , a well defined velocity profile and pressure are imposed on SPH particles. At the boundary between the solid and fluid particles, a no-slip condition is imposed on the velocity profile, as explained in [90].

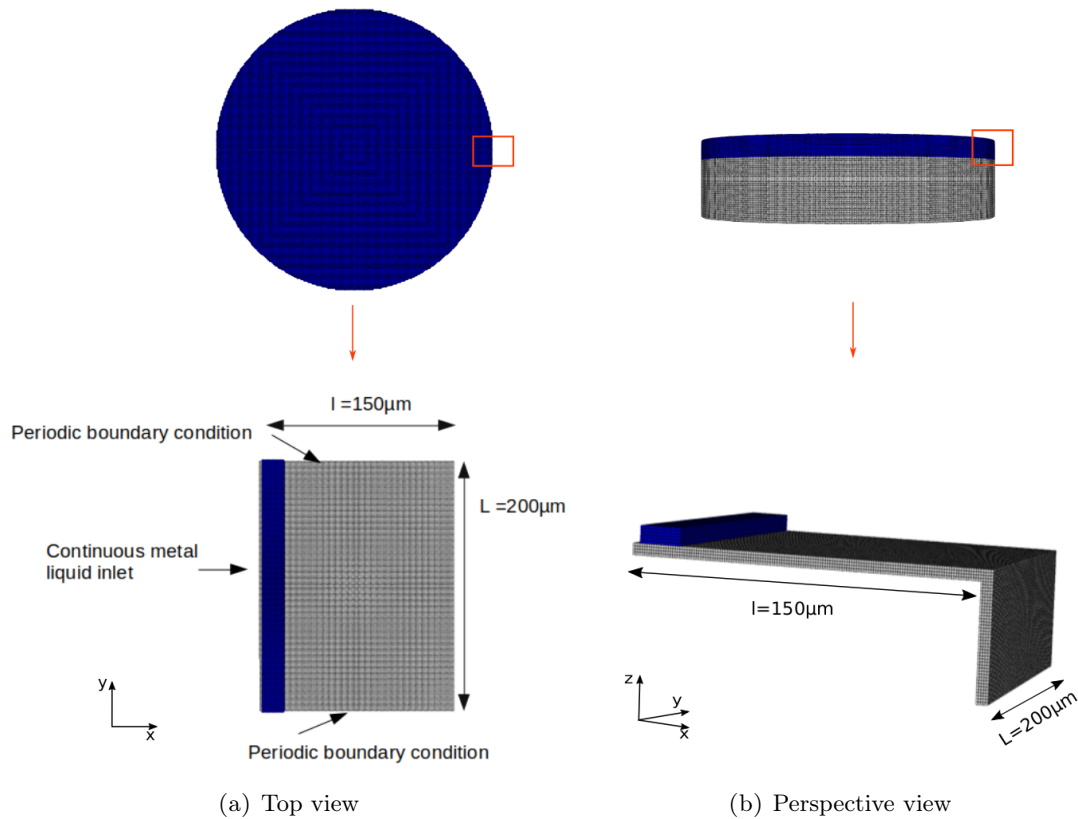


FIGURE IV.2: Reduced geometry with relevant boundary conditions for the REP simulation.

### IV.1.2 Results processing

According to the fuel specifications at CERCA-Framatome, the UMo fuel powder has to meet a list of constraints regarding composition, morphology, particle size, porosity, etc. The target droplet diameter is in the range of 40 to 125  $\mu\text{m}$ . From an industrial point of view and to study the efficiency of the REP atomizer, it is important to define the particle size distribution as a function of the mass or volume of the produced powders.



The normalized mass distribution  $\varphi_m$  is obtained by:

$$\varphi_m = \frac{\text{Mass of particles between } (D - \Delta D/2) \text{ and } (D + \Delta D/2)}{\text{Total mass of all particles}} \quad (\text{IV.1})$$

where  $\varphi_m$  describes the mass fraction of particles whose diameter is within an interval of  $D - \Delta D/2$  and  $D + \Delta D/2$  with  $\Delta D$  being the size of this interval (for this study  $\Delta D = 5 \mu\text{m}$ ). Because the particle mass is proportional to  $D^3$ , this representation overestimates coarse particles at the expense of fine particles. Thus, it is interesting to normalize the mass distribution by the corresponding size class [15] or to present the results as a function of the normalized number of particles  $\varphi_N$ .

$$\varphi_N = \frac{\text{Number of particles between } (D - \Delta D/2) \text{ and } (D + \Delta D/2)}{\text{Total number of particles}} \quad (\text{IV.2})$$

Another frequently used representation for the particle size analysis is the cumulative undersize distribution that expresses the mass/number percentage of a specific particle size or below, as shown in figure IV.3. In this work, the notation  $D_{m,x}$  indicates the diameter at which x percent of the particle mass has a smaller diameter than  $D$ . Another important characteristic diameter, the one expressed the most by the semi-empirical models, is  $D_{32}$  which refers to the Sauter diameter.  $D_{32}$  is used to describe particles having the same volume/area ratio as the entire powder, it is defined by:  $D_{32} = \frac{\sum_i D_i^3}{\sum_i D_i^2}$ .

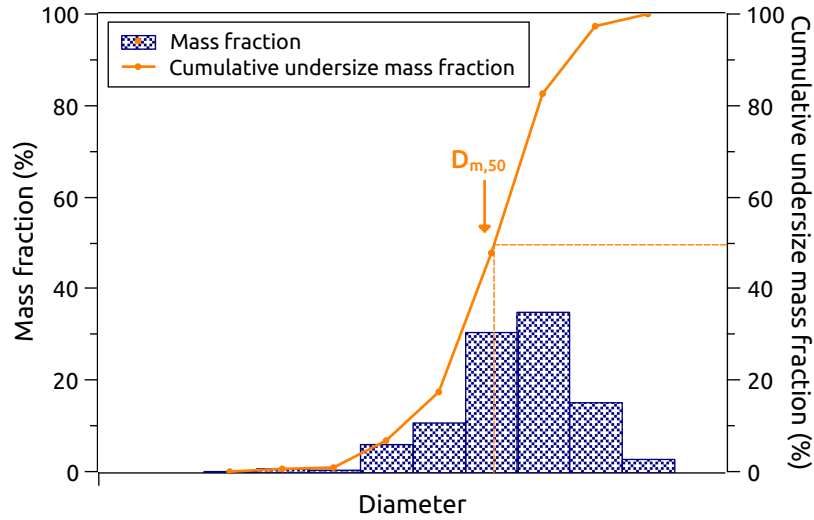


FIGURE IV.3: Example of a particle size distribution.

In what follows, the diameter of the droplets is measured using the "Ruler" kit in Paraview. For each droplet three measurements are taken in three directions (x, y and z) and the final diameter is estimated according to:

$$D_{droplet} = (D_x \times D_y \times D_z)^{1/3} \quad (\text{IV.3})$$

## IV.2 Simulation parameters

### IV.2.1 Analytical calculation

The main objective of this calculation is to estimate the liquid vertical velocity profile and its thickness along the rod radius. These data will be used as input data for the SPH numerical model of the REP atomizer.

#### IV.2.1.1 Melting speed

Here, the melting speed refers to the velocity at which the rod is consumed due to its fusion by the laser beam. The enthalpy difference  $q$  ( $J/m^3$ ) required for the fusion of  $1 m^3$  of UMo is equal to:

$$q = \rho[H_{Latent} + C_p * (T_m - T_0)] \quad (IV.4)$$

where  $H_{Latent}$  is the latent heat of fusion ( $J/kg$ ),  $C_p$  is the mass specific heat capacity ( $J/kg.K$ ) and  $T$  is the temperature ( $K$ ). The subscript  $m$  refers to the melt. This heat  $q$  is provided to the rotating rod by the laser power. Two illumination configurations are studied here: Linear and Gaussian profiles.

**Linear profile** In this case, the laser flux density  $\phi$  ( $W/m^2$ ) is constant along the rod radius and thus the total laser power  $P$  ( $W$ ) delivered to the rotating rod is calculated by:

$$P = \int_0^R \epsilon\phi 2\pi r dr = \epsilon\phi\pi R^2 \quad (IV.5)$$

where  $\epsilon$  is the absorption coefficient, the ratio between the delivered laser power and the one absorbed by the material. From equations IV.4 and IV.5 and by considering steady state with power equilibrium, the melting velocity can be calculated according to:

$$u_m(r) = \frac{P}{q\pi R^2} \quad (IV.6)$$

**Gaussian profile** In this case, the laser flux density can be expressed as follows:

$$\phi = \phi_0 \exp\left(\frac{-r^2}{2\mu^2}\right) \quad (IV.7)$$

where  $\mu$  is the standard deviation of the Gaussian distribution. Similarly to IV.5, the total power is equal to:

$$P = \int_0^R \epsilon\phi 2\pi r dr = 2\pi\epsilon\phi_0\mu^2 \left(1 - \exp\left(\frac{-R^2}{2\mu^2}\right)\right) \quad (IV.8)$$

Thus, the melting velocity in this case is obtained by:

$$u_m(r) = \frac{P}{q\pi R^2} \frac{\frac{R^2}{2\mu^2}}{1 - \exp\left(\frac{-R^2}{2\mu^2}\right)} \exp\left(\frac{-r^2}{2\mu^2}\right) \quad (\text{IV.9})$$

This profile contributes actively to the formation of a crater or a depression at the rod top surface.

#### IV.2.1.2 Volume flow rate

By carrying out a mass balance on a ring of radius  $r$ , width  $dr$  and height  $H$ , the volume flow rate  $Q$  ( $m^3/s$ ) in the axial direction  $z$  (figure IV.4), obtained by the fusion of the rotating rod, can be calculated based on the melting velocity:  $dQ_a(r) = (2\pi r dr)u_m(r)$ . The volume flow rate in the radial direction as a function of  $r$  can be calculated by applying the conservation law:  $Q(r+dr) = Q(r) + dQ_a(r)$  with  $Q(r) = (2\pi r h)\bar{u}(r)$ , where  $u_m$  is the velocity of the solid liquid interface that moves downwards and  $\bar{u}$  is the average velocity of the liquid film that moves horizontally, towards the periphery.

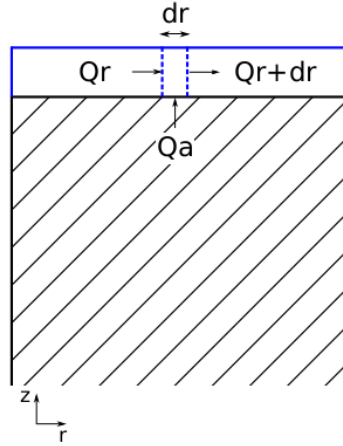


FIGURE IV.4: Flow rate representation.

By solving the above equations and by considering that at  $r = R$  the total flow rate  $Q(R)$  is known from experimental data ( $Q(R)$  is in the range of  $1-2e-7 m^3/s$ ), we obtain the following:

##### Linear profile

$$H\bar{u}(r) = \frac{1}{2}u_m(r)r + \frac{1}{r} \left( \frac{Q(R)}{2\pi} - \frac{1}{2}u_m(R)R^2 \right) \quad (\text{IV.10})$$

##### Gaussian profile

$$H\bar{u}(r) = -u_m(r)\frac{\mu^2}{r} + \frac{1}{r} \left( \frac{Q(R)}{2\pi} + u_m(R)\mu^2 \right) \quad (\text{IV.11})$$

**IV.2.1.3 Velocity profile**

Based on experimental data,  $Re_E$  is found to be in the range of 50 – 300, indicating that the flow is in the laminar regime [161]. Since it is a flow over a flat plate, the pressure gradient term in the flow direction can be neglected. By considering that the velocity derivatives across the film are large compared to those along the film, the Navier-Stokes equation, is simplified to:

$$\nu \frac{\partial^2 u(r)}{\partial z^2} + r\omega^2 = 0 \quad (\text{IV.12})$$

Equation IV.12 can be solved considering the following boundary conditions:

- at  $z = 0$  complete adherence  $\Rightarrow u(r) = 0$
- at  $z = H$  no shearing force  $\Rightarrow \frac{\partial u(r)}{\partial z} = 0$

The velocity profile in the radial direction as a function of  $z$  and the film thickness  $h(r)$  is then obtain by:

$$u(r) = \frac{\rho\omega^2 r}{\nu} \left( H(r)z - \frac{z^2}{2} \right) \quad (\text{IV.13})$$

**IV.2.1.4 Film thickness**

The film thickness is obtained using the relationship  $Q(r) = 2\pi r H(r) \bar{u}(r)$ .

**Linear profile**

$$H(r) = \left[ \frac{3\nu}{\rho\omega^2} \left( \frac{1}{2}u_m(r) + \frac{1}{r^2} \left( \frac{Q(R)}{2\pi} - \frac{1}{2}u_m(R)R^2 \right) \right) \right]^{\frac{1}{3}} \quad (\text{IV.14})$$

**Gaussian profile**

$$H(r) = \left[ \frac{3\nu}{\rho\omega^2 r^2} \left( -u_m(r)\mu^2 + \frac{Q(R)}{2\pi} + u_m(R)\mu^2 \right) \right]^{\frac{1}{3}} \quad (\text{IV.15})$$

Figure IV.5 shows an example of the film thickness as a function of the radius for an UMo rod of 1 cm radius rotating at 35000 rpm with a total mass flow rate of around 3 g/s. For linear and Gaussian profiles, the film thickness is almost constant at the rod edge and is equal to a few  $\mu\text{m}$ .

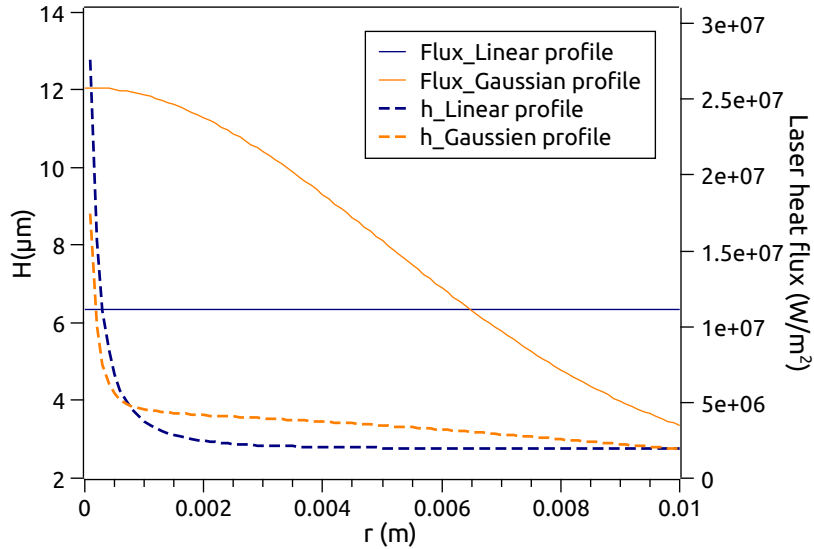


FIGURE IV.5: Example of the film thickness along the rod ( $\omega = 35000$  rpm and  $Q = 3$  g/s).

### IV.2.2 Simulations parameters choice

The main objective of this study is to verify that the SPH model is able to reproduce the results found in the literature and help manufacturers in defining suitable operational parameters for their powder atomization. We can then divide this objective into the following targets:

- Verify if the SPH model is capable of accounting for the different atomisation regimes (mainly DDF and LD) predicted by the theory (figure I.4).
- Verify if the SPH model is able to predict the Sauter diameter of the droplets calculated by the semi-empirical correlations (equation I.9).
- Compare SPH results with experimental results on the 316L stainless steel fragmentation.
- Identify the relevant operational parameters for the UMo atomization.
- Study the influence of applying vertical vibrations on the atomization process.

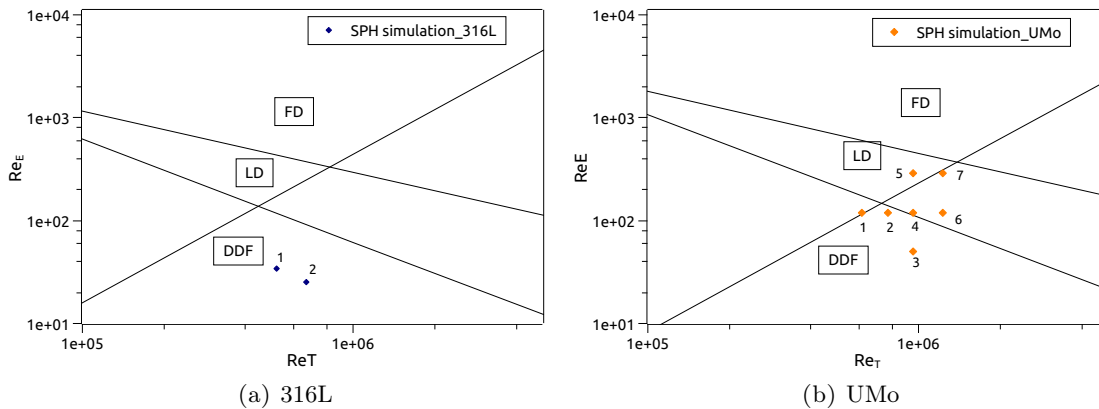
Previous theoretical and experimental studies [9, 15, 25] have shown that the fragmentation process and the PSD depend on the material properties ( $\rho$ ,  $\sigma$ ,  $\nu$ ) and operational conditions ( $Q$ ,  $D_{rod}$ ,  $\omega$ ). The material properties used in these studies are listed in table I.5. For the operational parameters, the rod diameter and rotation speed were defined by the design of the REP atomizer as part of the work of B. Ravry during his doctoral thesis [16]. The rod diameter is equal to  $D_{rod} = 0.02$  m and the rotation speed  $\omega$  ranges between 20000 – 40000 rpm. In the framework of his experimental thesis, experiments were conducted with 316L stainless steel. In this case, the mass flow rate  $Q$  observed experimentally is roughly equal to 1 g/s. For UMo simulations, the mass flow rate was chosen so as to compare different atomization regimes and to be able to map a region in the  $(Re_E, Re_T)$  space that interests the industrial partner. Thus, the mass flow rate  $Q$  is chosen between

3 – 20 g/s. These properties can be grouped into three non-dimensional numbers (table I.1):  $Re_E$ ,  $Re_T$  and  $Oh$ . Thereafter, the results will be presented as a function of these three numbers.

The  $Oh$  number is varied by changing the melting material. Two metals were considered in this study: Steel (316L) and UMo (table I.5). The main objective of using 316L is to compare the numerical results with the experimental data. The  $Re_T$  and  $Re_E$  are varied by changing the rotation speed and the mass flow rate, respectively. Experimentally, the mass flow rate is changed by changing the intensity of the heating laser. Table IV.1 represents the different simulations conducted for both steel and UMo. According to the experimental data with steel, the fragmentation occurs in the DDF regime as shown in figure IV.6a. In order to get closer to the experimental configuration, the fragmentation using UMo is conducted mainly in the DDF regime, with some simulations in the LD regime as represented in figure IV.6b for the purpose of studying the difference between these two regimes. The fragmentation in the LD regime is not relevant for UMo powder production because it was found experimentally that the particle size distribution of the final powder is broader.

TABLE IV.1: List of SPH simulations for 316L and UMo.

| Material | #      | $\omega$ (krpm) | $Q$ (g/s) | H ( $\mu\text{m}$ ) | $Oh$ ( $10^{-4}$ ) | $Re_T$ ( $10^5$ ) | $Re_E$ | Regime |
|----------|--------|-----------------|-----------|---------------------|--------------------|-------------------|--------|--------|
| 316L     | 316L-1 | 31              | 1.7       | 4                   | 4.6                | 5.2               | 34     | DDF    |
|          | 316L-2 | 40              | 1.3       | 3                   | 4.6                | 6.7               | 25     | DDF    |
| UMo      | UMo-1  | 20              | 7.2       | 5.5                 | 3.6                | 6.1               | 120    | DDF    |
|          | UMo-2  | 25              | 7.2       | 4.6                 | 3.6                | 7.7               | 120    | DDF    |
|          | UMo-3  | 31              | 3         | 3                   | 3.6                | 9.5               | 50     | DDF    |
|          | UMo-4  | 31              | 7.2       | 4                   | 3.6                | 9.5               | 120    | DDF    |
|          | UMo-5  | 31              | 17.4      | 5.5                 | 3.6                | 9.5               | 290    | LD     |
|          | UMo-6  | 40              | 7.2       | 3.3                 | 3.6                | 12.3              | 120    | DDF    |
|          | UMo-7  | 40              | 17.4      | 4.5                 | 3.6                | 12.3              | 290    | LD     |

FIGURE IV.6: SPH simulations in the  $(Re_T, Re_E)$  representation.

---

## IV.3 REP simulation results and observations

In this section, we compare SPH simulations to experimental observations and semi-empirical models for the Sauter Diameter. Further, the results on the effect of the vibrations on the atomization process are also presented.

### IV.3.1 Qualitative analysis

#### IV.3.1.1 Contact angle

As mentioned in the previous section, a complete wetting is considered between the liquid melt and the solid rotating rod. In the current SPH model, a complete wetting configuration can be achieved by taking into account the presence of the solid underneath the fluid in detecting surface particles. In this case, the surface tension force will not be applied on fluid particles in contact with the solid rod. The opposite situation is considered for zero wetting, the surface tension force will be applied on fluid particles as if the solid particles did not exist. To test these two configurations, the following test case was considered: an initially spherical liquid UMo droplet is deposited on a horizontal solid plane. Figure IV.7 presents the positions of the fluid particles at equilibrium for the two configurations. In the case of a complete wetting, the fluid particles spread out on the solid plane, which corresponds to a contact angle of  $0^\circ$ . For the zero wetting case, the particles form a droplet similar to the initial configuration but with a deformation due to gravity.

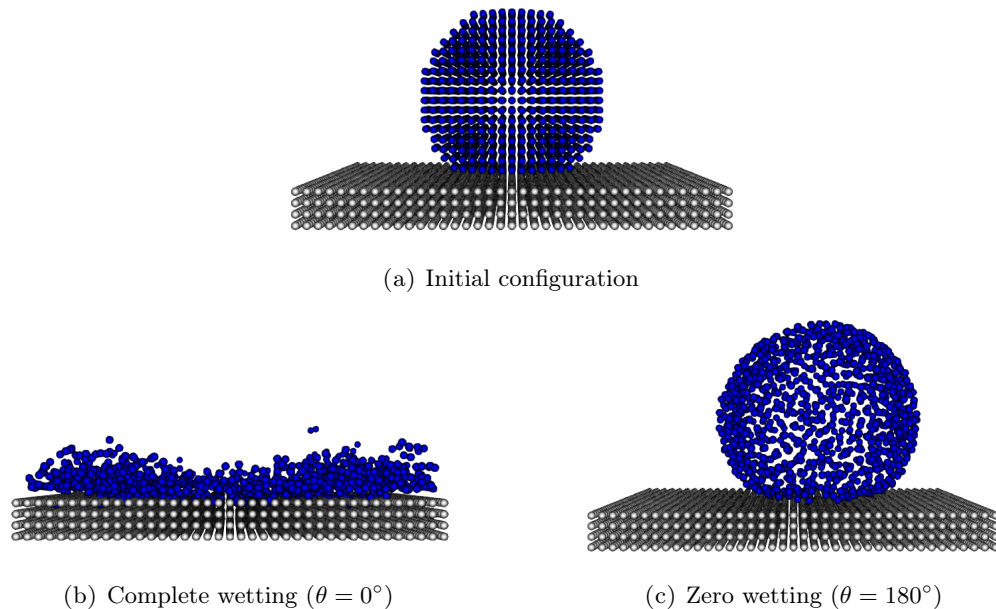


FIGURE IV.7: Wetting configurations.

In a static case (droplet at rest for example), the imposed angle between the fluid and the solid rod must be maintained. However, when the fluid is in motion, Cox-Voinov [162, 163] derived an empirical correlation between the dynamic contact angle and the capillary number taking into account the translational velocity of the contact line, see equation

IV.16. According to the correlation, the dynamic contact angle increases if the velocity of the contact line increases:

$$\theta_d^3 = \theta_s^3 + 9Ca * \ln\left(\frac{L_c}{l}\right) \quad (\text{IV.16})$$

where  $\theta_d$  and  $\theta_s$  are the dynamic and static contact angles, respectively. For complete wetting  $\theta_s = 0^\circ$ .  $l$  represents the microscopic length scale which is defined also by the slip length. In this case, it is considered equal to  $l = 5e-7 \text{ m}$ .  $L_c$  represents the macroscopic capillary length scale expressed by  $L_c = \sqrt{\frac{\sigma}{\rho a}}$ .  $Ca$  is the capillary number (table I.1).

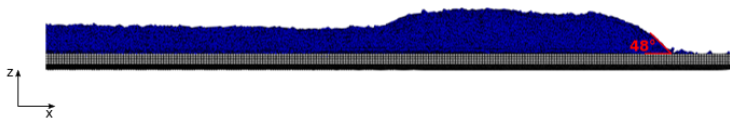


FIGURE IV.8: Example of contact angle measurement for the # UMo-5 simulation.

For most of the UMo simulations in the DDF regime, the film is not homogeneous near the edge. There is no formation of a homogenous film but rather the particles tend to clump forming droplets scattered over the rod surface. This behaviour makes it very difficult to measure the contact angle between the fluid and the solid support. For this reason, the contact angle is only measured when a homogeneous film is formed on the rod surface before reaching the edge. The angle formed by the liquid film and the solid rod is measured as shown in figure IV.8. The comparison between the calculated contact angles and the ones obtained by the SPH simulations are listed in table IV.2. Given the error due to the angle measurements, the results are acceptable since they are of the same order of magnitude as the angles predicted by equation IV.16.

TABLE IV.2: Comparison between analytical and SPH dynamic contact angles.

| #      | $L_c(\mu\text{m})$ | $Ca (\times 1000)$ | $\theta_{Cox-Voinov}^\circ$ | $\theta_{SPH}^\circ$ |
|--------|--------------------|--------------------|-----------------------------|----------------------|
| 316L-1 | 43.5               | 3.3                | 29                          | 35                   |
| 316L-2 | 33.7               | 3.1                | 28                          | 30                   |
| UMo-5  | 29.4               | 12                 | 43                          | 48                   |
| UMo-7  | 22.7               | 13                 | 44                          | 45                   |

### IV.3.1.2 Atomization regime

For the UMo simulations, two atomization regimes were analysed: Direct Droplet Formation (DDF) and Ligament Disintegration (LD). The difference in the fragmentation process between these two regimes can be seen in figure IV.9. For the DDF regime (figures IV.9a and IV.9b) the droplets are directly detached from the rod edge, whereas, for the LD regime (figures IV.9c and IV.9d), a ligament or a stripe is formed at the edge of the disk. These ligaments are then disintegrated into droplets at their ends, indicating a LD regime or a transition from DDF to LD. We can conclude that there is an agreement between the qualitative observations of the fragmentation modes obtained by SPH and the  $(Re_T, Re_E)$



---

representation [27] based on experimental results (presented in table IV.1 and figure IV.6b).

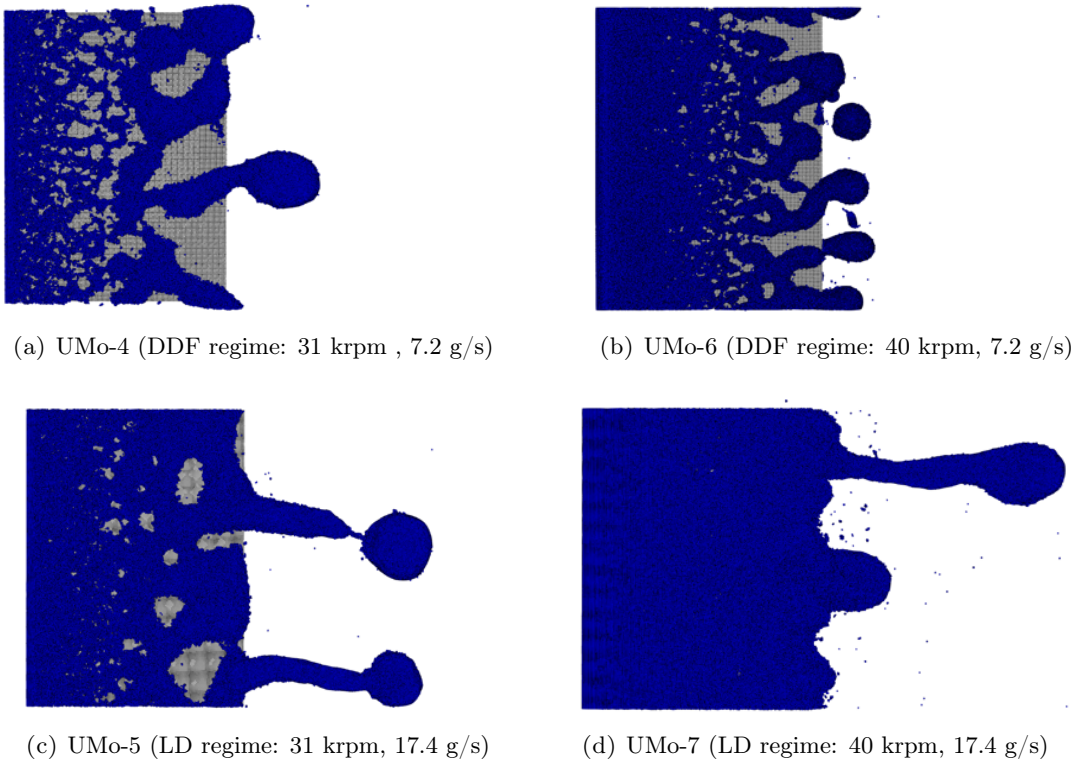


FIGURE IV.9: SPH simulation for UMo atomization: Evidence of DDF regime (a and b) and LD regime (c and d) (top view).

### IV.3.2 Particle size distribution

#### IV.3.2.1 SPH simulations with 316L

The aim of the simulations conducted with 316L stainless steel is to compare the SPH data with experimental data obtained in the framework of B. Ravry thesis [16]. However, taking into account the high computational cost and the time constraint, only a few droplets (less than 10 droplets) were obtained for 316L atomization. This means that the PSD could not be obtained. Hence, the study will be limited to the comparison of mean values of numerical and experimental data. A more complete study will be conducted for UMo atomization in the next section.

The main difference between 316L and UMo atomization is the centrifugal force. In fact, the break-up occurs when the centrifugal force overcomes the viscous and surface tension forces. Since the two alloys have similar properties, except for the density which is almost twice as high in the case of UMo, the centrifugal force for the latter is twice as important, which facilitates its atomization. Numerically, the atomization of UMo gives more droplets for a shorter calculation time, which has made it possible to obtain more particles and more robust statistical analysis.

For the simulations with steel, the diameter  $D_{m,50}$  is compared with experimental data (table IV.3). The SPH diameters are of the same order of magnitude ( $\pm 20\%$ ) as the experimental ones and they both follow the same tendency. However, the SPH simulations tend to under-estimate the droplet diameter compared with experimental values. This point will be discussed in more detail in the next section, where the UMo results are presented and compared with semi-empirical models. It was also observed, from the small data collected with SPH simulations, that for almost every main droplet, a smaller droplet was formed (figure IV.10). The diameters ratio between the main and satellite droplets is  $\frac{D_{satellite}}{D_{main}} = 0.17 \sim 0.18$ . Some experimental results, from B. Ravry thesis, show a bimodal distribution in the number-PSDs, for these cases the diameter ratio varies between  $0.17 - 0.25$ [16].

TABLE IV.3:  $D_{50}$  for experiments and SPH simulations with 316L.

| #      | $D_{Experimental}(\mu\text{m})$ | $D_{SPH}(\mu\text{m})$ | Standard deviation ( $\mu\text{m}$ ) | Error (%) | Nb of particles |
|--------|---------------------------------|------------------------|--------------------------------------|-----------|-----------------|
| 316L-1 | 90                              | 75                     | 30                                   | 17        | 10              |
| 316L-2 | 70                              | 55                     | 22                                   | 21        | 7               |

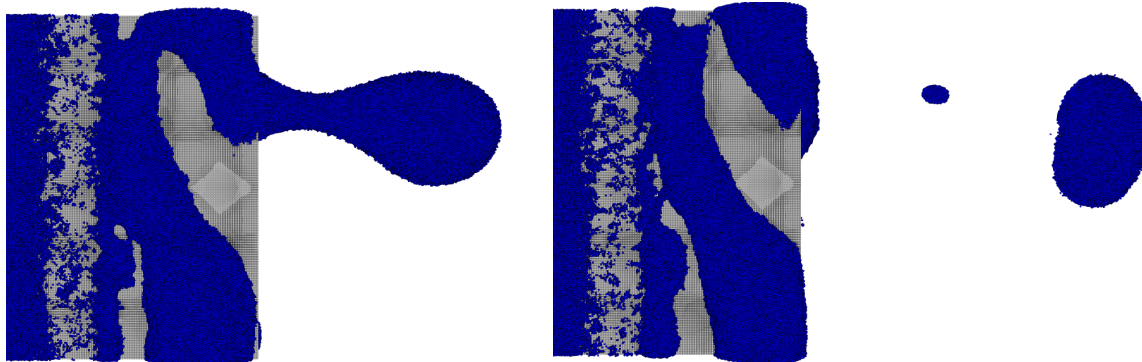


FIGURE IV.10: Steel atomization (316L-1) showing a bimodal PSD.

### IV.3.2.2 SPH simulations with UMo

Even for UMo simulations, the total number of droplets is limited due to the high computational cost. This number varies between 50 and 100 droplets. Be that as it may, the PSD and the mean diameter of the obtained droplets were compared for different operational parameters and the results are presented in the next section. To get an idea of the calculation time, table IV.4 presents the wall-clock time required to obtain the first 10 droplets for each simulation. The initial number of fluid particles refers only to the first few layers of particles as shown in figure IV.2. The average number of particles in these simulations is around  $10^6$  fluid particles. There is a significant difference in the wall-clock time between UMo-1 and UMo-5 simulations even though both have the same number of cores, time step and initial number of particles. This difference can be explained by the fact that in the case of UMo-5 simulation the size of the droplets is smaller compared to those for UMo-1 simulation. This means, that for UMo-5 simulation, several droplets can be obtained simultaneously on the periphery of the disk for the same geometry.

---

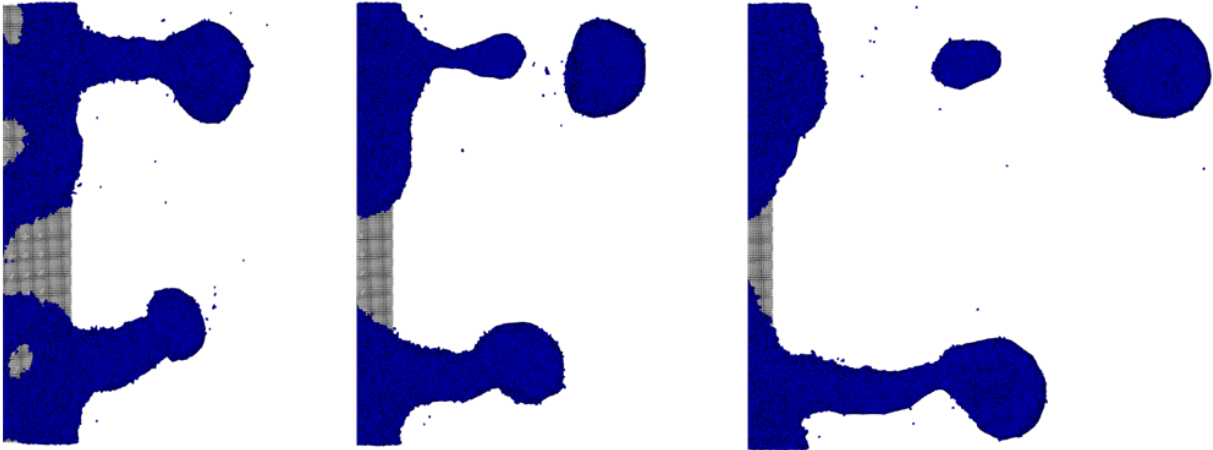
TABLE IV.4: Wall-clock time for obtaining the first 10 droplets.

| #     | Nb of particles /<br>thickness | Nb of cores | Time step<br>( $10^{-8}s$ ) | Initial nb of<br>fluid prtcls | Wall-clock<br>time (days) |
|-------|--------------------------------|-------------|-----------------------------|-------------------------------|---------------------------|
| UMo-1 | 5                              | 24          | 1                           | 20400                         | 12                        |
| UMo-2 | 4                              | 20          | 1                           | 13600                         | 8                         |
| UMo-3 | 3                              | 24          | 1                           | 10200                         | 6                         |
| UMo-4 | 4                              | 24          | 1                           | 13600                         | 4.5                       |
| UMo-5 | 5                              | 24          | 1                           | 20400                         | 4.5                       |
| UMo-6 | 7                              | 20          | 0.4                         | 103600                        | 11                        |
| UMo-7 | 4                              | 20          | 1                           | 17000                         | 6                         |

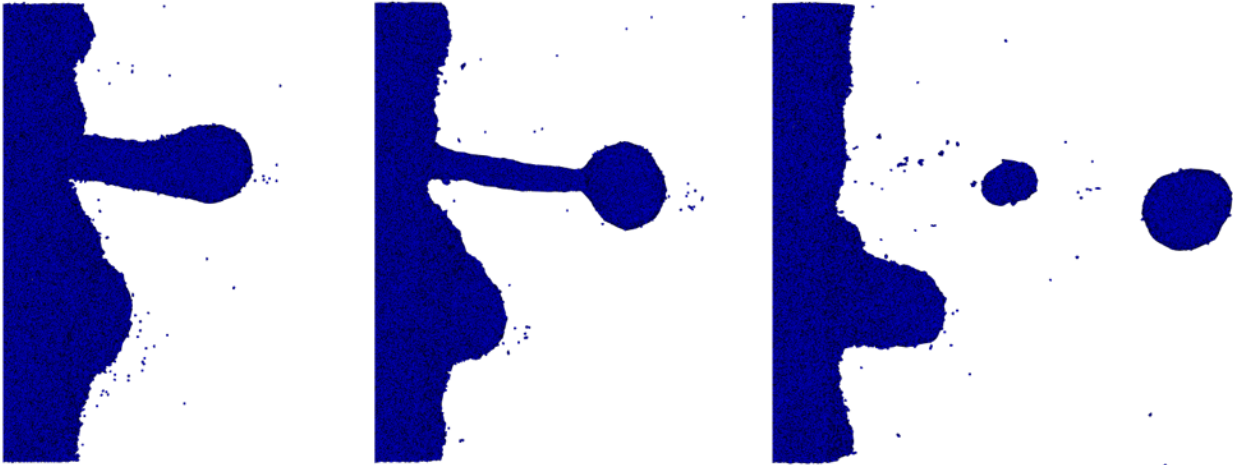
The number and mass PSDs of the droplets obtained by the SPH simulations for different input parameters are presented in figure IV.12. In the analysis proposed, the results are presented for a constant  $Re_T$  number (constant rotation speed) to study the effect of the flow rate on the PSD. Similarly, a constant  $Re_E$  number (constant flow rate) is considered to study the effect of the rotation speed.

The PSDs derived from the SPH simulations showed that, for the same rotation speed, the droplet size and the width of the PSD slightly increase with increasing liquid mass flow rate, which is similar to previous studies [164]. This observation also agrees with the semi-empirical models presented in chapter I. Concerning the rotation speed, when the latter is increased, the PSD becomes narrower and a shift to finer diameters is observed. This observation is also in line with the semi-empirical models.

The shape of the PSDs suggests a unimodal distribution, unlike the results obtained experimentally [15, 25]. However, for the atomization in the LD regime, a small peak can be observed in the PSD just before the main peak, indicating that satellite droplets were produced for some of the main droplets (figure IV.11).



(a) UMo-5 (31 krpm)



(b) UMo-7 (40 krpm)

FIGURE IV.11: Atomization in the LD regime ( $Q=17.4$  g/s)

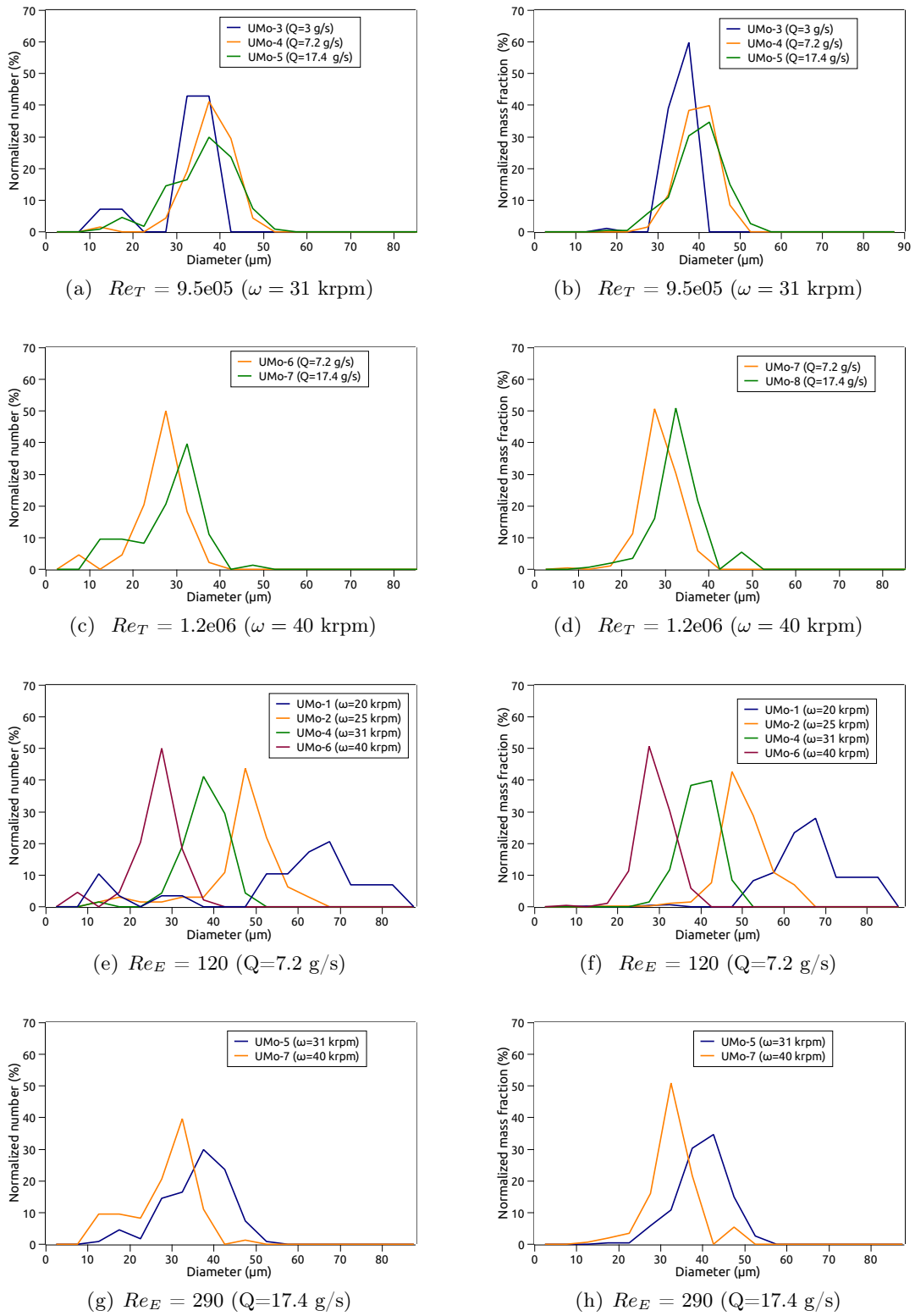


FIGURE IV.12: Number-PSD (left) and Mass-PSD (right) for UMo.

In addition, figure IV.13 shows the effect of the  $Re_T$  and  $Re_E$  numbers on the cumulative undersize mass fraction.

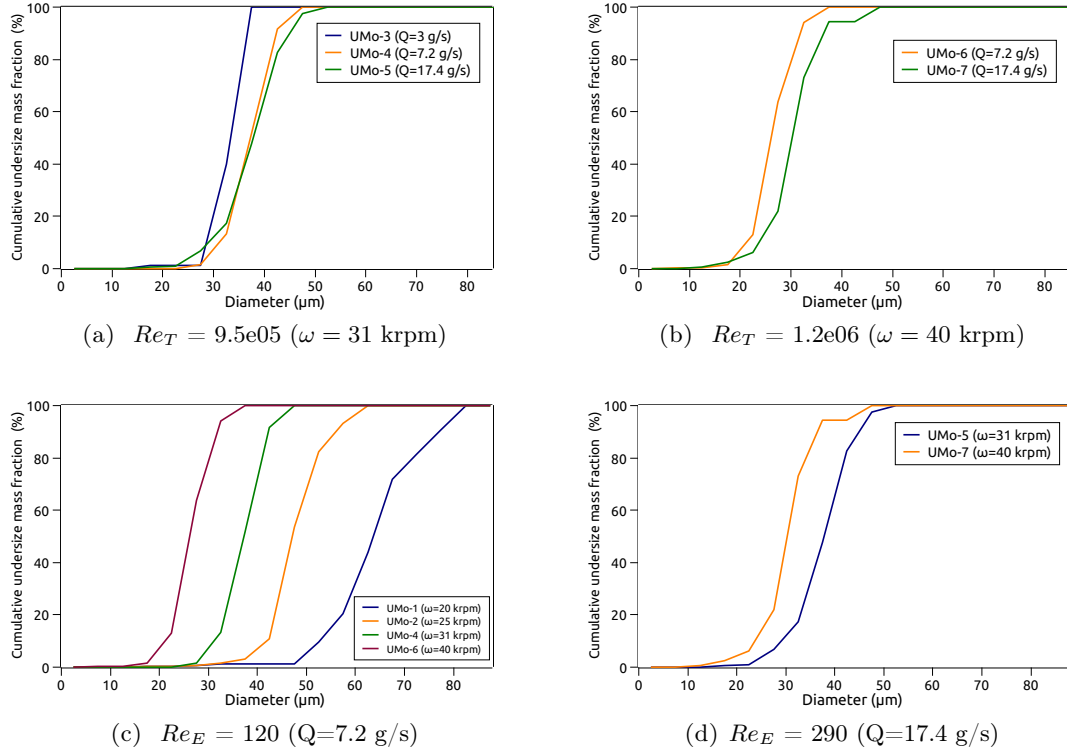


FIGURE IV.13: Cumulative mass fraction distribution for different  $Re_T$  and  $Re_E$  numbers.

The characteristic diameters obtained from the corresponding cumulative undersize distribution, the calculated Sauter Diameter  $D_{32}$  and the normalized/relative standard deviation for each simulation are summarized in table IV.5.  $D_{32}$  calculated by the semi-empirical models presented in chapter I for the corresponding rotation speed and flow rate are also presented in table IV.5. All diameters are expressed in  $\mu m$ .

TABLE IV.5: Characteristic diameters for SPH simulations and semi-empirical models.

| #     | $D_{m,10}$ | $D_{m,50}$ | $D_{m,90}$ | $D_{32}$ | Std | $D_{32}$ Champagne & Angers | $D_{32}$ Kim et al. | $D_{32}$ Schenk et al. | # particles |
|-------|------------|------------|------------|----------|-----|-----------------------------|---------------------|------------------------|-------------|
| UMo-1 | 56         | 67         | 80         | 67       | 0.3 | 99                          | 78                  | 105                    | 30          |
| UMo-2 | 44         | 49         | 59         | 49       | 0.2 | 79                          | 62                  | 85                     | 64          |
| UMo-3 | 32         | 36         | 39         | 35       | 0.3 | 58                          | 45                  | 62                     | 12          |
| UMo-4 | 33         | 39         | 44         | 39       | 0.1 | 64                          | 51                  | 69                     | 68          |
| UMo-5 | 31         | 40         | 46         | 39       | 0.2 | 71                          | 56                  | 76                     | 110         |
| UMo-6 | 23         | 27         | 34         | 28       | 0.2 | 50                          | 39                  | 53                     | 45          |
| UMo-7 | 27         | 33         | 37         | 32       | 0.2 | 55                          | 44                  | 59                     | 73          |

The three semi-empirical models express the ratio between the Sauter diameter and the rod diameter as a function of  $Re_E^{0.12} Re_T^{-0.98} Oh^{-0.86}$ . In order to compare the mean Sauter

diameter predicted by SPH simulations with the semi-empirical models, the dimensionless diameter  $\frac{D_{SPH-32}}{D_{rod}}$  is expressed as a function of  $Re_E^{0.12} Re_T^{-0.98} Oh^{-0.86}$  as follows:

$$\frac{D_{SPH-32}}{D_{rod}} = \beta Re_E^{0.12} Re_T^{-0.98} Oh^{-0.86} \quad (IV.17)$$

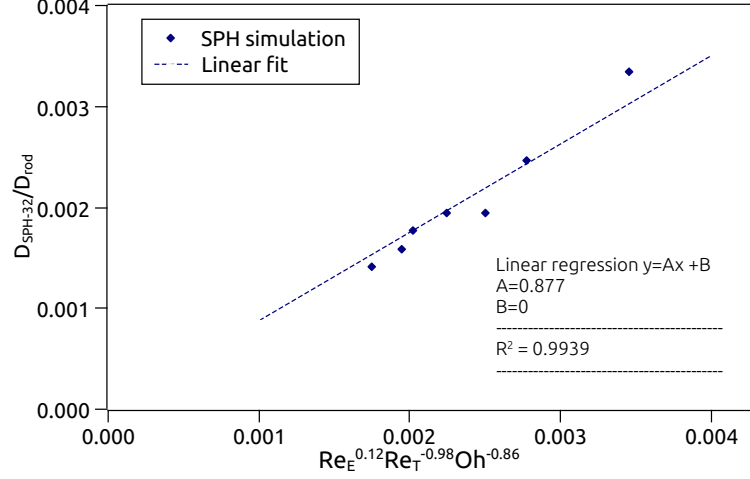


FIGURE IV.14: Linear regression analysis of SPH diameters  $D_{32}$ .

From the result presented in figure IV.14, it was found that the SPH simulations agree with respect to the semi-empirical model with a proportionality constant. For this case, the  $\beta$  coefficient was found equal to 0.88.

TABLE IV.6: Comparison between SPH and semi-empirical models for estimating the mean Sauter diameter.

| Model                  | $\beta$ |
|------------------------|---------|
| SPH                    | 0.88    |
| Champagne & Angers [9] | 1.42    |
| Kim et al. [30]        | 1.12    |
| Schenk et al. [15]     | 1.52    |

Table IV.6 compares  $\beta$  coefficients of the SPH numerical model with the semi-empirical models. The results show that the SPH model tends to under-estimate the droplet diameter. By comparing the SPH mean Sauter diameter with the average of  $D_{32}$  obtained by the other three models, we obtain the following:

$$\frac{D_{SPH-32}}{D_{semi-empirical-32}} = 0.65 \quad (IV.18)$$

The shift between the SPH results and the semi-empirical models can also be expressed as follows:

$$D_{SPH-32} = D_{semi-empirical-32} - 0.44 Re_E^{0.12} Re_T^{-0.98} Oh^{-0.86} \quad (IV.19)$$

There are several likely reasons to explain the unexpectedly low value for  $\beta_{SPH}$ . First, in the SPH model, the phase film thickness is considered to be independent of  $r$  or  $\theta$ . However, experimentally this is not the case. Possibly because the heating is not homogeneous, the surface of the rod after fragmentation is not smooth. There are rather scratches that may correspond to preferential paths for the liquid metal (see figure IV.15). This means that the local mass flow rate is more important than the average flow rate, which leads to an increase in the diameter of the atomized droplets.

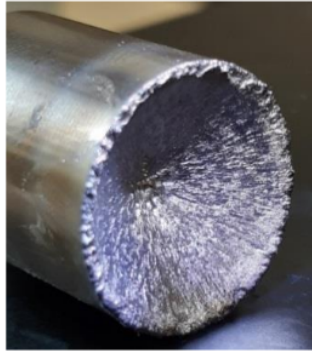


FIGURE IV.15: Example of partial rod atomization.

Second, the effect of the gas in the atomization chamber is not considered. In fact, there are two competing actions of the gas in affecting the droplet size. The gas is assumed to promote the disturbance of the liquid melt surface facilitating thus the atomization process and leading to the production of finer particles. On the other hand, the gas could play an important role in increasing the cooling rate of the liquid by increasing the convective heat transfer coefficient between the melt and the atmosphere. This decrease in the temperature is accompanied with a change in the fluid properties, mainly an increase in the viscosity which makes the atomization process more difficult. Recently, the effect of the gas in the atomization chamber was verified by Zhao et al. [164]. They found that when increasing the gas flow rate experimentally in a plasma rotating electrode process, the mean powder size increased. Furthermore, their numerical study on the atomization process showed the competing effect of the gas blast on the mean powder size.

Finally, the stability of the liquid film close to the inlet zone can play an important role in the dynamics of the fragmentation process. These numerical instabilities can facilitate the fragmentation process which can explain the smaller size of the SPH droplets. To have a better stability near the inlet zone area, solid wall particles were used on the top of the liquid film in order to create some sort of a small control box (figure IV.16). In addition, to ensure that the inlet flow is not disturbed by surface tension force, the surface tension coefficient is increased linearly from 0 at the fluid inlet zone to its real value just before the rod edge. It should be noted that this is a strong hypothesis that could have an effect on the droplets final diameter. In general, the surface tension force enhances the stability of the liquid film, and the atomization occurs only when the centrifugal force overcomes the viscous and surface tension forces. This means that a decrease in the surface tension coefficient promotes the liquid atomization process leading to finer powders. Improvement scenarios to stabilize the liquid film near the inflow zone are proposed in the conclusions



and perspectives chapter.

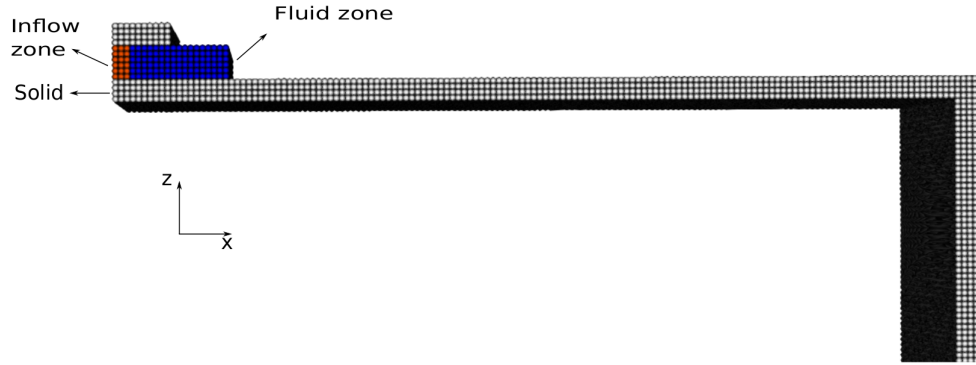


FIGURE IV.16: Representation of the inflow zone for the REP simulation.

The variation of  $D_{m,10}$ ,  $D_{m,50}$  and  $D_{m,90}$  can be also obtained as a function of the dimensionless numbers (see figure IV.17). With a linear regression analysis, the expression of these characteristic diameters can be expressed as follows:

$$\frac{D_{m,10}}{D_{rod}} = 0.74 Re_E^{0.12} Re_T^{-0.98} Oh^{-0.86} \quad (IV.20)$$

$$\frac{D_{m,50}}{D_{rod}} = 0.89 Re_E^{0.12} Re_T^{-0.98} Oh^{-0.86} \quad (IV.21)$$

$$\frac{D_{m,90}}{D_{rod}} = 1.03 Re_E^{0.12} Re_T^{-0.98} Oh^{-0.86} \quad (IV.22)$$

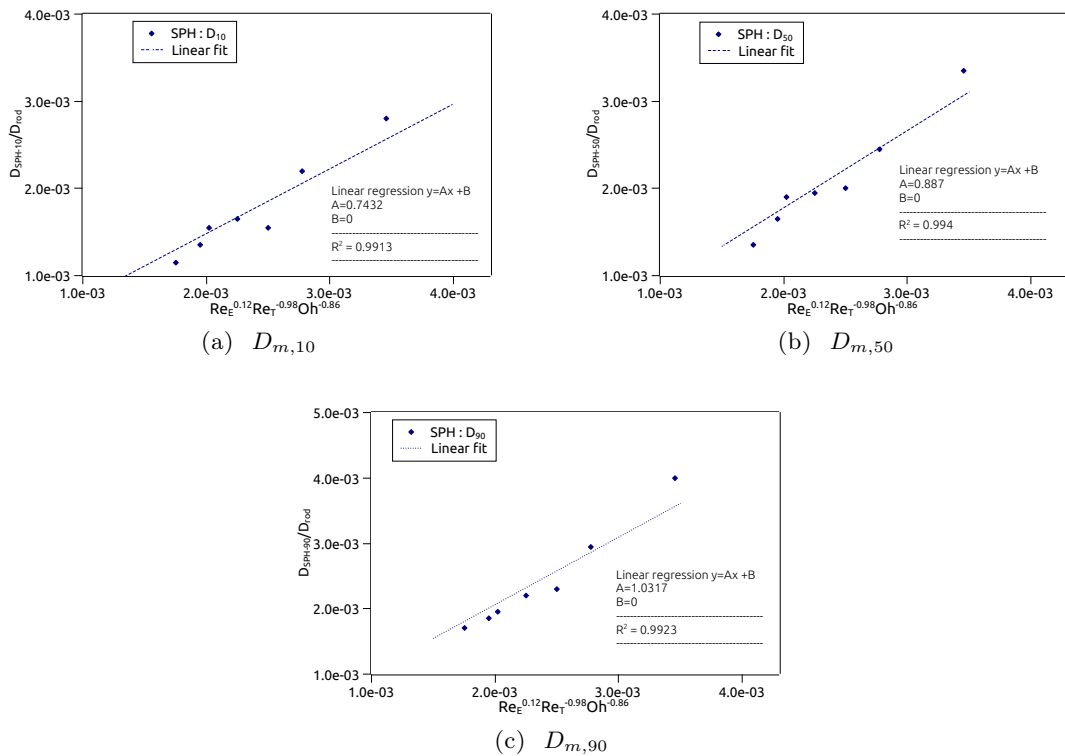


FIGURE IV.17: Linear regression analysis for SPH diameters:  $D_{m,10}$ ,  $D_{m,50}$  and  $D_{m,90}$ .

For its applications purposes, CERCA is interested in droplets having a diameter ranging between 0-40  $\mu\text{m}$ , 40-100  $\mu\text{m}$  and 100-125  $\mu\text{m}$ . According to the simulation results, the dimensionless numbers ( $Re_E$ ,  $Re_T$ ) for obtaining these diameters, assuming that  $Oh = 0.00036$ , are presented in figure IV.18.

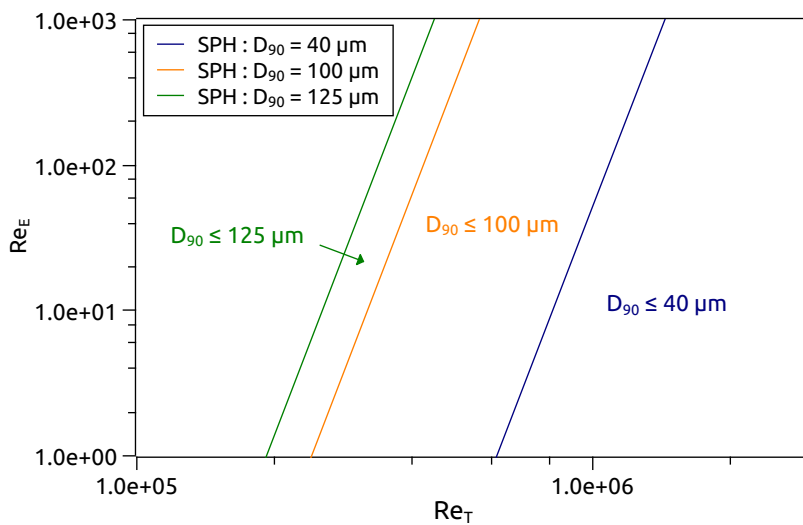


FIGURE IV.18: SPH results for  $D_{m,90}$  as a function of  $Re_T$  and  $Re_E$  for  $Oh = 0.00036$ .

---

### IV.3.2.3 Droplet formation frequency

Experimentally, the frequency at which the droplets are ejected can be calculated based on the flow rate in the steady state regime, the mean particle size diameter  $D_{m,50}$  and the distance between the two ejected droplets or two ligaments  $d$ , as illustrated in figure IV.19. By assuming that the ejection points (places where the droplet break-away from the rod edge) are evenly distributed at the periphery of the rod, the frequency can be expressed as:

$$F = \frac{Q}{\frac{\pi}{6} D_{m,50}^3} \frac{d + D_{m,50}}{\pi D_{rod}} \quad (\text{IV.23})$$

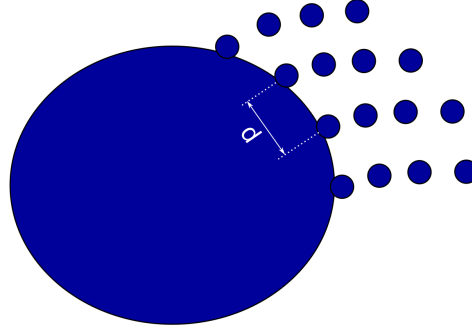


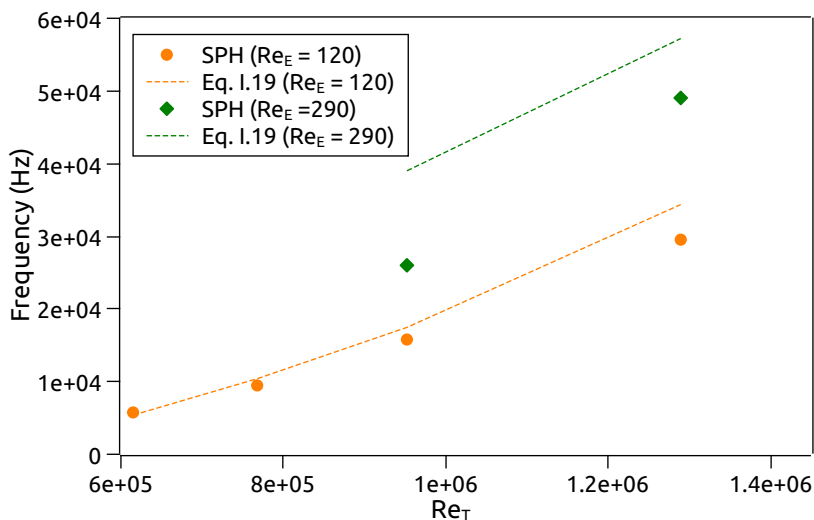
FIGURE IV.19: Schematic representation of the distance between two droplets.

From the SPH numerical results, the droplet generation frequency for each simulation is estimated by dividing the total number of droplets ejected in one streamline by the simulation duration. This frequency is presented in figure IV.20 as a function of the rotation speed ( $Re_T$ ) and the flow rate ( $Re_E$ ). It can be deduced that the frequency increases with the rotation speed and/or the flow rate.

The objective is to compare these frequencies with equation IV.23, except that the distance between two ejected particles is obtained using SPH simulations and not from theoretical or experimental data. This distance is measured at the rod periphery for each simulation, see table IV.7. The results show that this distance is almost equal to the mean Sauter diameter. Figure IV.20 shows good agreement between the measured and calculated frequencies for  $Re_E = 120$  with a difference below 14 %. For  $Re_E = 290$ , calculated and SPH frequencies have the same tendency and are of the same order of magnitude. However, the calculated frequency is higher by almost 30% than the one measured with the SPH simulation. The reason could be that the measured distance between two droplets is not accurate and should be smaller than the mean diameter. Another reason may be that the assumption of a uniform distance between the ejection points could be too crude.

TABLE IV.7: Measured distance  $d$  between two particles in SPH simulations.

| #     | $d$ ( $\mu m$ ) | $D_{32}$ ( $\mu m$ ) |
|-------|-----------------|----------------------|
| UMo-1 | 65              | 67                   |
| UMo-2 | 52              | 49                   |
| UMo-4 | 43              | 39                   |
| UMo-5 | 37              | 39                   |
| UMo-6 | 26              | 27                   |
| UMo-7 | 28              | 32                   |

FIGURE IV.20: Droplet generation frequency as a function of  $Re_T$  and  $Re_E$ .

### IV.3.3 Effect of external vibrations

As explained in chapter I and as seen in the validation example of chapter III, the fragmentation process can be controlled by applying external vibrations to trigger the fragmentation phenomenon. This was tested numerically on the REP by imposing the solid below the liquid film to move vertically in a sinusoidal form according to equations III.26 and III.27. The vibrations were applied for the fragmentation in the LD regime, as the case considered by Zainoun et al. [138]. The input parameters of simulation # UMo-5 (table IV.1) were considered. The maximum amplitude ( $A_0$ ) and frequency ( $F$ ) of the vibrations were varied between 1 to 10  $\mu m$  and 10 to 40 kHz, respectively. The droplets are detached from the rotating rod at a frequency around 20 kHz. Table IV.8 presents a list of the tested Amplitude/Frequency combinations. The acceleration due to the vibrations is calculated by:  $a_{vib} = A_0(2\pi F)^2$ . This acceleration is compared to the centrifugal acceleration, which is equal to 10000 g in this case. The ratio between these two accelerations is defined as:  $\Upsilon = \frac{a_{vib}}{a_{centrif}}$ .

TABLE IV.8: List of SPH simulations with vibrations.

| #       | $A_0(\mu m)$ | F (kHz) | Relative acceleration $\Upsilon$ |
|---------|--------------|---------|----------------------------------|
| UMo-5   | 0            | 0       | 0                                |
| UMo-5-a | 1            | 10      | 0.04                             |
| UMo-5-b | 1            | 20      | 0.16                             |
| UMo-5-c | 1            | 40      | 0.63                             |
| UMo-5-d | 10           | 20      | 1.6                              |
| UMo-5-e | 4            | 20      | 0.63                             |
| UMo-5-f | 2            | 28.3    | 0.63                             |

For simulation # UMo-5-d, it was found that the SPH particles tend to adhere to the peripheral rod surface instead of detaching, as it can be seen from figure IV.21. That is, droplets were not obtained for this set of parameters. This can be explained by the fact that the acceleration due to the vibrations is 1.6 times higher than the rotation acceleration. This means that the physical mechanism at hand has changed, and the centrifugal force is no longer the dominant one. Instead, the vertical shear stress becomes very important and because complete wetting is considered, the adhesion phenomenon is observed in this case. Subsequently and as part of this study, the acceleration due to vibrations was limited to 6300 g and various combinations (Frequency/Amplitude) allowing to obtain this acceleration were tested.

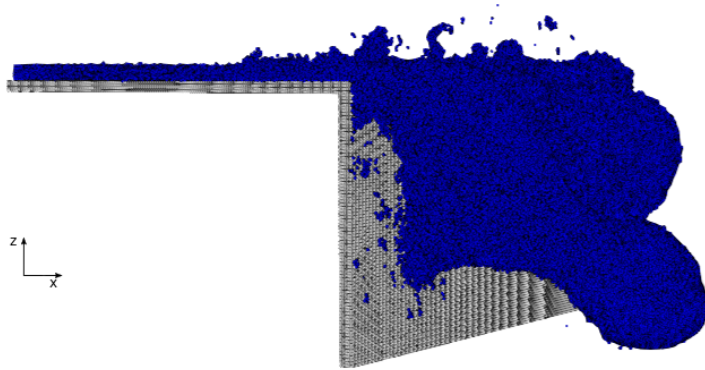


FIGURE IV.21: Adhesion of fluid particles on the solid rod for simulation # UMo-5-d.

No significant change was observed in the PSD, as shown in figure IV.22a, meaning that the effect of the vibrations is not remarkable for the tested configurations. It should be noted also that these vibrations did not affect the frequency of the droplets detachment, which remained equal to about 20 kHz. However, the standard deviation of the droplet diameters tends to slightly decrease by increasing the acceleration of the vibrations, as it can be seen from figure IV.22b. Unexpectedly, this decrease is related to the acceleration and was observed for any frequency and not only for that of droplets detachment.

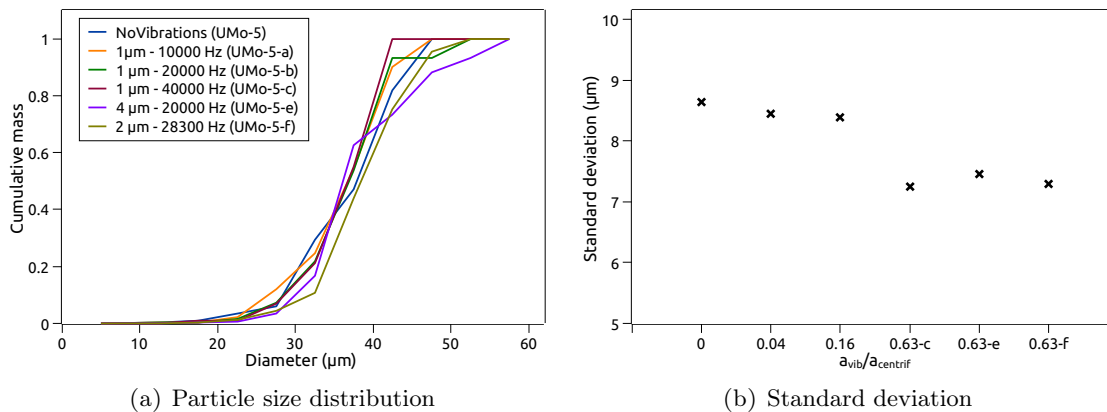


FIGURE IV.22: Effect of applying vibrations on the a) PSD and b) Standard deviation.

Unlike the simulations for the uni-directional jet break-up presented in the previous chapter, the vibrations in the REP configurations seems not to have an important effect on the mean particle diameter nor on the total PSD. This can be explained by mainly two reasons. In the first configuration, the vibrations were applied in the direction of the jet, contrary to the REP configuration where the vibrations were applied orthogonally to the jet. In addition, contrary to the unidirectional jet configuration, the fluid in the REP configuration has two degrees of freedom (the melt can move in the  $x$  and  $y$  directions). This also explains why in this case the stress due to vibrations is not transmitted to the liquid as effectively as in the case of a uni-directional jet.

## IV.4 Conclusions

The effect of varying the operational parameters and adding external vibrations on the UMo REP atomization process was studied. The conclusions are summarized as follows:

1. The Sauter diameter and the average frequency of droplet generation can be defined as a function of three dimensionless numbers ( $Re_E$ ,  $Re_T$  and  $Oh$ ).
2. By increasing the rotation speed, the droplet size decreases and the PSD becomes narrower.
3. In addition to the rotation speed, changing the mass flow rate can also affect the PSD. Bigger droplets can be obtained for a higher mass flow rate, with a slight increase in the width of the PSD.
4. Adding external vibrations in a direction perpendicular to the fluid flow has a very small effect on the PSD. The droplet mean diameters are not affected by these vibrations. However, a small decrease in the standard deviation is observed when the acceleration of the vibrations is important, which means that the droplets diameters distribution is more mono-disperse. This decrease depends mainly on the acceleration of the applied vibrations and not on their frequencies. It could be interesting to test different frequencies and check if there exist a frequency range where the PSD is slightly narrower (smaller standard deviation).

- 
5. The heating phenomenon plays an important role in defining the mass flow rate and the film thickness. Besides, the heat transfer between the melt and the gas in the atomization chamber can affect the fluid properties. Therefore, it would be interesting to further complete the model in order to take into account the thermal aspects.
  6. With the results obtained by the SPH simulations, expressions were defined for the characteristic diameters:  $D_{m,10}$ ,  $D_{m,50}$ ,  $D_{m,90}$  and  $D_{32}$ , as a function of the operational parameters represented by three dimensionless numbers:  $Re_E$ ,  $Re_T$  and  $Oh$ .





# Conclusions and perspectives

This work focuses on the development and validation of Smoothed Particle Hydrodynamics (SPH) formulations for the simulation of the fragmentation of thin liquid films, with the principal aim to simulate metallic powder production with the Rotating Electrode Process (REP). To achieve this objective, the numerical development was based on the weakly compressible SPH code developed by S. Adami and his team at the Institute of Aerodynamics and Fluid Mechanics at TUM.

After establishing the state of the art of the REP atomizer and the SPH method, the work was focused on three main areas. First, a proper surface tension model needed to be implemented for free surface flows. For that matter, different techniques for applying surface tension force, all based on the CSF approach, were compared. As a result, a model was chosen and implemented for detecting surface particles in free surface flow and applying surface tension force. The implementation was successfully tested with common test cases found in the literature: Square droplet and Droplet oscillation.

The second line of research is the development of a new correction method to estimate and correct the density near the free surface. The idea behind this method is to estimate the empty volume of the support domain due to the missing particles as a function of the distance to the surface and the curvature of this surface. This new method was implemented in 3D and tested for the Cube droplet test case and the Rayleigh-Plateau instability. By comparing this technique to the Shepard correction technique, the results show that this new method improved significantly the stability of the simulation, the density profile near the free surface and the particle re-arrangement. It should be noted that this method depends greatly on the curvature calculation and on the accuracy in detecting surface particles.

Lastly, small implementations and calculations were made to adapt the SPH code to be able to simulate the REP atomizer. Because of the high computational cost, an inflow boundary condition needed to be implemented to simulate a small part near the edge of the rotating rod. For that, a buffer zone was created for the fluid inlet. A prescribed pressure and velocity profile was imposed on the particles in this buffer zone. The implementation was verified with the Poiseuille flow test case. With the adopted geometry of the REP simulation, it is necessary to calculate the flow velocity profile and the film thickness as a function of the operational parameters. Thus, an analytical set of equations was detailed to calculate these quantities. Combining all modifications together, the overall SPH implementation was validated with the fragmentation of a unidirectional water jet. The

SPH model has proven to be a suitable tool to reproduce experimental and theoretical data.

Finally, regarding the applicability of what has been developed, a simulation list was carried out to study the effect of the operational parameters of the REP atomizer and investigate the impact of imposing vibrations on the droplets size. Qualitatively, the SPH model can reproduce the differences between the DDF and LD regimes. As for the droplets size, it was found that the Sauter diameter obtained by the SPH model is smaller than the one predicted by the semi-empirical models by a unique multiplicative constant. One of the main reasons is the simplifications taken for simulating the REP atomizer. The average size of the drops decreases by increasing the rotational speed and/or decreasing the flow rate of liquid metal (correlated to the laser heating power). Expressions for  $D_{10}$ ,  $D_{50}$  and  $D_{90}$  were obtained as a function of the dimensionless numbers:  $Oh$ ,  $Re_E$  and  $Re_T$ . Regarding the effect of the vibrations, the study showed that vibrations applied to the solid rod in the direction perpendicular to the liquid film do not have a significant effect on the particle size distribution, in the investigated REP configuration.

Nevertheless, some improvements can be proposed to achieve a better simulation of the REP atomizer. With regards to the surface tension model, it would be interesting to develop a proper contact angle model taking into account the wetting between the liquid melt and the solid rod. A virtual interface method can be implemented similar to the one proposed by Dong *et al.* [165]. The idea is to identify the contact point between the liquid and solid and create a virtual interface at this point by dividing the wall particles into two types (liquid or gas) according to the desired contact line. By applying this method the surface tension force can work as an adjustment force that tends to equilibrate the dynamic line into the equilibrium contact angle. As for the density correction method, a more precise representation of the surface and a more accurate calculation of the curvature will definitely lead to a better density correction for particles near the free surface.

Another improvement is in implementing angular periodic boundary conditions. Because of the absence of rotational periodicity, the system studied was reduced to a small rectangle at the edge of the rotating rod. With this improvement, an angular sector of the rotating rod could be simulated and not only its edge, and the Coriolis effect could also be included. Another advantage is that the distance travelled by the liquid flow prior to the break-up is larger and thus the problem of achieving a better stability for the particles shifting from the inlet buffer zone to the fluid zone could be solved. For example, in the actual version of the model, the surface tension force and the vibrations amplitude are gradually imposed to fluid particles and they reach their maximum values only at the edge of the rotating rod.

In fact, the stability of the liquid film over the rotating rod and more precisely close to the inlet zone may play an important role in the fragmentation process. Numerical instabilities can affect the force balance and subsequently affect the fragmentation process. This is why it seems relevant to work on the improvement of the stability near the inflow zone. One of the solutions could be the adaptation of the calculation of the curvature and the surface tension force in this region, which will of course affect the density calculation as well.

---

Ultimately, a more advanced SPH model including a coupling of heat transfer and fluid mechanics should be foreseen to simulate more precisely the REP atomizer, which will allow for further experimental validation. With implementing a proper heat transfer model, the cooling of the liquid film at the edge of the rotating rod can be studied as well as the effect of the non-homogeneity of the liquid film. The laser could be simulated by simply using the SPH heat conduction equation or by using a Ray tracing algorithm to track the propagation of the laser beam [166], which is currently under development in the SPH code used for this work. The main problem here is the high computational cost because first the phase change and the liquid break-up do not occur at the same time scales and second a finer discretization is needed to model the phase change from solid to liquid.



# Appendix **A**

## Experimental study: Influence of vibrations on the break-up of unidirectional liquid jets

The experimental set-up is described in chapter III. The images taken by the fast camera are analyzed using Matlab. Two fluids have been tested: water and Bolton 117 alloy with a melting temperature of 47 °C. For the metal jet to be fragmented, it is necessary to create an inert atmosphere and avoid oxidation. For this, a casing was designed to control the atmosphere at the exit of the jet (figure A.1).

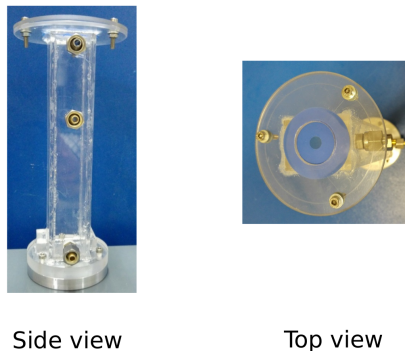


FIGURE A.1: Photos of the casing for metal fragmentation.

### Experiments with water

First, the influence of the direction of the vibrations compared to that of the jet was studied. Two orientations of the piezo-electric cell were tested (figure A.2):

- Vertical: in the direction of the jet
- Horizontal: perpendicular to the direction of the jet

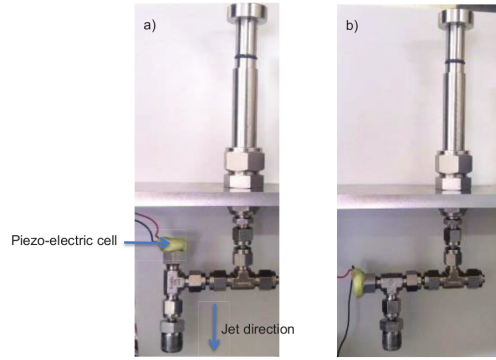


FIGURE A.2: Orientation of the piezo-electric cell: a) Vertical and b) Horizontal.

For both cases, a disk with an orifice diameter of around  $52 \mu\text{m}$  was used, with a jet speed equal to  $11.2 \text{ m/s}$ . In these conditions the Rayleigh frequency is equal to  $49.5 \text{ kHz}$ . The frequency of the vibrations was varied manually by scanning the interval between  $0$  and  $100 \text{ kHz}$ . By viewing the jet at the output, whenever a change in the diameter of the droplets is observed, the frequency is recorded and pictures of the droplets are taken. There are possibly optimal frequencies that have not been detected.

TABLE A.1: Droplets mean diameter as a function of the frequency for different orientations of the piezo-electric cell.

|                                      |  | Vertical orientation   |      |      |       |      |      |
|--------------------------------------|--|------------------------|------|------|-------|------|------|
| Frequency (kHz)                      |  | 0                      | 15.4 | 28   | 49.55 | 55.4 | 79.7 |
| $D_{mean}(\mu\text{m})$              |  | 85                     | 123  | 99   | 76    | 69   | 77   |
| Standard deviation ( $\mu\text{m}$ ) |  | 24.8                   | 6.2  | 6.3  | 9.4   | 17.5 | 25.5 |
| Photo of the jet                     |  |                        |      |      |       |      |      |
|                                      |  | Horizontal orientation |      |      |       |      |      |
| Frequency (kHz)                      |  | 0                      | 20.8 | 28.7 | 33    |      |      |
| $D_{mean}(\mu\text{m})$              |  | 85                     | 110  | 95   | 84    |      |      |
| Standard deviation ( $\mu\text{m}$ ) |  | 24.8                   | 14.9 | 24.2 | 11.8  |      |      |
| Photo of the jet                     |  |                        |      |      |       |      |      |

Table A.1 shows the average diameter and its standard deviation as a function of the frequency, for the two piezo-electric cell orientations. Between  $3000$  and  $4000$  droplets were considered for the statistical study. From these results, it appears that the vibrations are transmitted to the jet in both configurations. However, with the vertical orientation, the jet is more regular and thus the vibrations effect is more important. It confirms that the

orientation of the piezo-electric cell has an effect on the jet fragmentation.


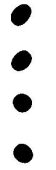
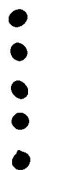


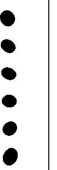


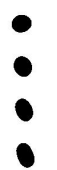
In the series of experiments presented above, a drilled disk glued to the atomization system was used to generate droplets. The problem with this configuration is that after a certain number of cycles, the disk detaches from the system. In most cases, while trying to glue it again, the hole get obstructed by some impurities and so another disk should be used. Its potentially different diameter makes the reproducibility study more difficult. To avoid this problem and in order to have a tight system for better vibration transmission, the glued disk was replaced by a machined and laser drilled Swagelok tip. In this second configuration, a series of experiments was conducted with an orifice of diameter around  $150 \mu\text{m}$ , with different output velocities:

- $u_1 = 5.5 \text{ m/s} \Rightarrow F_{Rayleigh} = 8.7 \text{ kHz}$
- $u_2 = 8.7 \text{ m/s} \Rightarrow F_{Rayleigh} = 12.7 \text{ kHz}$
- $u_3 = 12.2 \text{ m/s} \Rightarrow F_{Rayleigh} = 17.8 \text{ kHz}$

Table A.2 presents the results of this study. There exists a frequency range in which the size distribution of droplets is controlled. This frequency depends on the jet speed:

- $u_1 = 5.5 \text{ m/s} \Rightarrow \text{Frequency range} = [7-11] \text{ kHz}$
- $u_2 = 8.7 \text{ m/s} \Rightarrow \text{Frequency range} = [9-22] \text{ kHz}$
- $u_3 = 12.2 \text{ m/s} \Rightarrow \text{Frequency range} = [11-23] \text{ kHz}$






TABLE A.2: Droplets mean diameter as a function of the frequency for different jet speed.

| Velocity (m/s)                       | 5.5   |   |   | 8.7   |  |   | 12.2  |   |   |
|--------------------------------------|---|---|---|---|--|---|---|---|---|
| Frequency (kHz)                      | 8   | 9   | 11  | 11  | 14   | 21  | 11  | 17  | 22  |
| $D_{mean}(\mu\text{m})$              | 317   | 295   | 269   | 313   | 297  | 233   | 337   | 276   | 296   |
| Standard deviation ( $\mu\text{m}$ ) | 24.2  | 18.6  | 21.5  | 12.5  | 7.7  | 15  | 18.2  | 13.2  | 9.7   |
| Photo of the jet                     |  |  |  |  |  |  |  |  |  |

## Experiments with liquid metal (Bolton 117)

For the metal experiments, the casing was filled with nitrogen in order to reduce the concentration of oxygen in the range of 35 to 50 ppm. To compare the results between water and Bolton 117, the same machined part (Swagelok) with a diameter of around  $150 \mu\text{m}$  was used with a jet speed of  $u_1 = 5.5 \text{ m/s}$ . The Rayleigh frequency is also 8.7 kHz since it does not depend on the material used ( $F_{Rayleigh} = 0.222 \frac{u}{D_{jet}}$ ). The results are presented in table A.3.

TABLE A.3: Droplets mean diameter as a function of the frequency for metal break-up.

| Frequency (kHz)                      | 3   | 4   | 5   | 6   | 7   |
|--------------------------------------|---|---|---|---|---|
| $D_{mean}(\mu\text{m})$              | 302   | 288   | 247   | 211   | 202   |
| Standard deviation ( $\mu\text{m}$ ) | 21  | 15.8  | 27  | 31.6  | 30  |
| Photo of the jet                     |  |  |  |  |  |

These results show almost the same behavior as with water: there is an optimal frequency range where the particle size distribution is regular and the average diameter tends to decrease by increasing the frequency of the vibrations. However, this optimal frequency range is 3-7 kHz compared with 7-11 kHz in the case of water for the same experimental conditions. In addition, for the same frequency, the water droplets are larger than metal droplets (figure A.3). According to the formulas found in the literature and for small values of  $Oh$  number ( $Oh = 0.01$ ), the Rayleigh frequency and the droplet diameter do not depend on the material used (table I.2). The difference between water and metal droplet sizes and optimal frequencies could be caused by the differences between the two devices:

- Presence of the casing for controlling the atmosphere. This casing is in contact with the Swagelok for the jet orifice and so can alter the vibrations.
- Mass difference between the two systems leading to a different inertial damping.

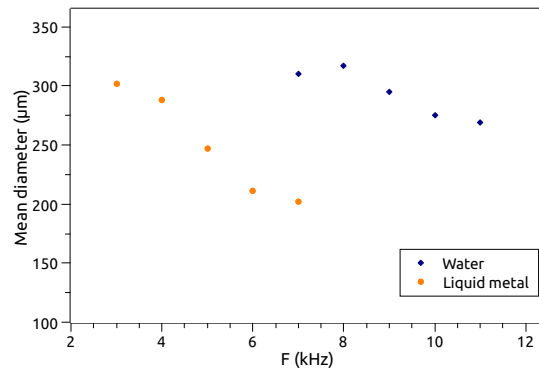


FIGURE A.3: Mean droplet diameter as a function of the frequency for a jet diameter of  $150 \mu\text{m}$  and a jet velocity of  $5.5 \text{ m/s}$ .



# Appendix B

## Convergence study

A numerical model is convergent if the solution approaches a fixed value with an increase in the domain refinement or a decrease in the time step. In the case in hand, three convergence studies were conducted: the sensitivity of the numerical model was tested to the space and time step and to the chosen geometry (size of the system).

Based on the analytical calculation presented in chapter IV, the thickness of the liquid film varies between 2 to 6  $\mu\text{m}$ . Given the size of the support domain of the chosen kernel function, at least three SPH particles must be considered to represent the fluid phase. The objective here is to chose the suitable space discretization that gives accurate results while minimizing the computational cost. That is, 3 to 6 layers of fluid particles are considered in the film thickness. To test the convergence of the SPH model, the PSD from two simulations were compared. The first reference simulation having a space discretization of  $dx$  with 4 SPH particles in the fluid thickness and the second simulation with dividing by 2 the distance between the particles ( $0.5dx$  or 8 SPH particles in the fluid thickness). Similarly, to study the convergence to the time step, two simulations were considered: the reference test case with a time step  $dt$  and the second simulation with a time step equal to  $0.5dt$ . Finally, the sensitivity of the model to the size  $L$  (see figure IV.1) of the system was studied. For that, a simulation was performed with twice the width  $2L$  and compared with the reference configuration. The results are presented in table B.1. The mean diameter and the standard deviation for each simulation are compared with the reference test case ( $dx$ ,  $dt$ ,  $L$ ).

TABLE B.1: Convergence study of the numerical model.

|                         |        |        |    | $D_{32}(\mu\text{m})$ | Std ( $\mu\text{m}$ ) | Number of droplets |
|-------------------------|--------|--------|----|-----------------------|-----------------------|--------------------|
| Reference (UMo-5)       | dx     | dt     | L  | 38.9                  | 8.7                   | 110                |
| Space convergence       | 0.5 dx | dt     | L  | 33.7                  | 13.5                  | 5                  |
| Time convergence        | dx     | 0.5 dt | L  | 38.1                  | 9                     | 48                 |
| System size convergence | dx     | dt     | 2L | 38.5                  | 9                     | 39                 |

By analysing the obtained values, it is noticed that the change in the Sauter mean diameter  $D_{32}$  is insensitive to the space and time resolution and to the system size. For a

more qualitative comparison, the normalized cumulative undersized mass fraction for each simulation is represented in figure B.1. The presented PSD for the different simulations are almost the same. The difference observed for the space convergence simulation (0.5 dx) is attributed to poor statistical representation where only 5 particles are considered due to time constraints. Therefore, it can be considered that the numerical convergence of the SPH model is achieved. In fact, this model is very sensitive to the curvature and thus, if we increase further the space discretization (decrease in dx), the error in the curvature calculation becomes more important and thus the stability of the numerical model will be affected.

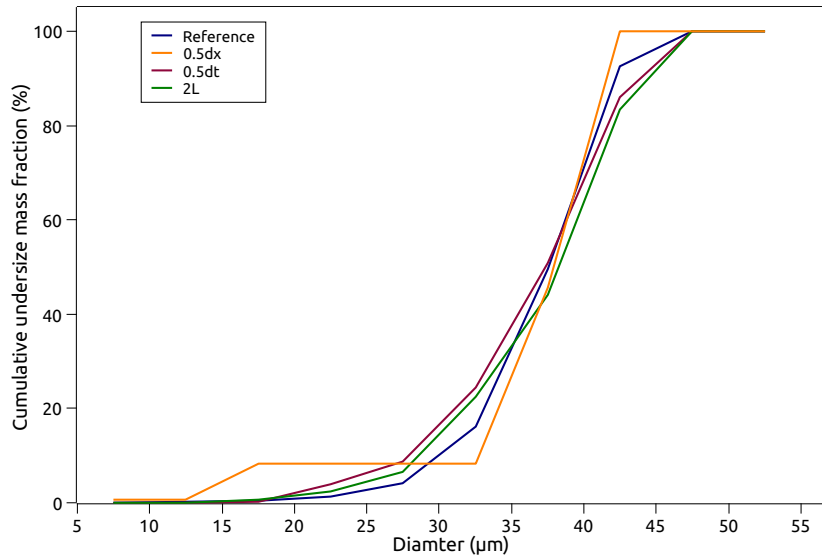


FIGURE B.1: Numerical convergence.

# Bibliography

- [1] *The HERACLES Consortium: Fuel Manufacturing.*
- [2] R. M. German, « Powder metallurgy science », *Metal Powder Industries Federation, 105 College Rd. E, Princeton, N. J. 08540, U. S. A, 1984. 279*, 1984.
- [3] E. Beşteş, « Powder metallurgy processes and making metal powder », 2020. DOI: 10.13140/RG.2.2.21469.84967.
- [4] A. Ünal, « Production of rapidly solidified aluminium alloy powders by gas atomisation and their applications », *Powder metallurgy*, vol. 33, no. 1, pp. 53–64, 1990.
- [5] H. Liu and M. Altan, « Science and Engineering of Droplets: Fundamentals and Applications », *Applied Mechanics Reviews*, vol. 55, no. 1, B16–B17, Jan. 2002, ISSN: 0003-6900, 2379-0407. DOI: 10.1115/1.1445335.
- [6] H. Franz, L. Plochl and F.-P. Schimansky, « Recent advances of titanium alloy powder production by ceramic-free inert gas atomization », in *Proceedings of the 24th Annual International Titanium Association Conference Titanium*, 2008.
- [7] M. A. Smirnov, M. A. Kaplan and M. A. Sevostyanov, « Receiving finely divided metal powder by inert gas atomization », *IOP Conference Series: Materials Science and Engineering*, vol. 347, p. 012033, Apr. 2018, ISSN: 1757-8981, 1757-899X. DOI: 10.1088/1757-899X/347/1/012033.
- [8] J. Xie, Y. Zhao and J. Dunkley, « Effects of processing conditions on powder particle size and morphology in centrifugal atomisation of tin », *Powder Metallurgy*, vol. 47, no. 2, pp. 168–172, Mar. 2004, ISSN: 0032-5899, 1743-2901. DOI: 10.1179/003258904225015482.
- [9] B. Champagne *et al.*, « Fabrication of powders by the rotating electrode process », *International journal of powder metallurgy*, vol. 16, 1980.
- [10] M. Zdujić and D. Uskoković, « Production of atomized metal and alloy powders by the rotating electrode process », *Soviet Powder Metallurgy and Metal Ceramics*, vol. 29, no. 9, pp. 673–683, Sep. 1990, ISSN: 0038-5735, 1573-9066. DOI: 10.1007/BF00795571.
- [11] Y. Millet, « Fabrication de poudres métalliques par la méthode PREP », *Editions TI/ Techniques de l'Ingénieur*, 2015.
- [12] P. Roberts and P. Loewenstein, « Titanium alloy powders made by the rotating electrode process », *TMS/AIME*, pp. 21–35, 1980.

- [13] D. B. Wallace, « Capillary instability of a jet of liquid metal », *Journal of Fluids Engineering*, vol. 115, no. 3, pp. 529–532, Sep. 1993, ISSN: 0098-2202, 1528-901X. DOI: 10.1115/1.2910172.
- [14] C. R. Clark, B. Muntifering and J.-F. Jue, « Production and characterization of atomized u-Mo powder by the rotating electrode process », Idaho National Laboratory (INL), Tech. Rep., 2007.
- [15] R. Schenk, « REP atomizer engineering and UMo fuel-powder fabrication », PhD Thesis, Technische Universität München, 2016.
- [16] B. Ravry, « Development of an atomizer pilot for powder manufacturing used in nuclear research reactor, » PhD Thesis, Université de Bourgogne-Framatome CERCA, in preparation, 2021.
- [17] N. Ashgriz, Ed., *Handbook of Atomization and Sprays*. Boston, MA: Springer US, 2011. DOI: 10.1007/978-1-4419-7264-4.
- [18] L. Rayleigh, « On the instability of jets », *Proceedings of the London Mathematical Society*, vol. s1-10, no. 1, pp. 4–13, Nov. 1878, ISSN: 00246115. DOI: 10.1112/plms/s1-10.1.4.
- [19] L. Rayleigh, « On the stability, or instability, of certain fluid motions », *Proceedings of the London Mathematical Society*, vol. 1, no. 1, pp. 57–72, 1879.
- [20] C. Weber, « Zum Zerfall eines Flüssigkeitsstrahles », *ZAMM-Journal of Applied Mathematics and Mechanics/Zeitschrift für Angewandte Mathematik und Mechanik*, vol. 11, no. 2, pp. 136–154, 1931.
- [21] J. Hinze and H. Milborn, « Atomization of liquids by means of a rotating cup », *Journal of Applied Mechanics-Transactions of the ASME*, vol. 17, no. 2, pp. 145–153, 1950.
- [22] R. Fraser, N. Dombrowski and J. Routley, « The filming of liquids by spinning cups », *Chemical Engineering Science*, vol. 18, no. 11, p. 728, Nov. 1963, ISSN: 00092509. DOI: 10.1016/0009-2509(63)85054-X.
- [23] D. J. Bodkin, P. W. Sutcliffe, P. G. Mardon and L. E. Russell, « Centrifugal shot casting: A new atomization process for the preparation of high purity alloy powders », *Powder Metallurgy*, vol. 16, no. 32, pp. 277–313, Sep. 1973, ISSN: 0032-5899, 1743-2901. DOI: 10.1179/pom.1973.16.32.008.
- [24] E. Teunou and D. Poncelet, « Rotary disc atomisation for microencapsulation applications—prediction of the particle trajectories », *Journal of Food Engineering*, vol. 71, no. 4, pp. 345–353, Dec. 2005, ISSN: 02608774. DOI: 10.1016/j.jfoodeng.2004.10.048.
- [25] B. Champagne and R. Angers, « Size distribution of powders atomized by the rotating electrode process », *Modern Development in Powder Metallurgy*, vol. 12, pp. 83–104, 1981.
- [26] C. Labrecque, R. Angers, R. Tremblay and D. Dubé, « Inverted disk centrifugal atomization of AZ91 magnesium alloy », *Canadian Metallurgical Quarterly*, vol. 36, no. 3, pp. 169–175, Jul. 1997, ISSN: 0008-4433, 1879-1395. DOI: 10.1179/cmqr.1997.36.3.169.

- 
- [27] J.-P. Leteurtois, « Dispersion fine d'un liquide à l'aide d'un disque en rotation », PhD Thesis, 1974.
- [28] W. Walton and W. Prewett, « The production of sprays and mists of uniform drop size by means of spinning disc type sprayers », *Proceedings of the Physical Society. Section B*, vol. 62, no. 6, p. 341, 1949.
- [29] S. Matsumoto, K. Saito and Y. Takashima, « Phenomenal transition of liquid atomization from disk », *Journal of Chemical Engineering of Japan*, vol. 7, no. 1, pp. 13–19, 1974.
- [30] C.-K. Kim, J.-M. Park and H.-J. Ryu, « Use of a centrifugal atomization in the development of research reactor fuel », *Nuclear Engineering and Technology*, vol. 39, no. 5, pp. 617–626, Oct. 2007, ISSN: 1738-5733. DOI: 10.5516/NET.2007.39.5.617.
- [31] J. Rest, Y. S. Kim, G. L. Hofman, M. K. Meyer and S. L. Hayes, « U-Mo fuels handbook. Version 1.0 », Argonne National Lab.(ANL), Argonne, IL (United States), Tech. Rep., 2006.
- [32] K. C. Mills, *Recommended Values of Thermophysical Properties for Selected Commercial Alloys*. Woodhead Publishing Limited, 2002, ISBN: 978-1-85573-569-9. DOI: 10.1533/9781845690144.
- [33] J. Cahill and A. Kirshenbaum, « The surface tension of liquid uranium from its melting point, 1406 k to 1850 k », *Journal of Inorganic and Nuclear Chemistry*, vol. 27, no. 1, pp. 73–76, 1965.
- [34] P.-F. Paradis, T. Ishikawa and N. Koike, « Non-contact measurements of the surface tension and viscosity of molybdenum using an electrostatic levitation furnace », *International Journal of Refractory Metals and Hard Materials*, vol. 25, no. 1, pp. 95–100, Jan. 2007, ISSN: 02634368. DOI: 10.1016/j.ijrmhm.2006.02.001.
- [35] V. Bobkov, L. Fokin, E. Petrov, V. Popov, V. Rumiantsev and A. Savvatimsky, « Thermophysical properties of materials for nuclear engineering: A tutorial and collection of data », IAEA, Vienna, 2008.
- [36] D. Ofte, « The viscosities of liquid uranium, gold and lead », *Journal of nuclear materials*, vol. 22, no. 1, pp. 28–32, 1967.
- [37] C. Heinzen, A. Berger and I. Marison, « Use of vibration technology for jet break-up for encapsulation of cells and liquids in monodisperse microcapsules », in *Fundamentals of Cell Immobilisation Biotechnology*, M. Hofman, J. Anné, V. Nedović, R. Willaert, V. Nedović and R. Willaert, Eds., vol. 8A, Dordrecht: Springer Netherlands, 2004, pp. 257–275, ISBN: 978-90-481-6534-6 978-94-017-1638-3. DOI: 10.1007/978-94-017-1638-3\_14.
- [38] J. Chicheportiche, J. Zainoun, J. Renaudeaux, M. Jenger and G. Liu, « A new vibro-rotating spray generator », *ReT 1000.10000*, 2011.
- [39] H. Deng and H. Ouyang, « Vibration of spinning discs and powder formation in centrifugal atomization », *Proceedings of the Royal Society A: Mathematical, Physical and Engineering Sciences*, vol. 467, no. 2126, pp. 361–380, Feb. 2011, ISSN: 1364-5021, 1471-2946. DOI: 10.1098/rspa.2010.0099.
- [40] S. Martin, « Contribution à la modélisation du frittage en phase solide », PhD Thesis, Université de Technologie de Compiègne, 2014.
-

- [41] G. Qiu, S. Henke and J. Grabe, « Application of a Coupled Eulerian–Lagrangian approach on geomechanical problems involving large deformations », *Computers and Geotechnics*, vol. 38, no. 1, pp. 30–39, Jan. 2011, ISSN: 0266352X. DOI: 10.1016/j.compgeo.2010.09.002.
- [42] H. U. Mair, « Review: Hydrocodes for structural response to underwater explosions », *Shock and Vibration*, vol. 6, no. 2, pp. 81–96, 1999, ISSN: 1070-9622, 1875-9203. DOI: 10.1155/1999/587105.
- [43] C. W. Hirt, A. A. Amsden and J. Cook, « An arbitrary Lagrangian-Eulerian computing method for all flow speeds », *Journal of computational physics*, vol. 14, no. 3, pp. 227–253, 1974.
- [44] W. F. Noh and P. Woodward, « SLIC (simple line interface calculation) », in *Proceedings of the fifth international conference on numerical methods in fluid dynamics June 28–July 2, 1976 Twente University, Enschede*, Springer, 1976, pp. 330–340.
- [45] C. W. Hirt and B. D. Nichols, « Volume of fluid (VOF) method for the dynamics of free boundaries », *Journal of computational physics*, vol. 39, no. 1, pp. 201–225, 1981.
- [46] S. Osher and J. A. Sethian, « Fronts propagating with curvature-dependent speed: Algorithms based on Hamilton-Jacobi formulations », *Journal of computational physics*, vol. 79, no. 1, pp. 12–49, 1988.
- [47] S. Popinet, « An accurate adaptive solver for surface-tension-driven interfacial flows », *Journal of Computational Physics*, vol. 228, no. 16, pp. 5838–5866, Sep. 2009, ISSN: 00219991. DOI: 10.1016/j.jcp.2009.04.042.
- [48] R. A. Gingold and J. J. Monaghan, « Smoothed Particle Hydrodynamics: Theory and application to non-spherical stars », *Monthly Notices of the Royal Astronomical Society*, vol. 181, no. 3, pp. 375–389, Dec. 1977, ISSN: 0035-8711, 1365-2966. DOI: 10.1093/mnras/181.3.375.
- [49] L. B. Lucy, « A numerical approach to the testing of the fission hypothesis », *The Astronomical Journal*, vol. 82, p. 1013, Dec. 1977, ISSN: 00046256. DOI: 10.1086/112164.
- [50] W. K. Liu, S. Jun and Y. F. Zhang, « Reproducing Kernel Particle methods », *International Journal for Numerical Methods in Fluids*, vol. 20, no. 8-9, pp. 1081–1106, Apr. 1995, ISSN: 0271-2091, 1097-0363. DOI: 10.1002/flid.1650200824.
- [51] B. Nayroles, G. Touzot and P. Villon, « Generalizing the finite element method: Diffuse approximation and diffuse elements », *Computational Mechanics*, vol. 10, no. 5, pp. 307–318, 1992, ISSN: 0178-7675, 1432-0924. DOI: 10.1007/BF00364252.
- [52] T. Belytschko, Y. Y. Lu and L. Gu, « Element-free Galerkin methods », *International Journal for Numerical Methods in Engineering*, vol. 37, no. 2, pp. 229–256, Jan. 1994, ISSN: 0029-5981, 1097-0207. DOI: 10.1002/nme.1620370205.
- [53] G. R. Liu and Y. T. Gu, « A Point Interpolation method for two-dimensional solids », *International Journal for Numerical Methods in Engineering*, vol. 50, no. 4, pp. 937–951, Feb. 2001, ISSN: 0029-5981, 1097-0207. DOI: 10.1002/1097-0207(20010210)50:4<937::AID-NME62>3.0.CO;2-X.

- 
- [54] G. R. Liu and G. Y. Zhang, « Edge-based Smoothed Point Interpolation Methods », *International Journal of Computational Methods*, vol. 05, no. 04, pp. 621–646, Dec. 2008, ISSN: 0219-8762, 1793-6969. DOI: 10.1142/S0219876208001662.
- [55] G. R. Liu, *Meshfree Methods: Moving beyond the finite element method, second edition*. Place of publication not identified: CRC Press, 2018, OCLC: 1102794283, ISBN: 978-1-138-37270-2.
- [56] M. Ellero, M. Kröger and S. Hess, « Viscoelastic flows studied by smoothed particle dynamics », *Journal of Non-Newtonian Fluid Mechanics*, vol. 105, no. 1, pp. 35–51, Jul. 2002, ISSN: 03770257. DOI: 10.1016/S0377-0257(02)00059-9.
- [57] Y. Sakai and A. Yamasita, « Elastic-Plastic large deformation analysis using SPH », in *Computational Methods*, G. Liu, V. Tan and X. Han, Eds., Dordrecht: Springer Netherlands, 2006, pp. 1515–1519, ISBN: 978-1-4020-3952-2. DOI: 10.1007/978-1-4020-3953-9\_77.
- [58] D. J. Price, « Smoothed Particle Magnetohydrodynamics - IV. Using the vector potential », *Monthly Notices of the Royal Astronomical Society*, vol. 401, no. 3, pp. 1475–1499, Jan. 2010, ISSN: 00358711, 13652966. DOI: 10.1111/j.1365-2966.2009.15763.x.
- [59] F. A. Stasyszyn and D. Elstner, « A vector potential implementation for Smoothed Particle Magnetohydrodynamics », *Journal of Computational Physics*, vol. 282, pp. 148–156, Feb. 2015, ISSN: 00219991. DOI: 10.1016/j.jcp.2014.11.011.
- [60] X. Hu and N. Adams, « A multi-phase SPH method for macroscopic and mesoscopic flows », *Journal of Computational Physics*, vol. 213, no. 2, pp. 844–861, Apr. 2006, ISSN: 00219991. DOI: 10.1016/j.jcp.2005.09.001.
- [61] N. Grenier, M. Antuono, A. Colagrossi, D. Le Touzé and B. Alessandrini, « An Hamiltonian interface SPH formulation for multi-fluid and free surface flows », *Journal of Computational Physics*, vol. 228, no. 22, pp. 8380–8393, Dec. 2009, ISSN: 00219991. DOI: 10.1016/j.jcp.2009.08.009.
- [62] J. J. Monaghan and A. Rafiee, « A simple SPH algorithm for multi-fluid flow with high density ratios », *International Journal for Numerical Methods in Fluids*, vol. 71, no. 5, pp. 537–561, Feb. 2013, ISSN: 02712091. DOI: 10.1002/flid.3671.
- [63] S. Adami, « Modeling and simulation of multiphase phenomena with Smoothed Particle Hydrodynamics », PhD Thesis, Technische Universität München, 2014.
- [64] D. Violeau and R. Issa, « Numerical modelling of complex turbulent free-surface flows with the SPH method: An overview », *International Journal for Numerical Methods in Fluids*, vol. 53, no. 2, pp. 277–304, Jan. 2007, ISSN: 02712091, 10970363. DOI: 10.1002/flid.1292.
- [65] J. J. Monaghan, « A turbulence model for Smoothed Particle Hydrodynamics », *European Journal of Mechanics-B/Fluids*, vol. 30, no. 4, pp. 360–370, 2011.
- [66] E. Kazemi, K. Koll, S. Tait and S. Shao, « SPH modelling of turbulent open channel flow over and within natural gravel beds with rough interfacial boundaries », *Advances in Water Resources*, vol. 140, p. 103 557, Jun. 2020, ISSN: 03091708. DOI: 10.1016/j.advwatres.2020.103557.
-

- [67] J. Monaghan, « Simulating free surface flows with SPH », *Journal of Computational Physics*, vol. 110, no. 2, pp. 399–406, Feb. 1994, ISSN: 00219991. DOI: 10.1006/jcph.1994.1034.
- [68] A. Colagrossi, « A meshless Lagrangian method for free-surface and interface flows with fragmentation », PhD Thesis, Universita di Roma, 2005.
- [69] R. Dalrymple and B. Rogers, « Numerical modeling of water waves with the SPH method », *Coastal Engineering*, vol. 53, no. 2-3, pp. 141–147, Feb. 2006, ISSN: 03783839. DOI: 10.1016/j.coastaleng.2005.10.004.
- [70] X. Xu, « An improved SPH approach for simulating 3D dam-break flows with breaking waves », *Computer Methods in Applied Mechanics and Engineering*, vol. 311, pp. 723–742, Nov. 2016, ISSN: 00457825. DOI: 10.1016/j.cma.2016.09.002.
- [71] A. Mahdavi and N. Shahkarami, « SPH analysis of free surface flow over Pivot Weirs », *KSCCE Journal of Civil Engineering*, vol. 24, no. 4, pp. 1183–1194, Apr. 2020, ISSN: 1226-7988, 1976-3808. DOI: 10.1007/s12205-020-0095-1.
- [72] P. Cleary, M. Prakash and J. Ha, « Novel applications of smoothed particle hydrodynamics (SPH) in metal forming », *Journal of Materials Processing Technology*, vol. 177, no. 1-3, pp. 41–48, Jul. 2006, ISSN: 09240136. DOI: 10.1016/j.jmatprotec.2006.03.237.
- [73] R. Koch, S. Braun, L. Wieth, G. Chaussonnet, T. Dauch and H.-J. Bauer, « Prediction of primary atomization using Smoothed Particle Hydrodynamics », *European Journal of Mechanics-B/Fluids*, vol. 61, pp. 271–278, 2017.
- [74] T. Takashima, T. Ito, M. Shigeta, S. Izawa and Y. Fukunishi, « Simulation of liquid jet breakup process by three-dimensional incompressible SPH method », in *Proceeding of 7th International Conference on Computer Fluid Dynamics (ICCFD7)*, 2012, pp. 9–13.
- [75] F. V. Sirotkin and J. J. Yoh, « A new particle method for simulating breakup of liquid jets », *Journal of Computational Physics*, vol. 231, no. 4, pp. 1650–1674, Feb. 2012, ISSN: 00219991. DOI: 10.1016/j.jcp.2011.10.020.
- [76] Q. Yang, F. Xu, Y. Yang and L. Wang, « A multi-phase SPH model based on Riemann solvers for simulation of jet breakup », *Engineering Analysis with Boundary Elements*, vol. 111, pp. 134–147, Feb. 2020, ISSN: 09557997. DOI: 10.1016/j.enganabound.2019.10.015.
- [77] F. Caleyron, « Simulation numérique par la méthode SPH de fuites de fluide consécutives à la déchirure d’un réservoir sous impact », PhD Thesis, INSA de Lyon, 2011.
- [78] M. R. R. M. A. Zainol, M. A. Kamaruddin, M. H. Zawawi and K. A. Wahab, « Numerical analysis study of Sarawak barrage river bed erosion and scouring by using Smooth Particle Hydrodynamic (SPH) », *IOP Conference Series: Materials Science and Engineering*, vol. 267, p. 012010, Nov. 2017, ISSN: 1757-8981, 1757-899X. DOI: 10.1088/1757-899X/267/1/012010.
- [79] D. A. Fulk and D. W. Quinn, « An analysis of 1-d Smoothed Particle Hydrodynamics Kernels », *Journal of Computational Physics*, vol. 126, no. 1, pp. 165–180, Jun. 1996, ISSN: 00219991. DOI: 10.1006/jcph.1996.0128.



- 
- [80] I. J. Schoenberg, « Contributions to the problem of approximation of equidistant data by analytic functions. Part a. On the problem of smoothing or graduation. a first class of analytic approximation formulae », *Quarterly of Applied Mathematics*, vol. 4, no. 1, pp. 45–99, Apr. 1946, ISSN: 0033-569X, 1552-4485. DOI: 10.1090/qam/15914.
- [81] J. Swegle, D. Hicks and S. Attaway, « Smoothed Particle Hydrodynamics stability analysis », *Journal of Computational Physics*, vol. 116, no. 1, pp. 123–134, Jan. 1995, ISSN: 00219991. DOI: 10.1006/jcph.1995.1010.
- [82] W. Dehnen and H. Aly, « Improving convergence in Smoothed Particle Hydrodynamics simulations without pairing instability: SPH without pairing instability », *Monthly Notices of the Royal Astronomical Society*, vol. 425, no. 2, pp. 1068–1082, Sep. 2012, ISSN: 00358711. DOI: 10.1111/j.1365-2966.2012.21439.x.
- [83] J. J. Monaghan, « Smoothed Particle Hydrodynamics », *Reports on Progress in Physics*, vol. 68, no. 8, pp. 1703–1759, Aug. 2005, ISSN: 0034-4885, 1361-6633. DOI: 10.1088/0034-4885/68/8/R01.
- [84] G. R. Liu and M. B. Liu, *Smoothed Particle Hydrodynamics - A Meshfree Particle Method*. World Scientific Publishing Co. Pte. Ltd., 2003, ISBN: 978-981-256-440-5. DOI: 10.1142/9789812564405.
- [85] X. Hu and N. Adams, « An incompressible multi-phase SPH method », *Journal of Computational Physics*, vol. 227, no. 1, pp. 264–278, Nov. 2007, ISSN: 00219991. DOI: 10.1016/j.jcp.2007.07.013.
- [86] S. Shao and E. Y. Lo, « Incompressible SPH method for simulating Newtonian and non-Newtonian flows with a free surface », *Advances in Water Resources*, vol. 26, no. 7, pp. 787–800, Jul. 2003, ISSN: 03091708. DOI: 10.1016/S0309-1708(03)00030-7.
- [87] J. P. Morris, P. J. Fox and Y. Zhu, « Modeling low Reynolds number incompressible flows Using SPH », *Journal of Computational Physics*, vol. 136, no. 1, pp. 214–226, Sep. 1997, ISSN: 00219991. DOI: 10.1006/jcph.1997.5776.
- [88] J. P. Morris, « Simulating surface tension with Smoothed Particle Hydrodynamics », *International Journal for Numerical Methods in Fluids*, vol. 33, no. 3, pp. 333–353, Jun. 2000, ISSN: 0271-2091, 1097-0363. DOI: 10.1002/1097-0363(20000615)33:3<333::AID-FLD11>3.0.CO;2-7.
- [89] A. Colagrossi and M. Landrini, « Numerical simulation of interfacial flows by Smoothed Particle Hydrodynamics », *Journal of Computational Physics*, vol. 191, no. 2, pp. 448–475, Nov. 2003, ISSN: 00219991. DOI: 10.1016/S0021-9991(03)00324-3.
- [90] S. Adami, X. Hu and N. Adams, « A generalized wall boundary condition for Smoothed Particle Hydrodynamics », *Journal of Computational Physics*, vol. 231, no. 21, pp. 7057–7075, Aug. 2012, ISSN: 00219991. DOI: 10.1016/j.jcp.2012.05.005.

- [91] M. Ferrand, D. R. Laurence, B. D. Rogers, D. Violeau and C. Kassiotis, « Unified semi-analytical wall boundary conditions for inviscid, laminar or turbulent flows in the meshless SPH method: Unified wall boundary conditions in SPH », en, *International Journal for Numerical Methods in Fluids*, vol. 71, no. 4, pp. 446–472, Feb. 2013, ISSN: 02712091. DOI: 10.1002/flid.3666.
- [92] Y. Tang, S. Chen and Q. Jiang, « A conservative SPH scheme using exact projection with semi-analytical boundary method for free-surface flows », *Applied Mathematical Modelling*, vol. 82, pp. 607–635, Jun. 2020, ISSN: 0307904X. DOI: 10.1016/j.apm.2020.01.073.
- [93] X. Xu and P. Yu, « A technique to remove the tensile instability in weakly compressible SPH », *Computational Mechanics*, vol. 62, no. 5, pp. 963–990, Nov. 2018, ISSN: 0178-7675, 1432-0924. DOI: 10.1007/s00466-018-1542-4.
- [94] S. Lind, R. Xu, P. Stansby and B. Rogers, « Incompressible Smoothed Particle Hydrodynamics for free-surface flows: A generalised diffusion-based algorithm for stability and validations for impulsive flows and propagating waves », *Journal of Computational Physics*, vol. 231, no. 4, pp. 1499–1523, Feb. 2012, ISSN: 00219991. DOI: 10.1016/j.jcp.2011.10.027.
- [95] A. Tartakovsky and P. Meakin, « Modeling of surface tension and contact angles with Smoothed Particle Hydrodynamics », *Physical Review E*, vol. 72, no. 2, Aug. 2005, ISSN: 1539-3755, 1550-2376. DOI: 10.1103/PhysRevE.72.026301.
- [96] J. Kordilla, A. Tartakovsky and T. Geyer, « A Smoothed Particle Hydrodynamics model for droplet and film flow on smooth and rough fracture surfaces », *Advances in Water Resources*, vol. 59, pp. 1–14, Sep. 2013, ISSN: 03091708. DOI: 10.1016/j.advwatres.2013.04.009.
- [97] A. M. Aly, M. Asai and Y. Sonda, « Modelling of surface tension force for free surface flows in ISPH method », *International Journal of Numerical Methods for Heat and Fluid Flow*, vol. 23, no. 3, pp. 479–498, Apr. 2013, ISSN: 0961-5539. DOI: 10.1108/09615531311301263.
- [98] M. B. Liu and G. R. Liu, « Smoothed Particle Hydrodynamics (SPH): An overview and recent developments », *Archives of Computational Methods in Engineering*, vol. 17, no. 1, pp. 25–76, Mar. 2010, ISSN: 1134-3060, 1886-1784. DOI: 10.1007/s11831-010-9040-7.
- [99] Z.-B. Wang, R. Chen, H. Wang, Q. Liao, X. Zhu and S.-Z. Li, « An overview of Smoothed Particle Hydrodynamics for simulating multiphase flow », *Applied Mathematical Modelling*, vol. 40, no. 23-24, pp. 9625–9655, Dec. 2016, ISSN: 0307904X. DOI: 10.1016/j.apm.2016.06.030.
- [100] M. Russell, A. Souto-Iglesias and T. Zohdi, « Numerical simulation of laser fusion additive manufacturing processes using the SPH method », *Computer Methods in Applied Mechanics and Engineering*, vol. 341, pp. 163–187, Nov. 2018, ISSN: 00457825. DOI: 10.1016/j.cma.2018.06.033.
- [101] J. Brackbill, D. Kothe and C. Zemach, « A continuum method for modeling surface tension », *Journal of Computational Physics*, vol. 100, no. 2, pp. 335–354, Jun. 1992, ISSN: 00219991. DOI: 10.1016/0021-9991(92)90240-Y.

- 
- [102] S. Adami, X. Hu and N. Adams, « A new surface-tension formulation for multi-phase SPH using a reproducing divergence approximation », *Journal of Computational Physics*, vol. 229, no. 13, pp. 5011–5021, Jul. 2010, ISSN: 00219991. DOI: 10.1016/j.jcp.2010.03.022.
- [103] H. Qiang, F. Chen and W. Gao, « Modified algorithm for surface tension with smoothed particle hydrodynamics and its applications », *Computer Modeling in Engineering and Sciences*, vol. 77, no. 3, p. 239, 2011.
- [104] J. K. Chen, J. E. Beraun and T. C. Carney, « A corrective Smoothed Particle method for boundary value problems in heat conduction », *International Journal for Numerical Methods in Engineering*, vol. 46, no. 2, pp. 231–252, Sep. 1999, ISSN: 0029-5981, 1097-0207. DOI: 10.1002/(SICI)1097-0207(19990920)46:2<231::AID-NME672>3.0.CO;2-K.
- [105] B. Lafaurie, C. Nardone, R. Scardovelli, S. Zaleski and G. Zanetti, « Modelling merging and fragmentation in multiphase flows with SURFER », *Journal of Computational Physics*, vol. 113, no. 1, pp. 134–147, Jul. 1994, ISSN: 00219991. DOI: 10.1006/jcph.1994.1123.
- [106] L. Yang, M. Rakhsha and D. Negrut, « Comparison of surface tension models in Smoothed Particles Hydrodynamics method », in *Volume 6: 15th International Conference on Multibody Systems, Nonlinear Dynamics, and Control*, Anaheim, California, USA: American Society of Mechanical Engineers, Aug. 2019, ISBN: 978-0-7918-5926-1. DOI: 10.1115/DETC2019-98124.
- [107] E. Arai, A. Tartakovsky, R. G. Holt, S. Grace and E. Ryan, « Comparison of surface tension generation methods in Smoothed Particle Hydrodynamics for dynamic systems », *Computers and Fluids*, vol. 203, p. 104540, May 2020, ISSN: 00457930. DOI: 10.1016/j.compfluid.2020.104540.
- [108] M. Gomez-Gesteira, B. D. Rogers, R. A. Dalrymple and A. J. Crespo, « State-of-the-art of classical SPH for free-surface flows », *Journal of Hydraulic Research*, vol. 48, no. sup1, pp. 6–27, Jan. 2010, ISSN: 0022-1686, 1814-2079. DOI: 10.1080/00221686.2010.9641242.
- [109] D. Violeau and B. D. Rogers, « Smoothed particle hydrodynamics (SPH) for free-surface flows: Past, present and future », *Journal of Hydraulic Research*, vol. 54, no. 1, pp. 1–26, Jan. 2016, ISSN: 0022-1686, 1814-2079. DOI: 10.1080/00221686.2015.1119209.
- [110] J. Bonet and T.-S. Lok, « Variational and momentum preservation aspects of Smooth Particle Hydrodynamic formulations », *Computer Methods in Applied Mechanics and Engineering*, vol. 180, no. 1-2, pp. 97–115, Nov. 1999, ISSN: 00457825. DOI: 10.1016/S0045-7825(99)00051-1.
- [111] M. Ordoubadi, M. Yaghoubi and F. Yeganehdoust, « Surface tension simulation of free surface flows using Smoothed Particle Hydrodynamics », *Scientia Iranica*, vol. 24, no. 4, pp. 2019–2033, Aug. 2017, ISSN: 2345-3605. DOI: 10.24200/sci.2017.4291.
-

- [112] N. N. Ehigiamusoe, S. Maxutov and Y. C. Lee, « Modeling surface tension of a two-dimensional droplet using Smoothed Particle Hydrodynamics: Modeling surface tension of a two-dimensional droplet using SPH », *International Journal for Numerical Methods in Fluids*, vol. 88, no. 7, pp. 334–346, Nov. 2018, ISSN: 02712091. DOI: 10.1002/flid.4663.
- [113] J.-P. Fürstenau, C. Weikenfels and P. Wriggers, « Free surface tension in incompressible Smoothed Particle Hydrodynamics (ISPH) », *Computational Mechanics*, vol. 65, no. 2, pp. 487–502, Feb. 2020, ISSN: 0178-7675, 1432-0924. DOI: 10.1007/s00466-019-01780-6.
- [114] M. Zhang, « Simulation of surface tension in 2D and 3D with Smoothed Particle Hydrodynamics method », *Journal of Computational Physics*, vol. 229, no. 19, pp. 7238–7259, Sep. 2010, ISSN: 00219991. DOI: 10.1016/j.jcp.2010.06.010.
- [115] A. Barecasco, H. Terissa and C. F. Naa, « Simple free-surface detection in two and three-dimensional SPH solver », *arXiv:1309.4290 [physics]*, Sep. 2013, arXiv: 1309.4290.
- [116] H. Terissa, A. Barecasco and C. F. Naa, « Three-dimensional Smoothed Particle Hydrodynamics simulation for liquid droplet with surface tension », *arXiv:1309.3868 [physics]*, Sep. 2013, arXiv: 1309.3868.
- [117] M. Yang, X. Li, G. Yang and E. Wu, « SPH-based Fluid Simulation with a New Surface Tension Formulation », in *2015 International Conference on Virtual Reality and Visualization (ICVRV)*, Xiamen: IEEE, Oct. 2015, pp. 295–300, ISBN: 978-1-4673-7673-0. DOI: 10.1109/ICVRV.2015.34.
- [118] G. A. Dilts, « Moving least-squares particle hydrodynamics II: Conservation and boundaries », *International Journal for Numerical Methods in Engineering*, vol. 48, no. 10, pp. 1503–1524, Aug. 2000, ISSN: 0029-5981, 1097-0207. DOI: 10.1002/1097-0207(20000810)48:10<1503::AID-NME832>3.0.CO;2-D.
- [119] T. Belytschko, Y. Krongauz, J. Dolbow and C. Gerlach, « On the completeness of meshfree particle methods », *International Journal for Numerical Methods in Engineering*, vol. 43, no. 5, pp. 785–819, Nov. 1998, ISSN: 0029-5981, 1097-0207. DOI: 10.1002/(SICI)1097-0207(19981115)43:5<785::AID-NME420>3.0.CO;2-9.
- [120] S. Sibilla, « SPH simulation of local scour processes », *SPHERIC-Smoothed Particle Hydrodynamics European Research Interest Community*, p. 169, Jan. 2007.
- [121] J. Shao, H. Li, G. Liu and M. Liu, « An improved SPH method for modeling liquid sloshing dynamics », *Computers & Structures*, vol. 100-101, pp. 18–26, Jun. 2012, ISSN: 00457949. DOI: 10.1016/j.compstruc.2012.02.005.
- [122] Z. Zhang and M. Liu, « Smoothed Particle Hydrodynamics with kernel gradient correction for modeling high velocity impact in two- and three-dimensional spaces », *Engineering Analysis with Boundary Elements*, vol. 83, pp. 141–157, Oct. 2017, ISSN: 09557997. DOI: 10.1016/j.enganabound.2017.07.015.
- [123] D. Molteni and A. Colagrossi, « A simple procedure to improve the pressure evaluation in hydrodynamic context using the SPH », *Computer Physics Communications*, vol. 180, no. 6, pp. 861–872, Jun. 2009, ISSN: 00104655. DOI: 10.1016/j.cpc.2008.12.004.

- 
- [124] H.-D. Seo, H.-J. Park, J.-I. Kim and P. S. Lee, « The particle-attached element interpolation for density correction in Smoothed Particle Hydrodynamics », *Advances in Engineering Software*, vol. 154, p. 102972, Apr. 2021, ISSN: 09659978. DOI: 10.1016/j.advengsoft.2021.102972.
- [125] J. Calderon-Sanchez, J. Cercos-Pita and D. Duque, « A geometric formulation of the Shepard renormalization factor », *Computers & Fluids*, vol. 183, pp. 16–27, Apr. 2019, ISSN: 00457930. DOI: 10.1016/j.compfluid.2019.02.020.
- [126] W. Kostorz and A. Esmail-Yakas, « A semi-analytical boundary integral method for radial functions with application to Smoothed Particle Hydrodynamics », *Journal of Computational Physics*, vol. 417, p. 109565, Sep. 2020, ISSN: 00219991. DOI: 10.1016/j.jcp.2020.109565.
- [127] M. Herant, « Dirty tricks for SPH », *Memorie della Societa Astronomica Italiana*, vol. 65, p. 1013, 1994.
- [128] H. A. T. Vanhala and A. G. W. Cameron, « Numerical simulations of triggered star formation. i. Collapse of dense molecular cloud cores », *The Astrophysical Journal*, vol. 508, no. 1, pp. 291–307, Nov. 1998, ISSN: 0004-637X, 1538-4357. DOI: 10.1086/306396.
- [129] P. Incardona, A. Leo, Y. Zaluzhnyi, R. Ramaswamy and I. F. Sbalzarini, « OpenFPM: A scalable open framework for particle and particle-mesh codes on parallel computers », *Computer Physics Communications*, vol. 241, pp. 155–177, Aug. 2019, ISSN: 00104655. DOI: 10.1016/j.cpc.2019.03.007.
- [130] S. Geara, S. Martin, S. Adami, W. Petry, J. Allenou, B. Stepanik and O. Bonnefoy, « A new SPH density formulation for 3D free-surface flows », en, *Computers & Fluids*, vol. 232, p. 105193, Jan. 2022, ISSN: 00457930. DOI: 10.1016/j.compfluid.2021.105193.
- [131] M. Dai and D. P. Schmidt, « Adaptive tetrahedral meshing in free-surface flow », *Journal of Computational Physics*, vol. 208, no. 1, pp. 228–252, Sep. 2005, ISSN: 00219991. DOI: 10.1016/j.jcp.2005.02.012.
- [132] M. Olejnik and K. Szewc, « Smoothed Particle Hydrodynamics modelling of the Rayleigh-Plateau instability », *Journal of Theoretical and Applied Mechanics*, p. 675, Jul. 2018, ISSN: 1429-2955. DOI: 10.15632/jtam-pl.56.3.675.
- [133] E.-S. Lee, C. Moulinec, R. Xu, D. Violeau, D. Laurence and P. Stansby, « Comparisons of weakly compressible and truly incompressible algorithms for the SPH mesh free particle method », *Journal of Computational Physics*, vol. 227, no. 18, pp. 8417–8436, Sep. 2008, ISSN: 00219991. DOI: 10.1016/j.jcp.2008.06.005.
- [134] M. Lastiwka, M. Basa and N. J. Quinlan, « Permeable and non-reflecting boundary conditions in SPH », *International Journal for Numerical Methods in Fluids*, vol. 61, no. 7, pp. 709–724, Nov. 2009, ISSN: 02712091, 10970363. DOI: 10.1002/flid.1971.
- [135] I. Federico, S. Marrone, A. Colagrossi, F. Aristodemo and M. Antuono, « Simulating 2D open-channel flows through an SPH model », *European Journal of Mechanics - B/Fluids*, vol. 34, pp. 35–46, Jul. 2012, ISSN: 09977546. DOI: 10.1016/j.euromechflu.2012.02.002.
-

- [136] S. K. Tan, N.-S. Cheng, Y. Xie and S. Shao, « Incompressible SPH simulation of open channel flow over smooth bed », *Journal of Hydro-environment Research*, vol. 9, no. 3, pp. 340–353, Sep. 2015, ISSN: 15706443. DOI: 10.1016/j.jher.2014.12.006.
- [137] M. Hirschler, P. Kunz, M. Huber, F. Hahn and U. Niekem, « Open boundary conditions for ISPH and their application to micro-flow », *Journal of Computational Physics*, vol. 307, pp. 614–633, Feb. 2016, ISSN: 00219991. DOI: 10.1016/j.jcp.2015.12.024.
- [138] N. Zainoun, J. Chicheportiche and J. Renaudeaux, « Le vibro-générateur d'aérosols homogènes », in *Proceedings of the annual conference ASFERA*, 2004.
- [139] B. Bonhoeffer, A. Kwade and M. Juhnke, « Impact of formulation properties and process parameters on the dispensing and deposition of drug nanosuspensions using micro-valve technology », *Journal of Pharmaceutical Sciences*, vol. 106, no. 4, pp. 1102–1110, Apr. 2017, ISSN: 00223549. DOI: 10.1016/j.xphs.2016.12.019.
- [140] H. R. Brandenberger, « Immobilisierung von Biokatalysatoren in monodispersen Alginatpartikeln mittels einer Eindüsen- und Mehrdüsenanlage », PhD thesis, ETH Zurich, 1999. DOI: 10.3929/ETHZ-A-003823527.
- [141] M.-C. Yuen, « Non-linear capillary instability of a liquid jet », *Journal of Fluid Mechanics*, vol. 33, no. 1, pp. 151–163, Jul. 1968, ISSN: 0022-1120, 1469-7645. DOI: 10.1017/S0022112068002429.
- [142] D. Rutland and G. Jameson, « Theoretical prediction of the sizes of drops formed in the breakup of capillary jets », *Chemical Engineering Science*, vol. 25, no. 11, pp. 1689–1698, Nov. 1970, ISSN: 00092509. DOI: 10.1016/0009-2509(70)80060-4.
- [143] N. Ashgriz and F. Mashayek, « Temporal analysis of capillary jet breakup », *Journal of Fluid Mechanics*, vol. 291, pp. 163–190, May 1995, ISSN: 0022-1120, 1469-7645. DOI: 10.1017/S0022112095002667.
- [144] H. González and F. J. García, « The measurement of growth rates in capillary jets », *Journal of Fluid Mechanics*, vol. 619, pp. 179–212, Jan. 2009, ISSN: 0022-1120, 1469-7645. DOI: 10.1017/S0022112008004576.
- [145] Q. Lehua, J. Xiaoshan, L. Jun, H. Xianghui and L. Hejun, « Dominant factors of metal jet breakup in micro droplet deposition manufacturing technique », *Chinese Journal of Aeronautics*, vol. 23, no. 4, pp. 495–500, Aug. 2010, ISSN: 10009361. DOI: 10.1016/S1000-9361(09)60246-6.
- [146] T. Driessen, P. Sleutel, F. Dijkstra, R. Jeurissen and D. Lohse, « Control of jet breakup by a superposition of two Rayleigh–Plateau-unstable modes », *Journal of Fluid Mechanics*, vol. 749, pp. 275–296, Jun. 2014, ISSN: 0022-1120, 1469-7645. DOI: 10.1017/jfm.2014.178.
- [147] J. R. Richards, A. M. Lenhoff and A. N. Beris, « Dynamic breakup of liquid–liquid jets », *Physics of Fluids*, vol. 6, no. 8, pp. 2640–2655, Aug. 1994, ISSN: 1070-6631, 1089-7666. DOI: 10.1063/1.868154.
- [148] Y. Pan and K. Suga, « A numerical study on the breakup process of laminar liquid jets into a gas », *Physics of Fluids*, vol. 18, no. 5, p. 052101, May 2006, ISSN: 1070-6631, 1089-7666. DOI: 10.1063/1.2194936.

- 
- [149] J. Delteil, S. Vincent, A. Erriguible and P. Subra-Paternault, « Numerical investigations in Rayleigh breakup of round liquid jets with VOF methods », *Computers & Fluids*, vol. 50, no. 1, pp. 10–23, Nov. 2011, ISSN: 00457930. DOI: 10.1016/j.compfluid.2011.05.010.
- [150] X. Yang and A. Turan, « Simulation of liquid jet atomization coupled with forced perturbation », *Physics of Fluids*, vol. 29, no. 2, p. 022 103, Feb. 2017, ISSN: 1070-6631, 1089-7666. DOI: 10.1063/1.4976621.
- [151] C. Shen, F. Liu, L. Wu, C. Yu and W. Yu, « Dripping, jetting and regime transition of droplet formation in a buoyancy-assisted microfluidic device », *Micromachines*, vol. 11, no. 11, p. 962, Oct. 2020, ISSN: 2072-666X. DOI: 10.3390/mi11110962.
- [152] S. Saito, Y. Abe and K. Koyama, « Lattice Boltzmann modeling and simulation of liquid jet breakup », *Physical Review E*, vol. 96, no. 1, Jul. 2017, ISSN: 2470-0045, 2470-0053. DOI: 10.1103/PhysRevE.96.013317.
- [153] T. Ménard, S. Tanguy and A. Berlemont, « Coupling Level Set/VOF/Ghost Fluid methods: Validation and application to 3D simulation of the primary break-up of a liquid jet », *International Journal of Multiphase Flow*, vol. 33, no. 5, pp. 510–524, May 2007, ISSN: 03019322. DOI: 10.1016/j.ijmultiphaseflow.2006.11.001.
- [154] M. Pourabdian, P. Omidvar and M. R. Morad, « Multiphase simulation of liquid jet breakup using Smoothed Particle Hydrodynamics », *International Journal of Modern Physics C*, vol. 28, no. 04, p. 1750 054, Apr. 2017, ISSN: 0129-1831, 1793-6586. DOI: 10.1142/S0129183117500541.
- [155] A. Farrokhpahanah and J. Mostaghimi, « Application of multiphase particle methods in atomization and breakup regimes of liquid jets », in *Fluids Engineering Division Summer Meeting*, American Society of Mechanical Engineers, vol. 46216, 2014, V01AT05A009.
- [156] « Chapter 5 Wetting properties of metal/metal systems », in *Pergamon Materials Series*, vol. 3, Elsevier, 1999, pp. 175–197, ISBN: 978-0-08-042146-9. DOI: 10.1016/S1470-1804(99)80007-8.
- [157] N. Eustathopoulos, « Wetting by Liquid metals—Application in materials processing: The contribution of the Grenoble Group », *Metals*, vol. 5, no. 1, pp. 350–370, Mar. 2015, ISSN: 2075-4701. DOI: 10.3390/met5010350.
- [158] S. Mohammadi, « Nano-TiO<sub>2</sub> precipitation in SDRs: Experimental and modelling studies », PhD Thesis, Newcastle University, 2014.
- [159] T. Myers and J. Charpin, « The effect of the Coriolis force on axisymmetric rotating thin film flows », *International Journal of Non-Linear Mechanics*, vol. 36, no. 4, pp. 629–635, Jun. 2001, ISSN: 00207462. DOI: 10.1016/S0020-7462(00)00026-3.
- [160] T. Myers and M. Lombe, « The importance of the Coriolis force on axisymmetric horizontal rotating thin film flows », *Chemical Engineering and Processing: Process Intensification*, vol. 45, no. 2, pp. 90–98, Feb. 2006, ISSN: 02552701. DOI: 10.1016/j.cep.2005.06.005.
- [161] M. Ahmed, N. Ashgriz and H. N. Tran, « Influence of Breakup Regimes on the Droplet Size Produced by Splash-Plate Nozzles », *AIAA Journal*, vol. 47, no. 3, pp. 516–522, Mar. 2009, ISSN: 0001-1452, 1533-385X. DOI: 10.2514/1.36081.
-

- [162] R. G. Cox, « The dynamics of the spreading of liquids on a solid surface. Part 1. Viscous flow », *Journal of Fluid Mechanics*, vol. 168, no. -1, p. 169, Jul. 1986, ISSN: 0022-1120, 1469-7645. DOI: 10.1017/S0022112086000332.
- [163] O. V. Voinov, « Hydrodynamics of wetting », *Fluid Dynamics*, vol. 11, no. 5, pp. 714–721, 1977, ISSN: 0015-4628, 1573-8507. DOI: 10.1007/BF01012963.
- [164] Y. Zhao, Y. Cui, H. Numata, H. Bian, K. Wako, K. Yamanaka, K. Aoyagi and A. Chiba, « Centrifugal granulation behavior in metallic powder fabrication by Plasma Rotating Electrode Process », *Scientific Reports*, vol. 10, no. 1, Dec. 2020, ISSN: 2045-2322. DOI: 10.1038/s41598-020-75503-w.
- [165] X. Dong, J. Liu, S. Liu and Z. Li, « Quasi-static simulation of droplet morphologies using a Smoothed Particle Hydrodynamics multiphase model », *Acta Mechanica Sinica*, vol. 35, no. 1, pp. 32–44, Feb. 2019, ISSN: 0567-7718, 1614-3116. DOI: 10.1007/s10409-018-0812-x.
- [166] G. Altay, R. A. C. Croft and I. Pelupessy, « Sphray: A smoothed particle hydrodynamics ray tracer for radiative transfer », *Monthly Notices of the Royal Astronomical Society*, vol. 386, no. 4, pp. 1931–1946, Jun. 2008, ISSN: 0035-8711, 1365-2966. DOI: 10.1111/j.1365-2966.2008.13212.x.



# List of Figures

|       |  |    |
|-------|--|----|
| 1     | Schematic of the UMo fuel plate production (adapted from [1]). . . . .   | 1  |
| I.1   | Schematic of the INL powder atomizer [14]. . . . .   | 8  |
| I.2   | Growth rate as a function of dimensionless wavenumber for the Rayleigh-Plateau instability. . . . .  | 10 |
| I.3   | Mechanisms of droplet formation: a) DDF, b) LD and c) FD (adapted from [24]). The liquid flow rate is increased from left to right. . . . .  | 11 |
| I.4   | Three regimes of droplet formation for 316L. . . . .   | 12 |
| I.5   | Position of the reference case on the $(Re_T, Re_E)$ graph for 316L. . . . .   | 15 |
| I.6   | Example of partial rod atomization. . . . .  | 16 |
| I.7   | Atomization steps for the reference test case. Top view of a laser irradiated steel rod (gray level is correlated to temperature: brighter region implies higher temperature). . . . . | 16 |
| II.1  | Deformation of a continuum in a Lagrangian [left] and Eulerian [right] approach [41]. . . . .  | 22 |
| II.2  | Domain and kernel function for particle $i$ [78]. . . . .  | 26 |
| II.3  | Illustration of fluid particles ( $\bullet$ ) interacting with wall particles ( $\circ$ ) [90]. . . . .  | 33 |
| II.4  | Illustration of the color function for a surface particle [left] and a bulk particle [right]. . . . .  | 39 |
| II.5  | Illustration of the sectors around a surface particle [left] and a bulk particle [right]. . . . .  | 39 |
| II.6  | Illustration of the cover vector for a surface particle [left] and a bulk particle [right]. . . . .  | 40 |
| III.1 | Surface particles detection (red particles): comparison between the three methods described in II. . . . .   | 49 |
| III.2 | Computational time as a function of the number of particles in 2D and 3D. . . . .  | 49 |
| III.3 | Representation of the normal vectors in the transition band. . . . .   | 50 |
| III.4 | Comparison between the different surface delta functions. . . . .  | 50 |
| III.5 | Estimating the curvature $k_i$ for particles located at $r_i$ near the free surface of a 2D disk. . . . .  | 51 |
| III.6 | Comparison of different methods for estimating the curvature $k_i$ of particles located at $r_i$ near the free surface of a sphere. . . . .  | 52 |
| III.7 | Square droplet test case 2D: particles positions at $t=0$ and $t=1$ . . . . .  | 54 |
| III.8 | Pressure profile inside the droplet at $t=1$ for different resolutions (2D test case). . . . .   | 55 |
| III.9 | Square droplet test case 3D: particles positions at $t=0$ and $t=1$ . . . . .  | 55 |

|        |  |    |
|--------|--|----|
| III.10 | Pressure profile inside the droplet at $t=1$ for different resolutions (3D test case).   | 56 |
| III.11 | Particles positions at different times.  | 57 |
| III.12 | Semi major axis as a function of time for different resolutions.   | 57 |
| III.13 | Representation of the empty volume (hatched moon) for a particle at a distance $d$ from the free surface.  | 59 |
| III.14 | Representation of the intersection distance $I$ .  | 60 |
| III.15 | Particles positions at $t=2$ : a) Density evolution b) Density evolution with Shepard filter ( $n=30$ ) and c) New correction based on curvature.                  | 62 |
| III.16 | Pressure inside the droplet as a function of the distance to the center.   | 62 |
| III.17 | Particles positions at different times for two density algorithms: a) Density evolution and Shepard summation ( $n=30$ ) and b) New correction based on curvature. | 64 |
| III.18 | Correction coefficients as a function of the position of the particles along the jet axis.   | 65 |
| III.19 | Disturbance growth process in time: Comparing the growth rate as a function of time with the reference data from Dai and Schmidt.                                  | 66 |
| III.20 | Sketch of the process of particles creation.   | 67 |
| III.21 | Poiseuille flow simulation.  | 68 |
| III.22 | Simulation set-up; liquid travelling on a vibrating solid plate.   | 69 |
| III.23 | Position of the solid and liquid particles as a function of time.  | 69 |
| III.24 | Dependence of the break-up regimes on the fluid properties and the jet velocity.   | 70 |
| III.25 | Schematic representation of the atomization device.  | 71 |
| III.26 | Water jet break-up simulation.   | 73 |
| III.27 | Snapshots of the jet fragmentation for different frequencies and times ( $\Delta t = 0.2$ ms).   | 74 |
| III.28 | Theoretical, SPH and experimental data for the variation of the mean and satellite droplet diameter as a function of the applied frequency.                        | 75 |
| III.29 | Satellite and main droplet merging.  | 76 |
| III.30 | Break-up time of the first droplet as a function of the frequency.   | 76 |
| III.31 | Cumulative mass distribution as a function of the frequency.   | 77 |
| IV.1   | Reduced geometry.  | 82 |
| IV.2   | Reduced geometry with relevant boundary conditions for the REP simulation.   | 82 |
| IV.3   | Example of a particle size distribution.   | 83 |
| IV.4   | Flow rate representation.  | 85 |
| IV.5   | Example of the film thickness along the rod ( $\omega = 35000$ rpm and $Q = 3$ g/s).   | 87 |
| IV.6   | SPH simulations in the $(Re_T, Re_E)$ representation.  | 88 |
| IV.7   | Wetting configurations.  | 89 |
| IV.8   | Example of contact angle measurement for the # UMo-5 simulation.   | 90 |
| IV.9   | SPH simulation for UMo atomization: Evidence of DDF regime (a and b) and LD regime (c and d) (top view).   | 91 |
| IV.10  | Steel atomization (316L-1) showing a bimodal PSD.  | 92 |
| IV.11  | Atomization in the LD regime ( $Q=17.4$ g/s)   | 94 |

---

|       |  |     |
|-------|--|-----|
| IV.12 | Number-PSD (left) and Mass-PSD (right) for UMo. . . . .  | 95  |
| IV.13 | Cumulative mass fraction distribution for different $Re_T$ and $Re_E$ numbers. . . . .   | 96  |
| IV.14 | Linear regression analysis of SPH diameters $D_{32}$ . . . . .   | 97  |
| IV.15 | Example of partial rod atomization. . . . .  | 98  |
| IV.16 | Representation of the inflow zone for the REP simulation. . . . .  | 99  |
| IV.17 | Linear regression analysis for SPH diameters: $D_{m,10}$ , $D_{m,50}$ and $D_{m,90}$ . . . . .   | 100 |
| IV.18 | SPH results for $D_{m,90}$ as a function of $Re_T$ and $Re_E$ for $Oh = 0.00036$ . . . . .   | 100 |
| IV.19 | Schematic representation of the distance between two droplets. . . . .   | 101 |
| IV.20 | Droplet generation frequency as a function of $Re_T$ and $Re_E$ . . . . .  | 102 |
| IV.21 | Adhesion of fluid particles on the solid rod for simulation # UMo-5-d. . . . .   | 103 |
| IV.22 | Effect of applying vibrations on the a) PSD and b) Standard deviation. . . . .   | 104 |
|       |  |     |
| A.1   | Photos of the casing for metal fragmentation. . . . .  | 111 |
| A.2   | Orientation of the piezo-electric cell: a) Vertical and b) Horizontal. . . . .   | 112 |
| A.3   | Mean droplet diameter as a function of the frequency for a jet diameter of<br>150 $\mu\text{m}$ and a jet velocity of 5.5 m/s. . . . . | 114 |
| B.1   | Numerical convergence. . . . .   | 116 |

# List of Tables

|        |  |     |
|--------|--|-----|
| I.1    | Relevant dimensionless numbers to describe the atomization mechanisms. . . . .   | 9   |
| I.2    | Rayleigh-Plateau instability. . . . .  | 10  |
| I.3    | Empirical and theoretical values for the $\alpha$ in equation I.8. . . . .   | 13  |
| I.4    | Values for the $\beta$ in equation I.9. . . . .  | 13  |
| I.5    | Material properties (316L + UMo). . . . .  | 14  |
| I.6    | Experimental data for the reference case. . . . .  | 15  |
| II.1   | Examples of kernel functions. . . . .  | 27  |
| III.1  | Strong scaling for the OpenFPM framework [129]. . . . .  | 47  |
| III.2  | Comparison of curvature estimation between the method presented by Fürstena<br>u <i>et al.</i> and dividing the curvature of equation II.54 by a factor 2 for<br>different particle resolutions. . . . . | 52  |
| III.3  | Square droplet : Simulation parameters . . . . .   | 54  |
| III.4  | Square droplet : Simulation parameters . . . . .   | 56  |
| III.5  | Fraction in (%) of particles having a pressure within a certain range around<br>Laplace pressure. . . . .  | 62  |
| III.6  | Raleigh-Plateau instability: Simulation parameters . . . . .   | 63  |
| III.7  | Number of "flying" particles for each method as a function of the system<br>resolution. . . . .  | 65  |
| III.8  | Variation of the droplet mean diameter as a function of the frequency. . . . .   | 71  |
| III.9  | Simulation parameters. . . . .   | 73  |
| III.10 | Theoretical, SPH and experimental mean droplet diameter as a function of<br>the applied frequency. . . . .   | 75  |
| IV.1   | List of SPH simulations for 316L and UMo. . . . .  | 88  |
| IV.2   | Comparison between analytical and SPH dynamic contact angles. . . . .  | 90  |
| IV.3   | $D_{50}$ for experiments and SPH simulations with 316L. . . . .  | 92  |
| IV.4   | Wall-clock time for obtaining the first 10 droplets. . . . .   | 93  |
| IV.5   | Characteristic diameters for SPH simulations and semi-empirical models. . . . .  | 96  |
| IV.6   | Comparison between SPH and semi-empirical models for estimating the<br>mean Sauter diameter. . . . .   | 97  |
| IV.7   | Measured distance $d$ between two particles in SPH simulations. . . . .  | 102 |
| IV.8   | List of SPH simulations with vibrations. . . . .   | 103 |
| A.1    | Droplets mean diameter as a function of the frequency for different orienta-<br>tions of the piezo-electric cell. . . . .  | 112 |
| A.2    | Droplets mean diameter as a function of the frequency for different jet speed. . . . .   | 113 |

---

|     |   |     |
|-----|---|-----|
| A.3 | Droplets mean diameter as a function of the frequency for metal break-up. . | 114 |
| B.1 | Convergence study of the numerical model. . . . .                           | 115 |